

# Design and Implementation of a Detector for High Flux Mixed Radiation Fields

by Daniel Kramer

Department of Physics  
Faculty of Science, Humanities and Education  
Technical University of Liberec

*Supervisors:*

Dr. Bernd DEHNING (CERN)

Doc. RNDr. Miroslav ŠULC Ph.D. (TUL)

Thesis submitted for the Degree of Doctor of Philosophy in the  
Technical University of Liberec  
Czech Republic

· September 2008 ·







# Abstract

The main purpose of the LHC Beam Loss Monitoring (BLM) system is the active protection of the LHC accelerators' elements against the quench of superconducting magnets and the damage of equipment caused by the loss of circulating protons. The lost protons initiate a shower of secondary particles, which deposit their energy in the equipment and partly in a radiation detector. If thresholds in the BLM system are exceeded, the circulating LHC beam is directed towards a dump to stop the energy deposition in the fragile equipment.

The LHC BLM system will use ionization chambers as standard detectors, and in the areas with very high dose rates Secondary Emission Monitor (SEM) chambers will be employed to increase the dynamic range. The SEM is characterized by a high linearity and accuracy, low sensitivity, fast response and a good radiation tolerance. The emission of electrons from the surface layer of metals by the passage of charged particles is only measurable in a vacuum environment. This requirement leads together with the foreseen operation of 20 years to an ultra high vacuum preparation of the components and even to an additional active pumping realized by a getter pump (NEG). The signal and bias electrodes are made of Ti to make use of its Secondary Emission Yield (SEY) stability and favorable vacuum properties.

The sensitivity of the SEM was modeled in GEANT4 via the Photo-Absorption Ionization module together with a custom parameterization for the very low energy secondary electron production using the modified Sternglass formula.

The simulations were validated by comparative measurements of several prototypes with proton beams of the CERN PS Booster dump line, the SPS transfer line, the PSI Optis line and by a muon beam in the COMPASS beam line. Tests of the complete acquisition chain were performed in the LHC test collimation area of the SPS and compared to the combined Fluka and GEANT4 simulations. The linearity and long term stability was also tested in the high energy beam dump area of the SPS.

A dedicated fixed target experiment was designed in the CERN H4 secondary beam line for testing all the 400 detectors produced in IHEP Protvino. The simulations were also used for the prediction of the signal levels expected in the LHC and for an absolute

dose calibration. The comparison of simulations and measurements and of SEM and ionisation chamber measurements resulted in the relative difference range between 8 and 43% for different setups and radiation fields.

# Résumé

Le rôle principal du système de protection des pertes de faisceau (Beam Loss Monitoring system, BLM) du Grand Collisionneur de Hadrons (Large Hadrons Collider, LHC) est de fournir une protection active des éléments de l'accélérateur contre une possible transition résistive des aimants supraconducteurs, et donc contre des dégâts irréversibles des équipements. L'énergie déposée dans les différents équipements provient des gerbes secondaires. Celles-ci sont créées par les hadrons primaires échappés de leur trajectoire. L'énergie est mesurée par des détecteurs de radiation. Si les seuils du système BLM sont dépassés, le faisceau circulant dans le LHC est dirigé vers un absorbeur, stoppant ainsi toute déposition d'énergie dans les équipements fragiles.

Le système BLM du LHC utilise des chambres à ionisation comme détecteurs standards; mais dans les zones où de très hautes doses de radiation sont attendues, des détecteurs à émission secondaire (Secondary Emission Monitors, SEM) sont employés pour augmenter la gamme des énergies mesurables. Ces détecteurs ont été développés pour leur très grande linéarité et précision, leur faible sensibilité et gain, la rapidité de leur réponse, et leur tolérance aux radiations. L'émission d'électrons depuis la couche superficielle d'un métal, lors de l'impact d'une particule chargée, est mesurable seulement dans le vide. La durée prévue de fonctionnement, de 20 ans, entraîne donc des spécifications de type ultravide pour les composants des SEM, ainsi qu'un pompage actif des dernières traces de gaz par piège à gaz (getter), constitué de NEG.

Les électrodes du SEM sont faites en titane, du fait de sa stabilité vis-à-vis de l'émission secondaire, et son comportement dans le vide. La sensibilité du SEM a été modélisée dans GEANT4 en utilisant le module Photo-Absorption Ionisation, ainsi qu'un paramétrage spécifique de l'émission des électrons à très basse énergie, par une formule de Sternglass modifiée. Les simulations ont été validées par une mesure comparative de plusieurs prototypes soumis à différents faisceaux de protons, au niveau de la ligne d'absorption de faisceau du PS Booster, de la ligne de transfert du SPS, de la ligne Optis du PSI, et auprès d'un faisceau de muons à COMPASS.

L'ensemble de la chaîne d'acquisition a été testé dans la zone de collimation du SPS et comparé aux simulations en FLUKA et GEANT4 combinées. La linéarité, ainsi que

la stabilité à long terme, ont aussi été testées auprès des absorbeurs de faisceau à haute énergie du SPS. Une expérience à cible fixe a été spécifiquement conçue au niveau de la ligne de faisceau secondaire H4 au CERN, afin de tester les 400 détecteurs produits au IHEP Protvino.

La précision des mesure de dose de radiation par les SEM a été évaluée par comparaison des résultats des simulations avec ces mesures, mais aussi celles des chambres à ionisation. La différence relative se situe entre 10 et 40%, pour les différents réglages et types de radiation.

# Acknowledgment

I would like to express my sincere gratitude to everybody, who contributed to the conception, growth and birth of this thesis.

During my stay at CERN, my supervisor Bernd Dehning was always very carefully listening to my ideas and forced me to support every decision by strong arguments, which helped me considerably to stay focused. I appreciated mostly the long night discussions on different physics subjects and his insight. I would also like to thank to my university supervisor Miroslav Šulc for guiding me through the dungeon of doctoral studies and mostly for bringing me to CERN and fully supporting me.

I have spent a very pleasant time in the Beam Loss section and could profit from the deep knowledge and experience of its members in domains I was not familiar with. In particular, I am grateful to Gianfranco Ferioli - the guru of the secondary emission screens in many accelerators. We have spent endless measurement nights in various control rooms and barns with the electronics wizards Ewald Effinger, Christos Zamantzas and Jonathan Emery. I enjoyed discovering bugs in their otherwise perfect work.

My colleagues, I shared office with, during the three year period Markus Stockner, Laurette Ponce, Mariusz Sapinski, Darius Bocian, Till Böhlen and Aurelien Marsili had to listen to my mostly stupid jokes but despite of that, the grid of our brains helped solving many problems and creating a lot of fun.

I am glad I could work also with Raymond Tissier, Ion Savu, Claudine Chery and Christophe Vuitton, who were always very helpful in constructing different prototypes in very short time and with Barbara Holzer and Viatcheslav Grishin, who organized the production of the detectors.

My thanks belong to the vacuum experts Paolo Chiggiato, Ivo Wevers and Mauro Taborelli for their great help with the very challenging design and tests of the detector from the vacuum point of view and to Thijs Wijnands for organizing our numerous calibration trips to PSI.

My eternal gratitude and love belongs to my amazing wife Tereza for everything she is and to our daughter Sarah, who was conceived, grown and born in parallel to this work.

The final thanks belongs to you for reading these lines, which means that universe still exists.

# Contents

<b>Abstract</b>	<b>iii</b>
<b>Résumé</b>	<b>v</b>
<b>Acknowledgment</b>	<b>vii</b>
<b>Contents</b>	<b>xi</b>
<b>Introduction</b>	<b>xiii</b>
<b>1 The Large Hadron Collider</b>	<b>1</b>
1.1 CERN . . . . .	1
1.2 The LHC Injector Chain . . . . .	1
1.2.1 Upgrades for the high intensity LHC beams . . . . .	3
1.3 The LHC accelerator . . . . .	4
1.3.1 Basic Layout of the LHC . . . . .	5
1.3.2 Machine Protection . . . . .	6
1.3.3 Quench Levels . . . . .	8
1.3.4 Collimation . . . . .	9
1.3.5 Beam Dump . . . . .	10
<b>2 Beam Loss Monitoring System</b>	<b>13</b>
2.1 Possible Sources of Beam Losses . . . . .	13
2.2 Expected Loss Locations . . . . .	14
2.3 Data Acquisition System . . . . .	16
2.3.1 Analog Front-End . . . . .	17
2.3.2 Data Acquisition Board . . . . .	18
2.3.3 Successive Running Sums . . . . .	19
2.4 Detection Requirements . . . . .	19
2.4.1 Ionisation Chamber . . . . .	20
2.4.2 Low Response Detector . . . . .	21

<b>3</b>	<b>Secondary Electron Emission</b>	<b>23</b>
3.1	Energy loss by ionisation . . . . .	23
3.2	Secondary Electron theory . . . . .	25
3.2.1	Generation of Secondary Electrons in Solids . . . . .	26
3.2.2	Diffusion process . . . . .	27
3.2.3	Emission process . . . . .	28
3.3	Semi-empirical theory of Sternglass . . . . .	28
3.4	Angular dependence . . . . .	30
3.5	Existing applications of the Secondary Electron Emission . . . . .	31
<b>4</b>	<b>Geant4 Simulations</b>	<b>33</b>
4.1	Introduction to GEANT4 code . . . . .	33
4.1.1	Hadronic models . . . . .	34
4.1.2	Electromagnetic models . . . . .	35
4.1.3	Photo-Absorption and Ionisation module . . . . .	36
4.1.4	Physics List . . . . .	36
4.2	Secondary Emission Model in Geant4 . . . . .	39
4.2.1	Choice of the Model . . . . .	39
4.2.2	Parametrized generation of Secondary Electrons . . . . .	40
4.2.3	Charge balance and signal generation . . . . .	41
4.2.4	Model Calibration . . . . .	43
4.2.5	Detector geometry . . . . .	45
4.2.6	Electrode thickness dependence . . . . .	46
4.2.7	Range cut-off dependence . . . . .	48
4.2.8	Response for different particle types . . . . .	49
4.3	Estimation of the SEM signal in the LHC dump region . . . . .	51
4.4	Simulation of the fixed target experiment for production testing and absolute calibration . . . . .	55
4.4.1	Absolute calibration of the SEM . . . . .	56
<b>5</b>	<b>Design and Production of the SEM</b>	<b>61</b>
5.1	Choice of materials . . . . .	62
5.1.1	Signal electrode . . . . .	62
5.1.2	Electrode holders . . . . .	64
5.1.3	Stainless steel components . . . . .	66
5.2	Vacuum . . . . .	67
5.2.1	Getter Pump . . . . .	67
5.2.2	Thermal and radiation induced outgassing . . . . .	68

5.2.3	Test production at CERN . . . . .	70
5.3	Serial production at IHEP Protvino . . . . .	70
5.3.1	Vacuum stand . . . . .	71
5.3.2	Quality control . . . . .	72
<b>6</b>	<b>Test and Calibration Measurements</b>	<b>75</b>
6.1	Early stage prototype tests . . . . .	76
6.1.1	Experimental setup in PSB . . . . .	76
6.1.2	Experimental setup in PSI . . . . .	77
6.1.3	Results and discussion . . . . .	78
6.2	Calibration in Cyclotron proton beam at 63 MeV . . . . .	80
6.2.1	Experimental Setup . . . . .	80
6.2.2	Results and comparison with simulations . . . . .	82
6.3	Calibration by bunched proton beam at 1.4 GeV . . . . .	83
6.3.1	Experimental setup . . . . .	84
6.3.2	Results and comparison with simulations . . . . .	86
6.4	High energy proton beam scan across the SEM . . . . .	87
6.4.1	Experimental setup . . . . .	87
6.4.2	Comparison of measurements with simulations . . . . .	89
6.5	Test in muon beam at 160 GeV . . . . .	89
6.6	BLM system tests in the SPS collimation area . . . . .	90
6.6.1	Experimental setup . . . . .	90
6.6.2	Results and comparison with simulations . . . . .	92
6.7	Linearity measurements in the SPS beam dump area . . . . .	94
6.7.1	Measurement setup . . . . .	95
6.7.2	Measurement results . . . . .	96
6.8	Production validation in a mixed radiation field . . . . .	101
6.8.1	Experiment requirements and setup . . . . .	101
6.8.2	Results . . . . .	103
<b>7</b>	<b>Conclusions</b>	<b>109</b>
<b>A</b>	<b>Drawings</b>	<b>119</b>
<b>B</b>	<b>Signal paths for the LHC BLM detectors</b>	<b>123</b>
<b>C</b>	<b>Space Charge Effect Correction</b>	<b>125</b>
<b>D</b>	<b>List of publications</b>	<b>127</b>



# Introduction

The Large Hadron Collider (LHC), which was constructed at CERN, the European Organization for Nuclear Research near Geneva, Switzerland, is the worlds most advanced particle physics instrument. It is going to accelerate particles up to the energy of 7 TeV and bring them into collision in four different experiments. In order to keep the particles circulating inside the 27 km long accelerator, superconducting cryogenic magnets are used.

The total amount of energy stored in the magnet coils reaches 10 GJ in the nominal conditions, while the energy carried by each of the two counter rotating beams amounts to 362 MJ. If even a very small fraction ( $10^{-9}$ ) of the beam energy is absorbed in the magnets, the coils undergo a resistive transition from the superconducting state or even get damaged causing a considerable downtime from several hours to several months. A very sophisticated active protection system is therefore critical for the safe operation of the machine.

This work has been carried out within the section responsible for the monitoring of beam losses, which is done by measuring the radiation produced by particles from the secondary showers developing in the equipment and initiated by the lost protons. Due to the unprecedented beam energy and intensity, the radiation levels in several areas of the LHC will reach very high levels. In order to correctly measure such high dose rates, a completely new type of radiation detector had to be designed.

The main objectives of this work are summarized as follows: Design of a radiation detector with a very low gain, high linearity and radiation tolerance susceptible to accurately operate in very high dose rate environments.

These specifications are addressed by the work plan:

- build a simulation model able to predict the response of the detector
- validate the simulation model by verification measurements
- calibrate the detector

The required precision of the energy deposition measurements by the BLM system is 200%. The contribution of the detector to the total uncertainty is limited to 40% including the unknowns of the simulation based calibration.

The first chapter of this work introduces CERN with its Large Hadron Collider and focuses to the subsystems relevant for this subject.

The second chapter is dedicated to the philosophy and components of the LHC Beam Loss Monitoring system.

Chapter 3 describes the present knowledge of the Secondary Electron Emission from metals, which is the main process generating the signal in the detector developed during this work. It introduces the theoretical treatment of Sternglass.

The contribution of the author starts with the simulation model built in the Geant4 particle physics Monte-Carlo simulation framework (Chapter 4). The implementation of the secondary electron emission model based on the modified and calibrated Sternglass formula is described after the introduction of the relevant components of Geant4. The two step signal generation is described in detail and the sensitivity of the simulations to different parameters is presented. The response spectra generated by the simulations were used for predicting the detector signal in the LHC dump area. The absolute calibration of the detector is provided by combining measurements and simulations of a fixed target experiment.

Chapter 5 describes the design of the detector and its main components. The calculations of the long term outgassing, which revealed the necessity of an active pumping element are followed by the description of the vacuum and bake-out cycle.

Chapter 6 starts by the description of the initial prototype tests performed in the development phase. The test measurements of the final prototypes in different radiation conditions are compared to the corresponding simulations. The validation of the series production by a fixed target experiment is described at the end of the chapter.

The results of this work are summarized in the Conclusions.

# Chapter 1

## The Large Hadron Collider

### 1.1 CERN

CERN, the European Organization for Nuclear Research, is one of the worlds largest and most respected centers for scientific research. Its main research activity is fundamental physics and the structure of matter at the smallest scale. At CERN, the worlds largest and most complex scientific instruments are used to study the basic constituents of matter the fundamental particles. By studying what happens when these particles collide, physicists learn about the laws driving the interactions of the particles.

The instruments used at CERN are particle accelerators and detectors. Accelerators boost beams of particles to high energies before they are made to collide with each other or with stationary targets. Detectors observe and record the results of these collisions.

Founded in 1954, the CERN Laboratory sits astride the FrancoSwiss border near Geneva. It was one of Europes first joint ventures and now has 20 Member States[1].

Currently, the key objective of CERN is to complete the construction and fully exploit the potential of the world's largest research instrument, the Large Hadron Collider (LHC). The parameters of the LHC were chosen to allow a high discovery potential of for example the Higgs particle. It surpasses other existing accelerators (HERA, Tevatron, SPS) by almost a factor 10 in energy and more than a factor 10 in intensity.

### 1.2 The LHC Injector Chain

CERN's accelerator complex consists of many different types of linear and circular accelerators and interconnecting transfer lines.

At the beginning of the chain, the protons are extracted from hydrogen and ac-

celerated in the LINAC2 to the kinetic energy of 50 MeV per proton and transferred to the Proton Synchrotron BOOSTER (PSB). The PSB accelerates them to 1.4 GeV and sends to the Proton Synchrotron (PS). After having reached 25 GeV in the PS, the protons are injected to the Super Proton Synchrotron (SPS) and accelerated to 450 GeV. Finally, they are transferred to the two LHC rings and accelerated for 20 minutes to the nominal energy of 7 TeV.

The LHC is also supposed to accelerate and collide lead ions ( $Pb^{82+}$ ) with the kinetic energy of 2.8 TeV per nucleon. These ions will be produced in the LINAC3 and accumulated in the Low energy ion ring (Leir). Afterwards, they will be injected into the PS and follow the same path as the protons up to the LHC.

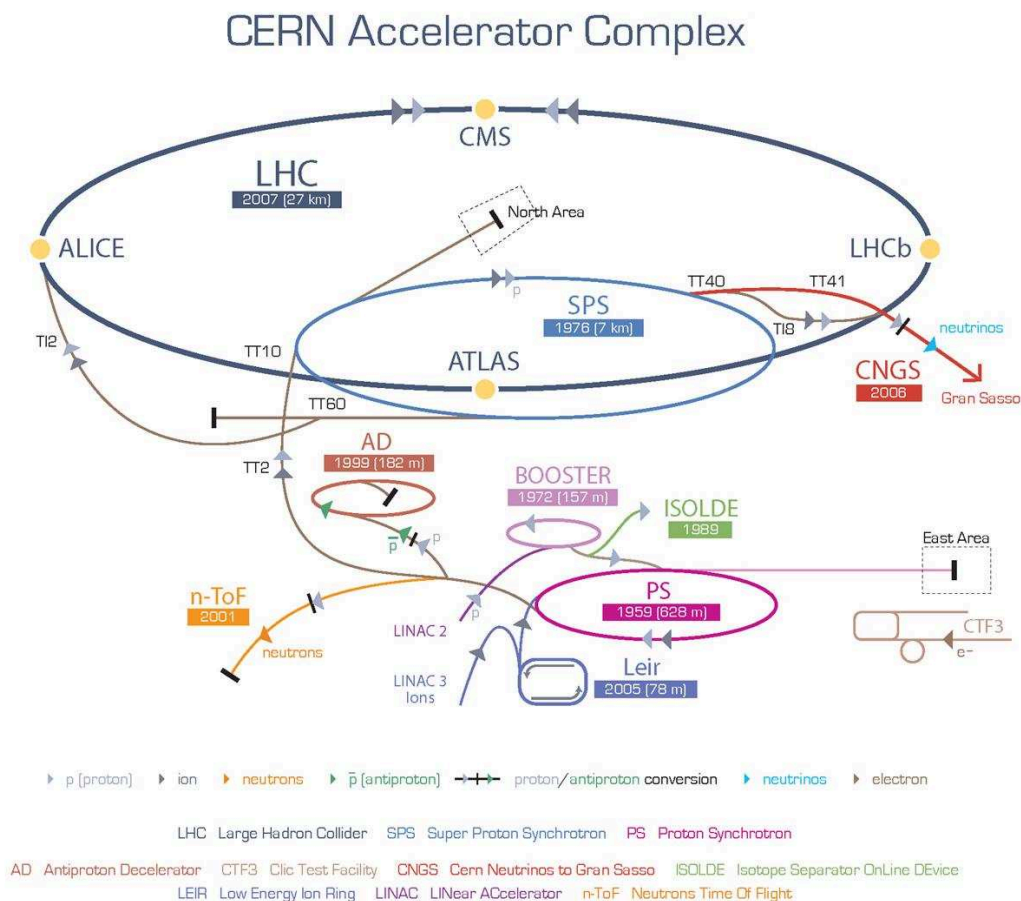


Figure 1.1: CERN accelerator complex.

Several injections from the smaller accelerator are generally needed to fill the subsequent machine so the filling of one LHC ring to the nominal intensity should take

in total 4 minutes and 20 seconds. Once the nominal energy is reached, the particles should remain circulating in the LHC and colliding inside the four main experiments (ATLAS, CMS, LHCb and ALICE) for several hours. There are two other smaller experiments in the LHC. The LHCf is installed close to the ATLAS interaction point and the TOTEM nearby CMS.

The complex of the CERN accelerators is very versatile and far from being just the injectors to the LHC. Most of the machines have their own dedicated experimental areas using fixed targets to explore wide range of physics phenomena. The beam types range from high intensity neutrons for the n-ToF experiment, decelerated anti-protons for anti-matter production to neutrino beams sent to Italy by the CNGS project.

Figure 1.1 presents a general overview of the system of consecutive accelerators including the LHC with its four main experiments (yellow points).

### 1.2.1 Upgrades for the high intensity LHC beams

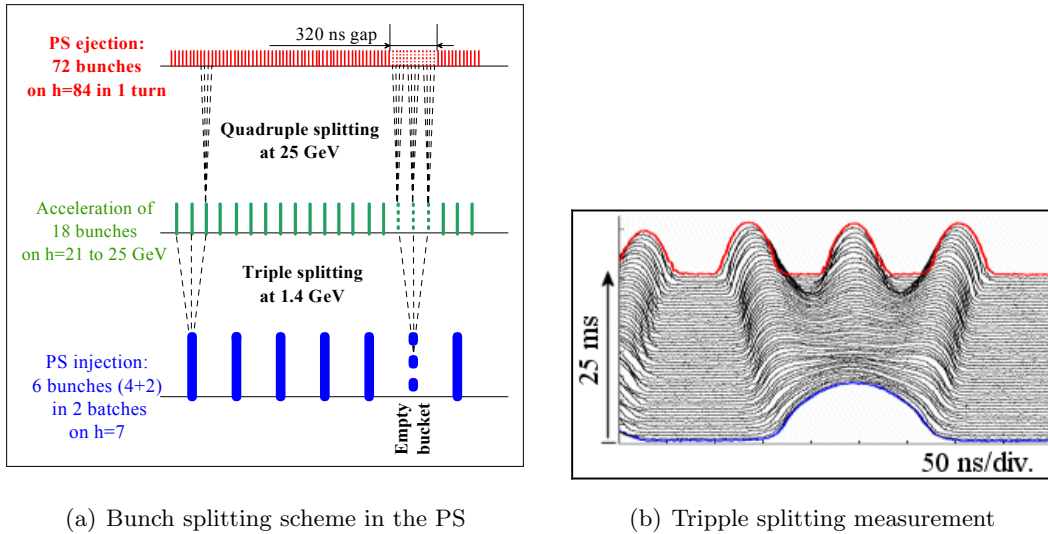
The LHC will require for its nominal operation, beams of a very high intensity. This means that high density bunches should be extracted from the SPS with a spacing of 25 ns (see Table 1.1). For this reason, the injectors had to be upgraded and dedicated beam manipulations introduced.

The Linac2 has to bring 180 mA of proton current to the PSB while the design value was 150 mA. A considerable effort was undertaken to tune all the parameters and several components were changed, like i.e. the power amplifiers of the RF system [23].

The PSB operation is very difficult with the bunch density needed for the LHC due to the very high space charge and the resulting electromagnetic fields. Each ring of the PSB will therefore accelerate two bunches with half the nominal intensity in parallel and the extraction energy was increased from 1 to 1.4 GeV. The main magnet power supplies had to be changed as well as the RF system including the cavities.

The final bunch structure has to be produced already in the PS ring. Hence, a new bunch splitting scheme was implemented requiring important modifications in the RF system. The bunches are split upon arrival into three smaller ones by using higher harmonics of the main RF frequency. The further splitting into four bunches is applied after acceleration as can be seen on Figure 1.2. The length of the bunch is still too high after the last manipulation, so a bunch rotation has to be performed further reducing the length to the required 4 ns.

The changes in the SPS were considerable as well and included for example the



(a) Bunch splitting scheme in the PS

(b) Tripple splitting measurement

Figure 1.2: Generation of the nominal bunch train for LHC (25 ns bunch spacing). From [23]

closure of the West experimental area leaving the space for an upgraded fast extraction for the clockwise (see Fig. 1.1) beam of the LHC. The anticlockwise beam will use a completely new extraction system. The combined length of 5.6 km of the transfer lines TI2 and TI8 had to be built and equipped. An entirely new 800 MHz RF system was installed in the SPS ring. The major issue for the LHC beams in the SPS is the Electron Cloud [24] effect inducing heavy instabilities to the large intensity beams with the short 25 ns bunch spacing. The main cure was found to be the dedicated Scrubbing run (take few days), during which the beam pipe is bombarded by electrons. Consequently, secondary electron emission coefficient of the surface is lowered, further inhibiting the cloud buildup.

### 1.3 The LHC accelerator

The very purpose of the LHC is to produce particles by colliding hadrons stored in the two counter rotating beams. The detectors around the interaction points, where the beams are crossing, will explore the physics in the TeV range of the proton constituents.

The event rate in a collider is proportional to the interaction cross section  $\sigma_{int}$  and the factor of proportionality is called the luminosity:

$$R = \mathcal{L}\sigma_{int} \quad (1.1)$$

Quantity	number
Circumference	26 659 m
Dipole operating temperature	1.9 K
Number of magnets	9593
Number of main dipoles	1232
Number of main quadrupoles	392
Number of RF cavities	8 per beam
Nominal energy, protons	7 TeV
Nominal energy, ions	2.76 TeV/u
Peak magnetic dipole field	8.33 T
Min. bunch spacing	25 ns
Design luminosity	$10^{34} \text{ cm}^{-2}$
No. of bunches per proton beam	2808
No. of protons per bunch	$1.15 \times 10^{11}$
Revolution frequency	11.245 kHz
Revolution period	88.924 $\mu\text{s}$
Collision rate	600 MHz
Average beam size	200 $\mu\text{m}$

Table 1.1: Some of the nominal parameters of the LHC

If two bunches containing  $n_1$  and  $n_2$  particles collide with frequency  $f$ , the luminosity is

$$\mathcal{L} = f \frac{n_1 \cdot n_2}{4\pi \cdot \sigma_x \cdot \sigma_y} \quad (1.2)$$

where  $\sigma_x$  and  $\sigma_y$  characterize the Gaussian transverse beam profiles in the horizontal (bend) and vertical directions and to simplify the expression it is assumed that the bunches are identical in the transverse profile, that the profiles are independent of position along the bunch, and the particle distributions are not altered during collision [2].

### 1.3.1 Basic Layout of the LHC

The LHC machine is divided into eight equivalent bending sections called ARCs. They are separated by eight straight sections, out of which four are housing the main experiments in their centers called Insertion Regions (IR). The beams from the SPS are injected close to the LHCb and ALICE experiments. The superconducting Radio Frequency (RF) cavities necessary for providing energy to the particles during acceleration are located in the IR4. The “beam cleaning” collimation systems are divided between IR3 and IR7. When needed, the beams will be extracted from the LHC by the beam

dumping system in IR6.

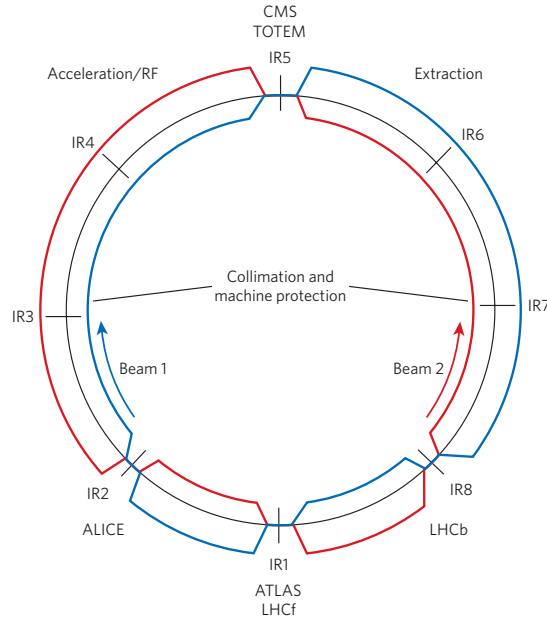


Figure 1.3: LHC beam direction and beam naming conventions. From [22]

The LHC accelerator is using superconducting NbTi dipole magnets to bend and quadrupole magnets to focus the particle beams. The coils have to be constantly cooled by the superfluid helium at 1.9 K to maintain the superconductivity, but there are also some magnets operating at 4.5 K and normal conducting magnets at room temperature. When the particle trajectories in the beam pipe are bent by the magnetic fields, they emit synchrotron radiation, which is depositing energy into the elements of the beam pipe. This energy has to be extracted by the cryogenic systems, otherwise the coils would undergo the transition from the superconducting to the resistive state called quench.

Several key parameters of the LHC are summarized in the table 1.1.

### 1.3.2 Machine Protection

The energy stored in the nominal LHC beam is  $3.23 \times 10^{14} \cdot 7 \text{ TeV} = 362 \text{ MJ}$ , which is at least 200 times more than any other accelerator and is equivalent to 87 kg of TNT. The existing machines (SPS, HERA, TEVATRON) with very large stored beam energy had already several accidents [20] causing considerable damage to various elements of the beam lines. If an LHC dipole magnet was damaged, it would take approximately 30 days to exchange it, causing a considerable down time. Nevertheless, if a final focusing triplet magnet was damaged, it could not be replaced as there are no spares. It is therefore essential for the LHC to minimize the risk of critical failures. One can clearly

see on Figure 1.4 that already the beams injected from the SPS have a considerable damage potential.

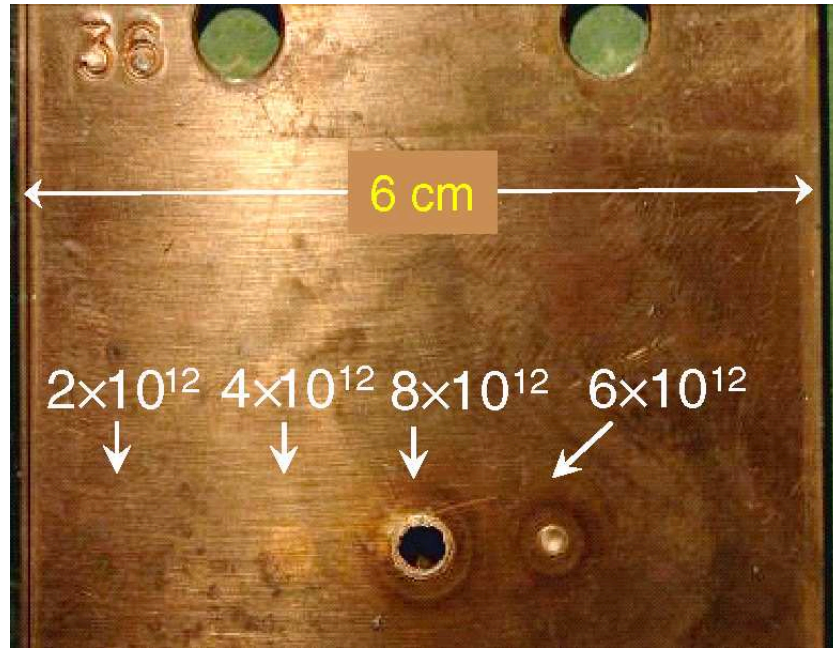


Figure 1.4: Damage of a copper plate by a 450 GeV beam at different intensities. The plate was located at the maximum shower density. From [20]

The machine protection has to be assured by active as well as passive systems. The passive ones consist mainly of the collimation system and various absorbers protecting the most sensitive equipment from failure scenarios that can not be handled by the active systems. The philosophy of the active protection system is based on the detection of dangerous situations (i.e. too high beam losses), prompt removal of the “Beam Permit” signal from the Beam Interlock System (BIS) and a subsequent fast extraction of the beams to the beam dumps. There are about 140 systems connected to the BIS and each of them can request the beam abort, but only one measures the beam losses.

The second priority of the machine protection systems is to increase the availability of the LHC. Excessive beam losses can heat up the coils and quench the superconducting magnets. The recovery time from such event can take from 1 up to 48 hours and therefore should be avoided as much as possible.

The main active detection systems participating to the machine protection of the LHC are the Quench Protection System (QPS), the fast magnet current change monitors and the Beam Loss Monitoring (BLM) system. The QPS is measuring the voltage across the superconducting magnets and when a threshold voltage appears signaling

a starting resistive transition, the coils are heated to assure a homogeneous quench. In parallel, the electric current is safely extracted from the magnet. The fast magnet current change monitors are detecting fast changes of the electric current in the warm magnets, which could lead to fast changes of the beam position and eventually fast beam losses (i.e the injection septum). The BLM system is supposed to detect fast to slow losses of particles impacting on the beam pipe and request a beam abort if a given threshold value is exceeded. The Chapter 2 is dedicated to the BLM system.

### 1.3.3 Quench Levels

The superconducting cables in the magnet coils are cooled by the superfluid He to 1.9 K or liquid He to 4.5 K which allows the use of the nominal current of  $\sim 12000$  A without any resistive losses. The temperature of the cables can slightly increase under external heat load without quenching the coil. The allowed temperature increase is called the temperature margin and depends on the electric current density, the temperature and magnetic field. The energy needed to heat up the coil by the temperature margin in a given time is called the “quench limit” and corresponds to a maximum allowed energy deposition inside the coil.

The particles lost from the primary beam will create showers and deposit energy in the magnet coils. If the shower is propagated through the cryostat using the Geant4 code, the signal created in the beam loss monitor corresponding to the quench limit in the coil can be estimated.

The accurate knowledge of the quench levels is critical for the proper operation of the BLM system, because the beam abort thresholds for the ionisation chambers on the cryogenic magnets will be set to 30% of the quench limit. The quench level for the fast losses is expressed as energy density [ $\text{mJ}/\text{cm}^3$ ] as it depends on the deposited energy density which is compared to the heat capacity of the coil. The steady state quench limit is defined by the efficiency of the cooling system and is expressed as power density [ $\text{mW}/\text{cm}^3$ ]. The intermediate duration quench limits are calculated by assuming also the heat transfer from the cables to the Helium or just the heat capacity of the Helium. The quench limits for the LHC dipole magnets are presented on the Fig. 1.5 as function of the loss duration and for the injection and top energy. The quench limit expressed as the proton loss rate impacting on the inner wall of the vacuum chamber, which is proportional to the power deposit in the magnet coil. The quench limit is lower at high energy because of the higher energy density of the secondary shower, the transverse shrinking of the shower and the lower temperature margin caused by the higher current density and higher field.

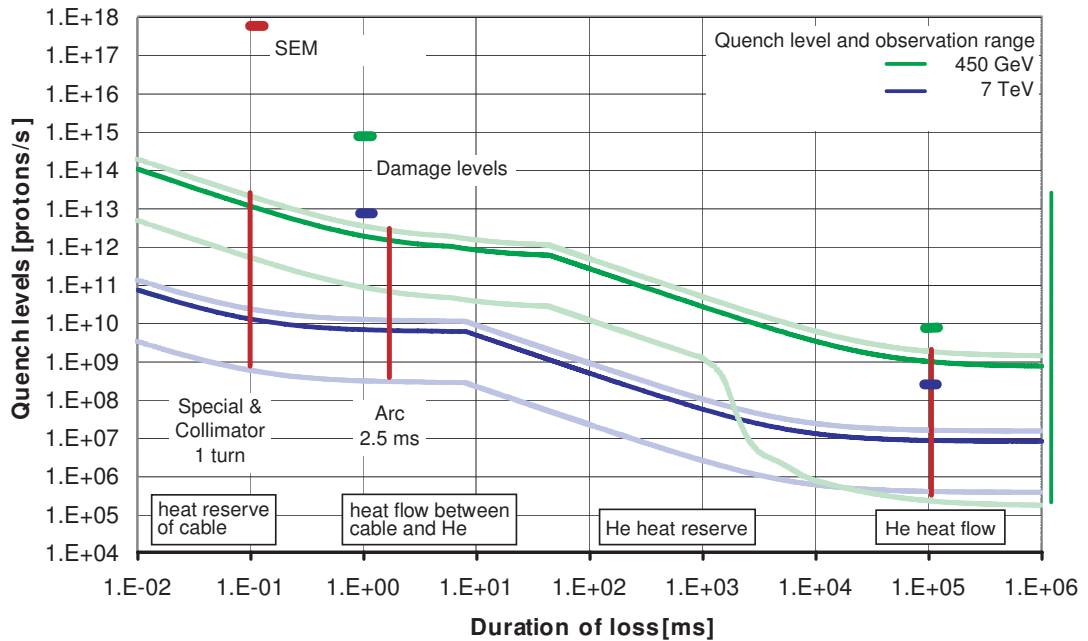


Figure 1.5: Quench levels of the LHC bending magnets as function of loss duration at 450 GeV and at 7 TeV (dark green and dark blue). The required observation range for both energies is indicated in light green and light blue color.

### 1.3.4 Collimation

In a circular accelerator, particles perform transverse oscillations around the central orbit called the Betatron oscillations. The amplitude as well as the frequency of the oscillations depend on the configuration of the focusing elements. Similar behavior appears in the longitudinal dimension. When a particle arrives to an accelerating RF cavity, it is accelerated or decelerated depending on its phase which in turn depends on the momentum of the particle. This effect produces longitudinal oscillations called Synchrotron oscillations.

As the geometrical aperture of the beam pipe is not infinite, there is a limit for the amplitude of the betatron oscillations beyond which the particles would hit the walls of the accelerator. Also in the longitudinal space, there is an energy acceptance limit beyond which the particles do not remain stable and can be lost mainly during the beginning of the acceleration process.

The collimation scheme is based on the multi-stage scattering and absorbing scheme (see Fig. 1.6). The primary collimator mainly scatters the particles from the primary beam halo, which are then further interacting inside the secondary collimator and are finally absorbed by the tertiary collimators or absorbers. The collimation system limits the maximum oscillation amplitudes or energy offsets by extracting the off-orbit or

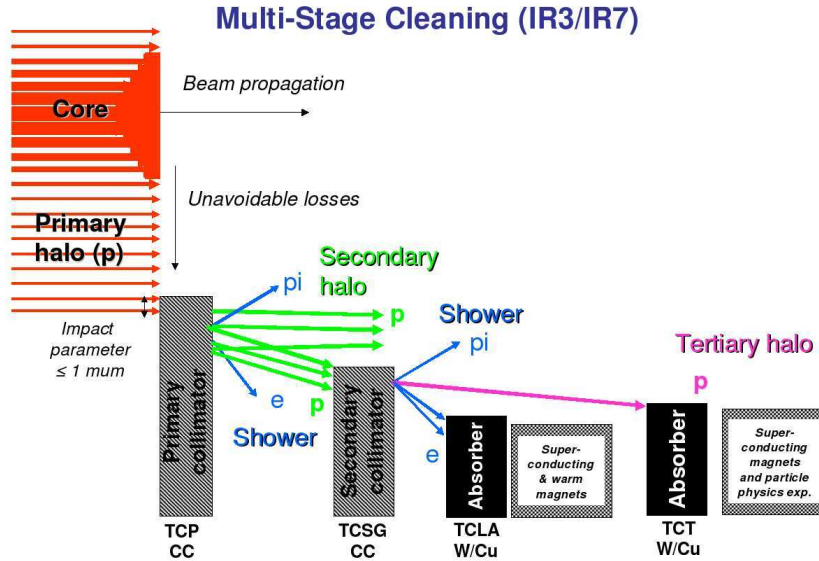


Figure 1.6: Schematic of the multi-stage collimation system in the LHC. Courtesy of R. Assmann.

off-momentum particles from the beam.

The main component of the primary and secondary collimators are the carbon fiber reinforced graphite jaws, which will be in charge of scattering the beam particles during operation. The copper support structure of the jaws is cooled down by circulating water. The efficiency of the cooling system imposes the steady state limit on the particle load of the collimator, because the graphite material starts outgassing even at moderately elevated temperatures thus degrading the vacuum in the beam pipe. The short beam loss limit is given by the peak energy density allowed in the material of the jaw, beyond which the graphite would suffer structural damage.

### 1.3.5 Beam Dump

The role of the LHC beam dumping system is to safely dispose of the beam when beam operation must be interrupted for any reason.

”Fifteen fast kicker magnets with a pulse rise-time of less than  $3 \mu\text{s}$  deflect the beam by an angle of  $280 \mu\text{rad}$  in the horizontal plane. To ensure that all particles are extracted from the LHC, the beam has a particle free abort gap with a length of  $3 \mu\text{s}$  corresponding to the kicker rise-time. The extraction kicker is triggered such that the field increases from zero to the nominal value during this gap when there should be no particles. Downstream of the kicker the beam is deflected vertically by  $2.4 \text{ mrad}$  towards the beam dump block by 15 septum magnets. A short distance further downstream, ten

diluter kicker magnets are used to “paint” the bunches in both horizontal and vertical directions to reduce the beam density on the dump block (see Fig. 1.7).

The beam is transferred through a 700 m long extraction line to increase the transverse r.m.s. beam size from approximately 0.2 to 1.5 mm and to spread the bunches further on the dump block. The overall shape is produced by the deflection of the extraction and dilution kickers. For nominal beam parameters, the maximum temperature in the beam dump block is expected to be in the order of about 700 °C.” [20]

All the warm magnets in the dump extraction line are monitored by BLM system to allow post-mortem analysis in case of the system failure. Due to the risk of very fast and intense losses, the magnets are equipped by the ionisation chambers together with the SEM monitors as it can be seen on Fig. 2.1.

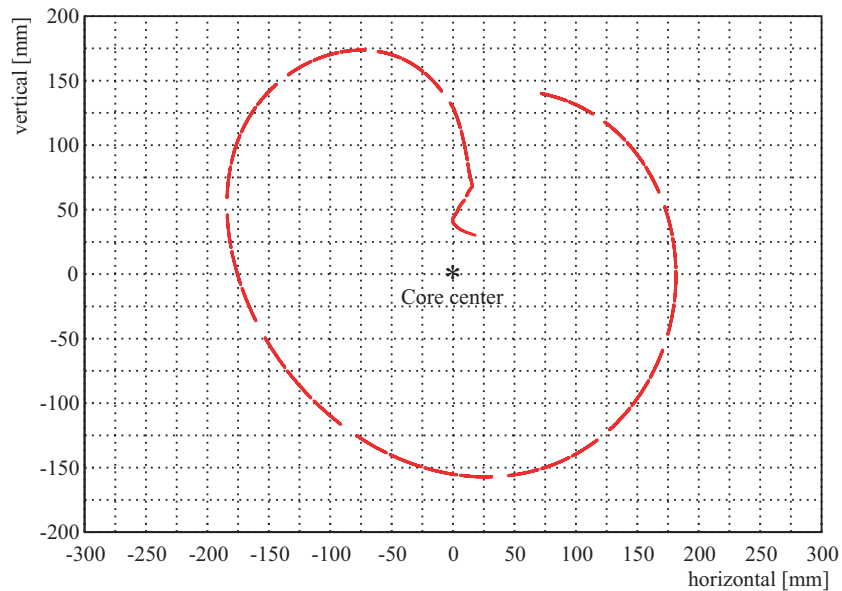


Figure 1.7: Positions where the 2808 bunches from the beam impinge on the dump core front face in normal operation of the LHC. The origin corresponds to the center of the core front face. From [19]



## Chapter 2

# Beam Loss Monitoring System

The Beam Loss Monitoring (BLM) system is used for measuring and localizing radiation created by the lost particles impacting on the accelerator beam pipe. It is the only system which can protect the LHC from fast losses and which can prevent a quench.

When a high energy hadron intercepts an aperture restriction like a warm quadrupole magnet, it initiates a hadronic shower, which extends far beyond the impact point. The Beam Loss Monitors have to detect this radiation within a reasonable response time. The front-end electronics will then send the data in a reliable way to the processing electronics, which has to compare the measured dose rate to the safety operation threshold valid for the actual beam energy. The BLM detectors are placed in the locations where the losses would most likely occur, because the beam size reaches its local maximum with respect to the available aperture.

### 2.1 Possible Sources of Beam Losses

The beam loss events are classified according to their duration mainly given by the different reaction times of the protection systems.

- Ultra Fast loss ...  $< 356 \mu\text{s}$  (4 turns)
- Fast loss ... 0.267 to 10 ms
- Intermediate loss ... 10 ms to 1 s
- Slow loss ...  $> 1$  s
- Steady state loss ...  $> 100$  s

The ultra fast losses can occur mainly due to a misfire of one of the very fast kicker magnets or a wrong injection from the SPS. Due to the reaction time of the protection chain (BLM system, Beam Interlock System and the Beam Dumping system) in the

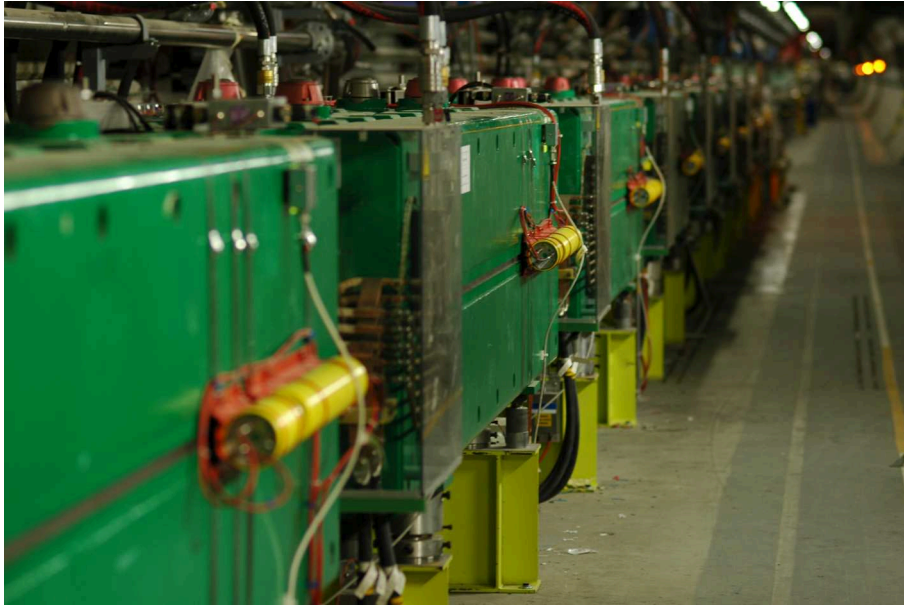


Figure 2.1: Ionisation chambers and SEM BLM detectors on the warm magnets of the LHC extraction dump line.

order of 3 LHC revolutions, the machine protection has to rely on the passive absorbers for this type of events as illustrated by the Fig. 2.2.

The fast beam losses will be covered only by the BLM system acting as a damage and quench prevention. It uses integration windows from  $40 \mu\text{s}$  to 80 s. The origin of the losses can be significantly diverse, but a considerable effort is being done in order to predict the possible loss scenarios. Several examples of different failure modes, which can lead to significant losses are presented in the following list.

- failure of a magnet power converter
- kicker magnet failure or misfire
- asynchronous beam dump
- miss steering of the beam
- beam resonance crossing and resulting blow up

## 2.2 Expected Loss Locations

The LHC BLM system will use roughly 4000 detectors to cover the 27 km of the machine circumference and the two dump lines. The length of a hadronic shower created by a 7 TeV proton in a cryostat can extend only to few meters as seen on the Figure 2.3 and the detectors will cover only 0.5 m.

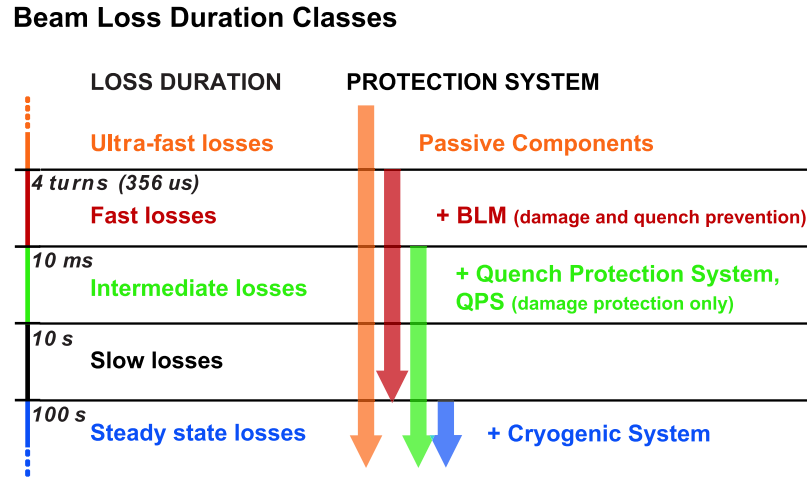


Figure 2.2: Classification of beam losses according to their duration and the applicable protection systems (courtesy of E.B. Holzer).

From the machine protection point of view, the monitors have to be placed at the locations with the highest secondary shower particle density created by proton impacts in the most fragile areas. For the optimization of the detector locations, the proton loss simulations were combined with particle shower simulations taking into account the damage and quench potentials. It is for example not relevant to protect a simple beam pipe in a straight section whereas the superconducting quadrupoles are considered as the most critical elements. The physical beam size in the periodic lattice is generally highest inside the quadrupole so the losses will likely concentrate in the beginning of the quadrupole and induce quenches or even damage the fragile magnets.

According to the previous studies [43], it was decided to place three monitors on every cryogenic quadrupole for each beam at the level of the beam pipes to cover most of the expected losses (see Fig. 2.3). As the showers can be initiated close to the end of the magnet at the transition between two magnets, one of the monitors will be physically located on the following dipole. This is the baseline solution for the periodically structured arcs and straight section magnets.

The straight sections of the insertions have a much more complicated structure and can not be easily generalized. Every collimator (primary or secondary) will be monitored by the BLM system as well as the cryogenic feedthroughs (DFB). The injection regions composed of the injection septum (MSI), protection collimators (TDI), masks and the D1 dipole will be covered too. Most of the elements of the dump line in IR6 have their individual monitors serving mainly for the analysis in case of a failure. Every

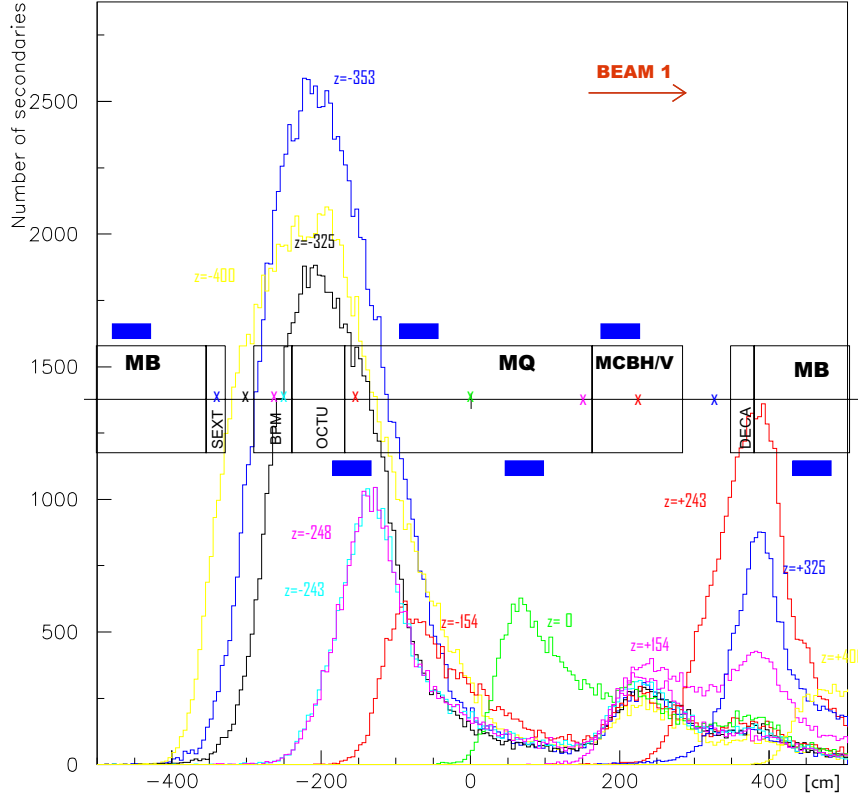


Figure 2.3: Losses in the MQY magnet with different impact locations along the magnet. Particles scored outside of the cryostat using Geant3.

dispersion suppressor, which is a special part of the lattice at the beginning of each straight section, has been well covered, because the particles with large momentum offsets produced in the IRs will be predominantly lost in that location.

### 2.3 Data Acquisition System

The detector output signals are measured by the analogue part of the front-end electronics card located in the LHC tunnel, and transmitted to the surface, where the final evaluation takes place in the Threshold Comparator (BLMTC) data acquisition board. A schema of the complete measurement chain presented on the Fig. 2.4.

The signal current from the BLM chambers is converted to a digital form in the radiation tolerant front-end card for eight channels in parallel. The data are then sent via long optical fibers to the BLMTC card, which processes the data from two front-end cards in parallel. The front-end card is designed to withstand an integrated dose of about 500 Gy, which is safe for the installation under the magnets in the arcs.

Nevertheless, the radiation levels expected in the locations, where most of the SEMs are installed are much higher, so the detectors in the straight sections are connected with long multi-wire cables (NG18) to the front-end cards located in the nearest alcove.

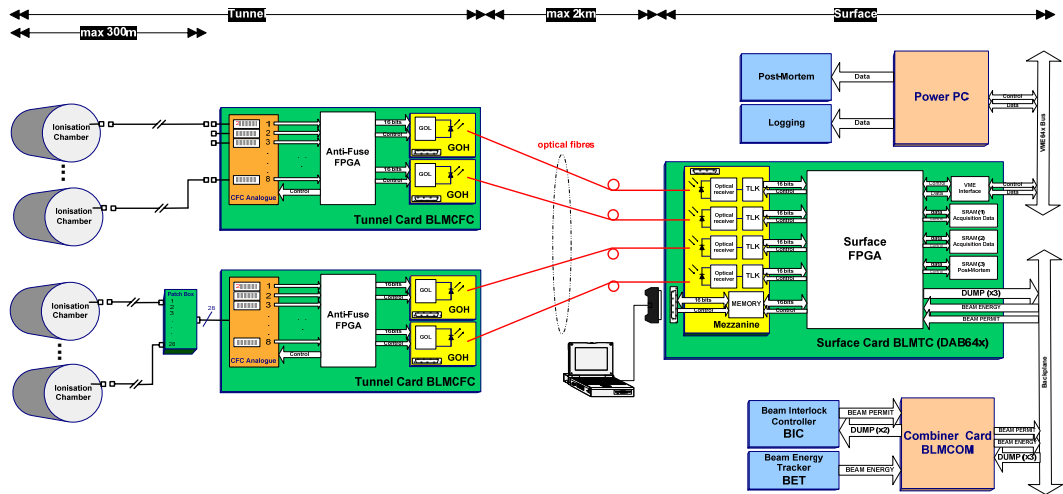


Figure 2.4: LHC Beam Loss Monitoring System Overview [50].

### 2.3.1 Analog Front-End

To measure the detector signal, a current-to-frequency converter (CFC) was designed, as it allows to reach a very high dynamic range while keeping a good linearity. It works on the principle of balanced charge and shown on the Fig. 2.5.

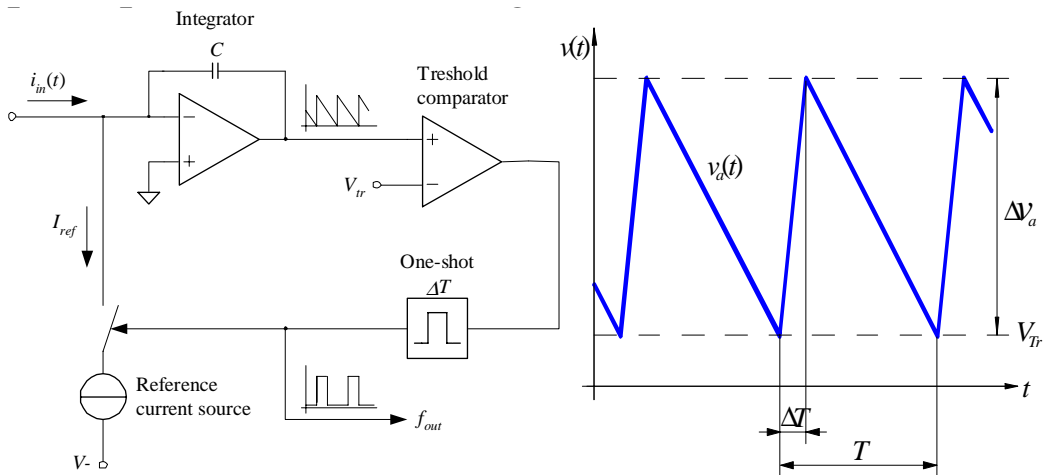


Figure 2.5: Principle of the charge balanced Current to Frequency Converter. From [21]

During the period  $T$ , the current induced by radiation in the detector is integrated. If a constant signal is applied, the integrator output ramps down with a constant slope. At the threshold level  $V_{Tr}$  the reference current  $I_{ref}$  is injected into the summing node of the operation amplifier for a fixed period of time  $\Delta T$  which resets the integrator output thus producing the so-called CFC count. The relation between the output frequency and the detector current is derived as:

$$f = \frac{\overline{i_{in}}}{I_{ref} \Delta T} \quad (2.1)$$

One of the benefits of using the CFC is the fact, that it does not have any dead time and therefore allows a continuous operation. When an input current is present during the reset of the integrator, it decreases the reference current  $I_{ref}$  and the next reset will come sooner thus increasing correspondingly the counting frequency. Each channel of the CFC is calibrated to the sensitivity of 200 pC/count using a calibrated current source.

When the input stage of the CFC is subject to a negative current, the counting process stops, because the voltage on the output of the comparator increases up to the saturation level of the operational amplifier. The CFC card is therefore equipped with a current source, which constantly injects 10 pA into the input stage thus avoiding the blocking of the CFC by low current noise. This current has to be considered, when very low currents are being measured. Additionally, an automatic negative current compensation procedure was implemented in the CFC card, which is triggered every time the operational amplifier is in saturation mode due to the negative current input for more than  $\sim 2$  minutes. The input offset current is then increased (up to maximum 255 pA) in steps until the measured current is at least +10 pA.

In order to extend the dynamic range of the CFC for very low currents, an additional Analog to Digital Converter (ADC) was added to the front-end card. The ADC measures the voltage on the integrating capacitor and its value is sent together with the data from the counter to the BLMTC card.

The CFC card is also equipped with a pair of protection diodes at the level of the input to the integrator. One of the diodes becomes conducting when a sufficiently large positive or negative current pulse saturates the amplifier and its input voltage reaches about 0.6 V.

### 2.3.2 Data Acquisition Board

The signal processing is performed outside of the LHC tunnel. The BLMTC processing module is a VME card that provides the necessary processing power and includes the

components for the optical link. The data sent from the tunnel include an ADC and a CFC counter value, which are combined together in the BLMTC card to a single number. The combined values are fed every  $40\ \mu\text{s}$  to the Successive Running Sums which allows to keep a history of the detector data. The measured values are converted to dose rate (Gy/s) by the corresponding calibration factors of the SEM or the ionisation chamber. All the produced sums are compared with the predefined threshold values. Due to the loss duration dependence of the quench levels (see Fig. 1.5) or damage thresholds, each running sum has a different threshold which is changing also with the actual beam energy. When a single value exceeds its threshold, the BLM system requests a beam dump. When the dump request is issued, the dedicated buffers with long data history are sent to the Post-Mortem analysis system.

### 2.3.3 Successive Running Sums

A constantly updated window is kept by adding the newest incoming value to a shift register and subsequently subtracting the oldest value. The number of values kept in the window which correspond to a certain period in time define the integration time of the window (see Table 2.1). This window is called Running Sum (RS). Multiple moving windows are cascaded to generate longer integration periods. This procedure minimizes the utilized resources.

The running sums from each BLM are transmitted to the LHC control center and the central logging system with a frequency of 1 Hz. The maximum value detected during the last second is transmitted for the windows with integration time shorter than 1 s (RS 1..8). The actual value of the integrals is transmitted for the longer running sums (RS 9..12). More details can be found in [50].

The maximum counting frequency of the CFC limits the number of counts integrated during  $40\ \mu\text{s}$  to 256, which corresponds to a continuous current of  $\sim 1.3\ \text{mA}$ . Due to the additional information from the ADC, one count is divided into 1024 bits. The dynamic range for the RS1 is then  $2.6 \cdot 10^5$ , while the dynamic range is larger for the longer running sums, as they can detect smaller currents.

## 2.4 Detection Requirements

In the SPS accelerator, the protection of the equipment is based on the BLM system (using ionisation chambers) and its empirical adjustments of thresholds. The main aim of the system is the protection against direct impact of the beam on the equipment and its subsequent activation. The beam dump thresholds are set according to the “operational experience” and no absolute calibration was done. The LHC BLM system has to protect the machine from the first moment with circulating beam and therefore

Signal Name	Time Window		Refreshing Rate [ms]	Data Type
	$\Delta t_i$ [ms]	$40 \mu s$ Steps		
RS1	0.04	1	0.04	max.
RS2	0.08	2	0.04	max.
RS3	0.32	8	0.04	max.
RS4	0.64	16	0.04	max.
RS5	2.56	64	0.08	max.
RS6	10.24	256	0.08	max.
RS7	81.92	2048	2.56	max.
RS8	655.36	16384	2.56	max.
RS9	1310.72	32768	81.92	sum
RS10	5242.88	131072	81.92	sum
RS11	20971.52	5242288	655.36	sum
RS12	83886.06	2097152	655.36	sum

Table 2.1: Integration periods of the Running Sums and their update frequencies.

it has to rely on loss simulations and full characterization of the detectors.

A very high operational reliability is needed because of the damage potential of the beam, which could damage a superconducting magnet causing an LHC downtime of several months.

The monitors have to be suitable for mixed radiation fields (for example not being sensitive just to neutrons) and radiation tolerant. The monitors working in the collimation areas are expected to integrate up to 70 MGy per year in the nominal conditions and still keep their operational parameters unchanged.

The dynamic range of the BLM system is determined at the lower end by the low quench level of the superconducting magnets and on the high end by the high loss rates expected in both collimation regions. The signal produced by the BLM detectors will span over 13 orders of magnitude.

The required very high dynamic range imposes the use of two detector types with different sensitivities as the same front end electronics is preferred to be employed. An ionisation chamber will cover the lower and mid range dose rates and a low response detector the very high dose rates with a small overlap in the mid range.

### 2.4.1 Ionisation Chamber

The parallel plate Ionisation Chamber (IC) [26] detector is the most common beam loss monitor at the LHC. In total 4250 ICs were produced in IHEP Protvino [44] and 3700 were installed in the LHC tunnel.

The chambers have an active volume of  $1.5 \text{ dm}^3$  and are filled with nitrogen at 0.1 bar overpressure. The electrodes are made of a 0.5 mm thick aluminium and spaced by 5.75 mm. Each signal electrode is surrounded by two bias electrodes maintained at 1500 V. The assembly is attached to the stainless steel shell via two very high resistivity ceramic ( $\text{Al}_2\text{O}_3$ ) plates, the electrodes are connected by two ceramic feedthroughs.

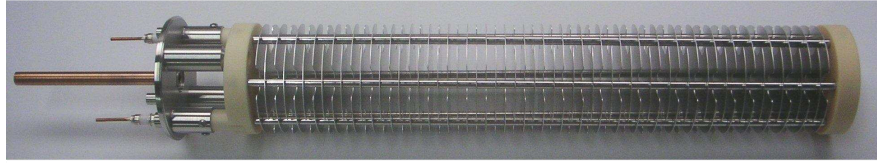


Figure 2.6: Inner assembly of the LHC Ionisation Chamber without the steel cover.

The thickness of the steel shell cylinder is 2 mm, the bottom and the top cover are 5 mm thick. The covers, feedthroughs and the copper pumping tube are welded in argon inert atmosphere (TIG).

The leakage current of each IC is individually tested and is usually below 1 pA at 1500 V. Each piece is also calibrated by using a strong gamma source ( $740 \text{ GBq } \text{Cs}^{137}$ ) in the CERN Gamma Irradiation Facility.

### 2.4.2 Low Response Detector

There are different approaches possible to reach a relatively small response yield for a radiation detector and the considered options will be shortly presented.

A very small ionisation chamber (IC) in the order of  $1 \text{ cm}^3$  would have a 1000 times lower response than the equivalent  $1 \text{ dm}^3$  IC, but its main disadvantage is the space charge effect limiting the usability to the same level as the standard IC BLM. It could be partially avoided by using a low pressure IC, but the saturation effect would again cause nonlinear behavior at high dose rates. Scintillators are known for their high dynamic range and very fast response, but suffer from darkening at high doses and require the use of optical detectors, which are normally not “radiation hard”. The state of the art silicon detectors used by ATLAS or CMS are radiation tolerant only up to  $1 \cdot 10^{15} p^+ / \text{cm}^2$  ( $\sim 1 \text{ MGy}$ ) and an improvement of two orders of magnitude can not be expected for the silicon technology. The large LHC experiments ATLAS and CMS are using the so-called Beam Condition Monitors (BCM) to estimate the radiation level inside the detectors. The BCM are based on the use of diamonds produced by the chemical vapor deposition technology as solid state ionisation detectors. The incident particles create electron hole pairs, which are separated by a bias field. The CVD diamonds were successfully measured [74] up to  $1.8 \cdot 10^{16} p^+ / \text{cm}^2$ , but even if they were still operational, their response dropped significantly and the signal to noise ratio

decreased as well. Another considered technology was the cryogenic micro-calorimeter [25]. It exploits a very strong temperature dependence of the resistivity of a carbon plate mounted inside the cryostat. Unfortunately, the response time is excessively long in the order of 150 ms.

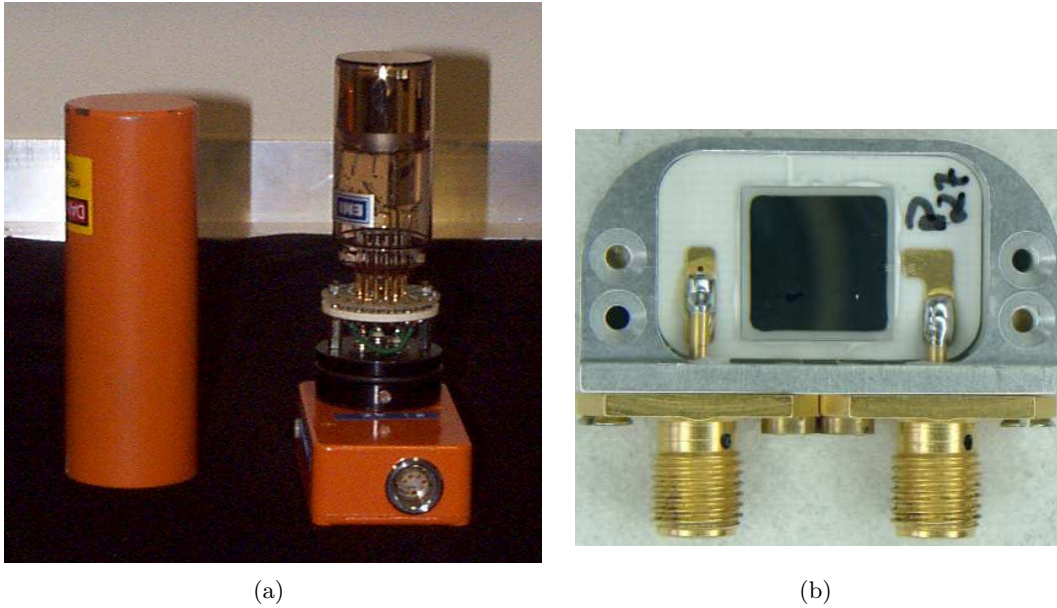


Figure 2.7: a) Aluminium Cathode Electron Multiplier is the standard beam loss monitor of the CERN PS and PSB areas. b) A photograph of the final CVD diamond module used by CMS for its beam condition monitoring system [74].

The Aluminium Cathode Electron Multiplier (ACEM) BLM detectors are presently used in the PS and were considered for the LHC. The low energy secondary electrons are emitted from an Al plate upon irradiation and multiplied by dynodes like in a photomultiplier. The ACEM has rather low dynamic range and a poor gain stability at higher doses requiring regular calibrations. Moreover, the multiplication part saturates at high dose rates, but the time response is very fast and would allow bunch by bunch measurements.

The most promising technology seemed to be based on the Secondary Electron Emission (SEE) process like in the ACEM detector but without the multiplication stage. A beam loss detector using this process was developed and will be described in the following chapters.

## Chapter 3

# Secondary Electron Emission

### 3.1 Energy loss by ionisation

When a charged particle passes through an absorbing medium, it predominantly interacts by coulomb forces with the electrons of the medium [36]. For hadrons, interactions with the cores of the atoms are generally possible (e.g. Rutherford scattering) but much less frequent. The projectile particle will transfer a part of its energy to the electrons it encounters along its trajectory. The electrons will either be excited to the higher energy levels or gain sufficient energy to leave the atom and therefore ionise it. The maximum energy  $T_{max}$  that can be transferred to a target electron in a single head-on interaction is given by the following formula.[2]

$$T_{max} = \frac{2m_e c^2 \beta^2 \gamma^2}{1 + \frac{2\gamma m_e}{M} + \left(\frac{m_e}{M}\right)^2} \quad (3.1)$$

Where  $\beta$  and  $\gamma$  are the relativistic factors,  $M$  is the mass of the projectile and  $m_e$  is the electron mass. The electrons produced by these close interactions are often called delta rays, but are much less frequent[35] than the low energy electrons coming from the distant collisions. For the heavy charged particles, one can safely assume that this is a continuous process as only a small fraction of the projectiles' energy is lost in each collision. The mechanism is usually described by the mean differential energy loss  $dE/dx$  (or by the stopping power  $S = -\frac{dE}{dx}$ ).

The energy loss of a muon in copper is illustrated on the Figure 3.1. The pattern is rather complicated, but can be divided into several parts and each of them described by a formula or a parametrization. The part above the break  $\beta\gamma \approx 0.1$  up to 500 is well described by the classic Bethe-Bloch formula, which is based on the electronic energy loss through atomic excitation and ionisation. For muons and pions, the radiative processes are dominating above the critical energy and can not be described by the Bethe-Bloch formula any more. A very similar situation happens for electrons and

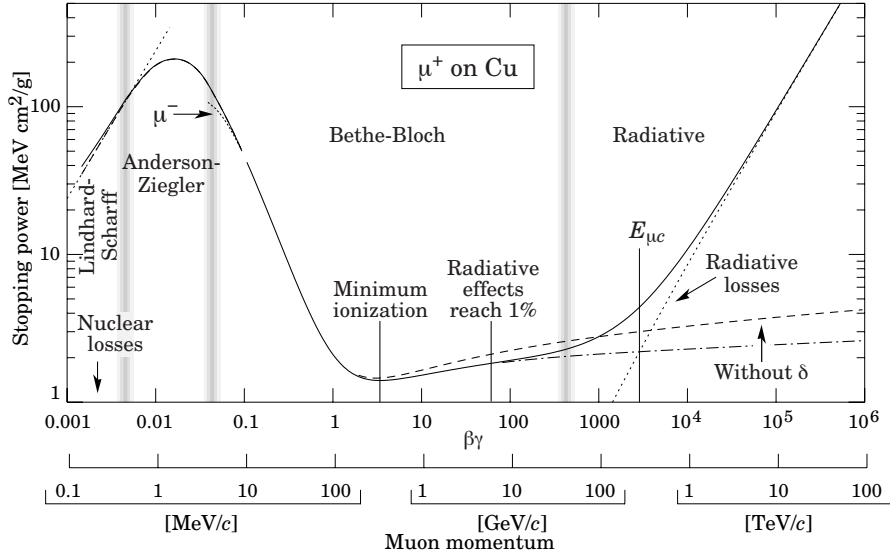


Figure 3.1: Stopping power ( $= \langle -\frac{dE}{dx} \rangle$ ) for positive muons in copper as a function of  $\beta\gamma = p/Mc$  over nine orders of magnitude in momentum (12 orders of magnitude in kinetic energy). Solid curves indicate the total stopping power. From [2].

positrons for which the bremsstrahlung (gamma emission caused by the passage through the field of the nucleus) starts dominating the ionisation above few tens of MeV for most of the materials.

The characteristic amount of matter traversed by a high energy electron in relation to the bremsstrahlung is called radiation length. It is defined as the mean distance over which a high energy electron loses all but  $1/e$  of its energy by bremsstrahlung [2].

The critical energy  $E_c$  for electrons can be defined for solids as the energy at which the ionisation loss per radiation length is equal to the electron energy[2]:

$$E_c = \frac{610 \text{ MeV}}{Z + 1.24} \quad (3.2)$$

where  $Z$  is the atomic number of the absorber. The critical energy for muons is defined as the energy at which the contribution of the ionisation equals the contribution of the radiative processes to the energy loss. For solids, it is defined as

$$E_{\mu c} = \frac{5700 \text{ GeV}}{(Z + 1.47)^{0.838}} \quad (3.3)$$

The Bethe-Bloch formula for the energy loss is written as [2]

$$-\frac{dE}{dx} = Kz^2 \frac{Z}{A} \frac{1}{\beta^2} \left[ \frac{1}{2} \ln \frac{2m_e c^2 \beta^2 \gamma^2 T_{max}}{I^2} - \beta^2 - \frac{\delta(\beta\gamma)}{2} \right] \quad (3.4)$$

where  $I$  is the mean excitation energy for the given absorber (varies from few eV for low  $Z$  to hundreds of eV for high  $Z$  materials),  $Z$  and  $A$  the atomic number and mass of the absorber,  $ze$  is the charge of the projectile,  $K/A$  is  $0.307075 \text{ MeV } g^{-1} \text{ cm}^2$  and the  $\delta(\beta\gamma)$  is a parametrized density correction factor necessary for highly relativistic particles.

### 3.2 Secondary Electron theory

When a charged particle passes through an interface of a solid material, very low energy electrons can be emitted from the surface by the Secondary Electron Emission (SEE) process. The SEE phenomenon was discovered already in 1902 by Austin and Starke[37] and since then extensively studied for many different target projectile combinations and kinetic energy ranges going up to the few MeV. The main parameter describing the SEE is the Secondary Emission Yield (SEY), which is the average number of electrons emitted when an incident projectile enters or exits a surface. An example of the differential SEY for different target materials can be seen on the Fig. 3.2. In general, the spectra maximum is reached for energies of few eV and a longer tail extends up to several tenths of eV.

The SEE process can be generally divided into three consecutive steps. After the electrons are generated, they can diffuse up to the surface and possibly exit the material.

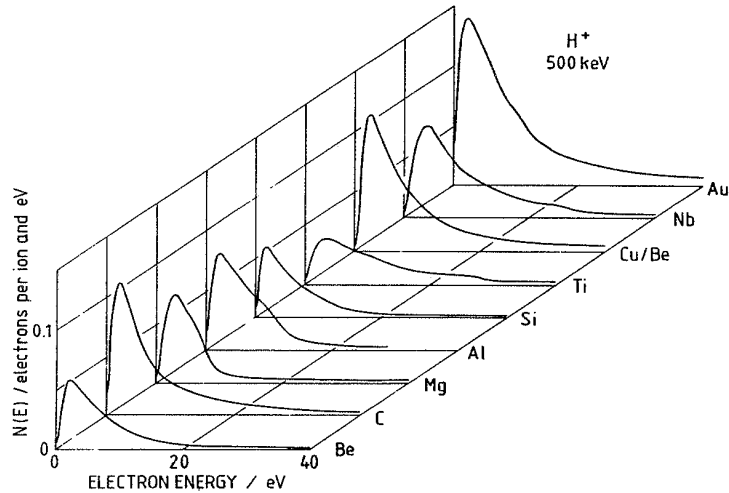


Figure 3.2: Low energy spectra  $N(E) = dSEY/dE$  induced by protons at 500 keV from different clean metals. From [5]

It was found by many authors, that the SEY for different projectile / target combinations is proportional to the energy loss rate  $dE/dx$  in the target material. A plot

summarizing the linear relationship over three orders of magnitude is shown on Fig. 3.3. It is important to note that the data were taken with incident charge states close to the mean charge state of the emerging ions.

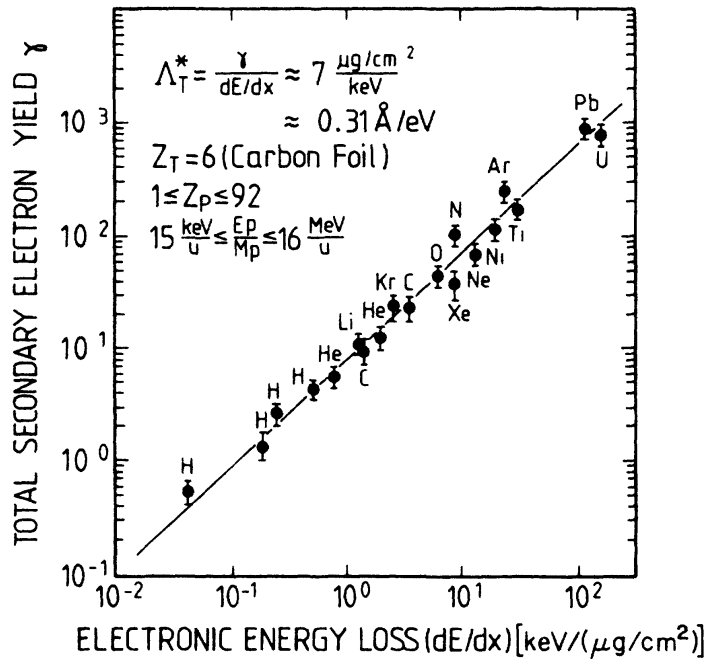


Figure 3.3: The total secondary electron yield  $\gamma$ , from carbon foils as a function of the electronic energy loss  $dE/dx$  of the projectiles [76].

### 3.2.1 Generation of Secondary Electrons in Solids

The first step in the SE creation is the production of the electron - ion pairs by a fast projectile in the bulk of the material. The dominant process is the ionisation as described in the previous section. The least energy is required to excite electrons from the conduction band above the Fermi level. The ionisations in the outer or even in the inner shells are less probable but also possible. If the projectile is an ion containing electrons in its shells, these ones can be stripped off and possibly induce further ionisations, but if it scatters out of the material, it can not be counted as a secondary electron. The electrons from the projectile will also interact with the target electrons and can cause ionisations without leaving the projectile.

The passage of the charged projectile leads to a certain extend also to the formation of the surface or volume plasmons along the track of the projectile. These collective excitations can decay in some cases by transferring the energy to a single low energy electron. The recoil atoms displaced during the knock-on interaction with the projectile

are capable to produce ionisations too, but the probability is very low compared to the direct ionisation process. When a rather low energy projectile passes through the solid, the ionisation electrons can get “captured” by the field of the projectile and form the so-called convoy electrons. They travel at the same velocity as the projectile and can be detected only in the forward direction (i.e. direction of the projectile). [4]

### 3.2.2 Diffusion process

When the low energy electrons produced by ionisations propagate through the solid, they strongly interact with other electrons and rapidly loose their energy. The energy loss rate of low energy electrons in Aluminium can be seen in the Figure 3.4. The peak loss occurs at about 30 eV (above conduction band), as the collective excitation process (generation of plasmon oscillations) peaks too. But for the electrons below 20 eV, the loss rate decreases and such electrons can therefore diffuse to larger distances.

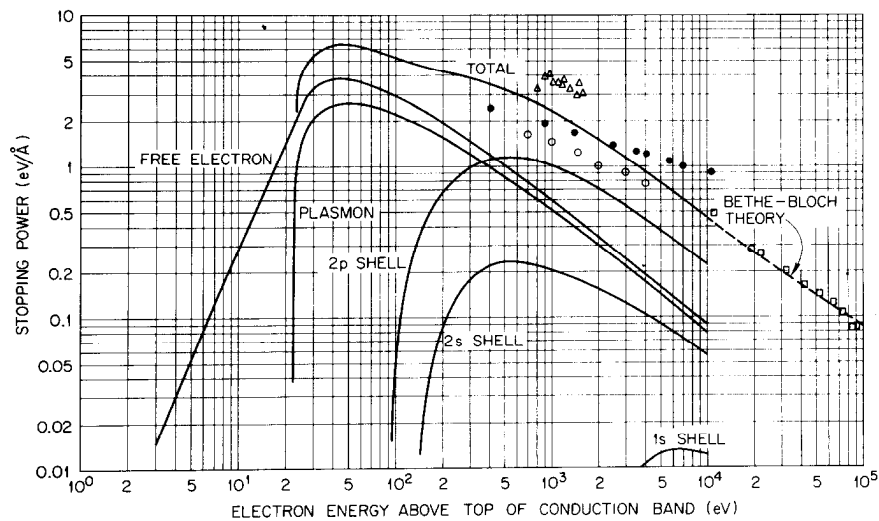


Figure 3.4: Stopping power of aluminum for electrons as a function of electron energy. Contributions to the total stopping power from inner-shell ionisation, plasmon excitation, and electron-hole pair excitation (free electron curve). From [40]

The fast energy loss permits only a very shallow penetration depth of the low energy electrons. In metals, the behavior of the conduction band electrons can be approximated by an electron gas and the excited electrons with higher velocities have to propagate by diffusion and by cascade multiplication create many low energy secondaries.

### 3.2.3 Emission process

Before a secondary electron is emitted from a metallic surface, it has to overcome the surface barrier potential, which is characterized by the mean work function  $e\Phi$  and the barrier height  $W = E_F + e\Phi$ , with  $E_F$  as the Fermi energy and  $\Phi$  as the surface potential.

The emission process can be regarded as a refraction phenomenon, as only the momentum vector normal to the surface (longitudinal) is lowered due to the barrier crossing and the transverse momentum is conserved. As a consequence, the electrons able to surmount the barrier with a given energy  $E_i$  inside the solid have a velocity vector lying inside an escape cone with a maximum angle  $\vartheta_{max}$  with respect to the surface normal[4]:

$$\vartheta_{max} = \arccos\left(\sqrt{\frac{W}{E_i}}\right); \quad E_i \geq W \quad (3.5)$$

Assuming an isotropic distribution of the low energy electrons inside the solid, the probability  $P(E)$  for a secondary electron with energy  $E = E_i - W$  outside the solid to penetrate the surface barrier is

$$P(E) = 1 - \frac{W}{E_i} = 1 + \left(\frac{W}{E}\right); \quad E_i \geq W \quad (3.6)$$

## 3.3 Semi-empirical theory of Sternglass

The theoretical treatment of the SEE by E.J. Sternglass was formulated in 1957 [10] and was used in a simplified form for generating the secondary electrons in the simulations presented later in this work. The theory is valid only for the backward emission (projectile entering the target).

Two main channels of the Secondary Electron (SE) formation are assumed. The low energy electrons produced by the small energy transfers to the target electrons during ionisation present the main contribution, whereas the fast delta electrons emitted mostly in the forward region can produce additional SE. The number of the low energy electrons produced in a depth  $x$  is approximated to

$$n_e(x, v)^{(1)} = \frac{1}{\bar{E}_0} \left\langle \frac{dE}{dx} \right\rangle^{(1)} \quad (3.7)$$

where  $\bar{E}_0$  is the mean energy loss per secondary formed and the  $\langle dE/dx \rangle^{(1)}$  is the mean differential energy loss going directly into the production of low energy sec-

daries. The number of the electrons produced by the delta electrons looks very similar to the previous equation.

$$n_e(x, v)^{(2)} = f(x, v) \frac{1}{\bar{E}_0} \left\langle \frac{dE}{dx} \right\rangle^{(2)} \quad (3.8)$$

The  $\langle dE/dx \rangle^{(2)}$  is now the energy loss going into the production of delta rays and  $f(x, v)$  represents the fraction of that energy available for the production of delta-ray caused electrons at the depth  $x$ . Sternglass makes use of the Bethe-Bohr equipartition rule[38] stating that half of the total ionisation energy loss goes in the formation of the delta rays and the second half to the production of the slow electrons.

The probability  $P(x)$  that an electron produced at a depth  $x$  can escape from the material follows an exponential behavior written as

$$P(x) = \mathcal{T} A \exp(-x/L_s) \quad (3.9)$$

where  $\mathcal{T}$  is a surface transmission coefficient.  $A$  is a constant related to the distribution of the initial velocities of electrons and to the number of collisions required to absorb the electron. The characteristic length  $L_s$  describing the diffusion of the low energy electrons (which is of the order of distance between inelastic collisions[10]) is obtained by

$$L_s = (\alpha' N \sigma_g)^{-1} \quad (3.10)$$

where  $N$  is the number of atoms per unit volume,  $\sigma_g$  is the cross section of the target atoms which can be parametrized by  $1.6Z^{1/3}10^{-16} \text{ cm}^2$  and  $\alpha'$  is a factor depending on the cross section of the SE scattering process. The differential Secondary Emission Yield (SEY) is now given by

$$dSEY = n_e(v, x) P(x) dx \quad (3.11)$$

where  $n_e = n_e^{(1)} + n_e^{(2)}$ , which reads after integration for low  $Z$  targets

$$SEY = \frac{1}{2\bar{E}_0} \left\langle \frac{dE}{dx} \right\rangle \mathcal{T} A L_s \left[ 1 + \left( 1 + \frac{L_\delta}{L_s} \right)^{-1} \right] \quad (3.12)$$

Sternglass estimated the mean energy  $\bar{E}_0$  lost per ion formed inside the solid to 25 eV. Also the coefficients  $\mathcal{T}$  and  $A$  should be constant for all the metals and were

estimated to  $\mathcal{T}A = 0.5$  and  $\alpha'$  was obtained from the available measurements of the  $L_s$ , which lead to  $\alpha' = 0.23$ . The ratio of the effective path lengths of delta electrons to low energy electrons was estimated in [39] to  $\frac{L_\delta}{L_s} = kE/A_p$ , with  $k \approx 5.4 \cdot 10^{-6} \text{ amu/eV}$  and  $E$  and  $A_p$  the kinetic energy and mass of the projectile.

If the above estimations are inserted into the Eq. 3.12 3.10, the following numeric relation is obtained

$$SEY = 0.01L_s \left. \frac{dE}{dx} \right|_{el} \left[ 1 + \frac{1}{1 + (5.4 \cdot 10^{-6} E/A_p)} \right] \quad (3.13)$$

$$L_s = (3.68 \cdot 10^{-17} N Z^{1/3})^{-1} [cm] \quad (3.14)$$

Please notice that the electronic energy loss should be in [eV/cm] and the projectiles' kinetic energy in eV.

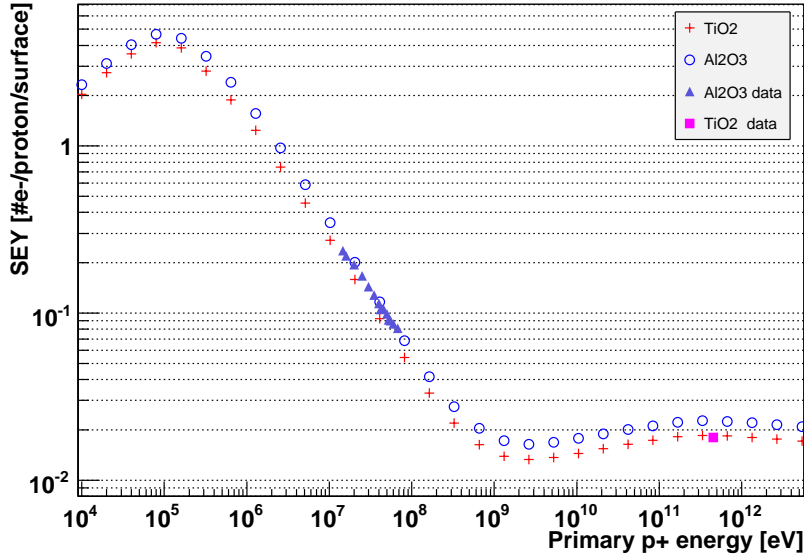


Figure 3.5: Modified Sternglass formula for true SEY of primary protons for different materials scaled by factor 0.8 to fit reference data[12, 13].

### 3.4 Angular dependence

In the treatment by Sternglass, the dependence of the SEY on the angle of incidence is regarded as a change of the effective penetration distance  $L_s$ . The distance  $L_s$  can be regarded as a thickness of the target from which the low energy electrons can escape. If the projectile impacts under an angle  $\theta$  other than normal, the effective track length of the projectile extends by the factor  $1/\cos$ , so the resulting SEY normalized to the normal incidence would be:

$$\frac{SEY(\theta)}{SEY(0)} = \frac{1}{\cos(\theta)} \quad (3.15)$$

This formula would be rather difficult to implement in the simulation model, because the resulting value for the grazing angles tends to infinite. Also the experimental values confirm the cosine dependence only up to about  $70^\circ$  and fall below the curve above this angle [4]. The recent measurements using primary electrons were showing a different angular dependence in the following form [75] (or [77]):

$$\frac{SEY(\theta)}{SEY(0)} = e^{\alpha(1-\cos(\theta))} \quad (3.16)$$

The value of the coefficient  $\alpha$  was measured to be about 0.5 for the surface conditioned by a large electron dose and was used in the implementation of the SEY model in this work. The corresponding curve compared with the standard  $1/\cos$  dependence is presented on the Fig. 3.6.

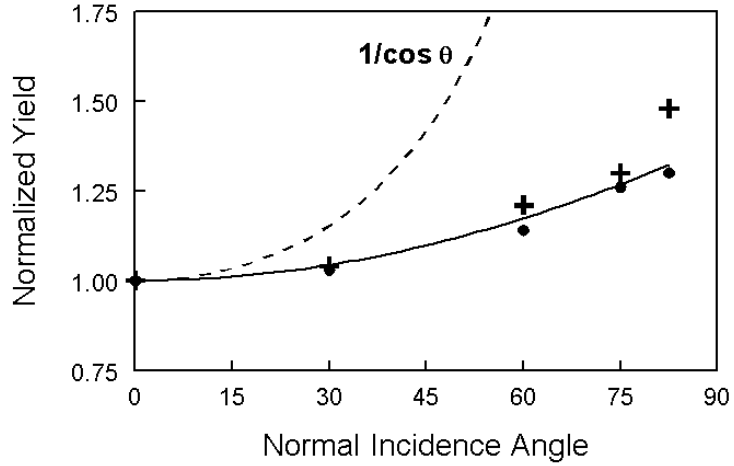


Figure 3.6: Normalized peak yields from TiN coated Al plates for  $\sim 400$  eV electrons impacting at different angles onto a cleaned surface (dots) and a surface additionally conditioned by large electron dose (crosses) [75]

### 3.5 Existing applications of the Secondary Electron Emission

The detectors based on the SEE are very well known in the beam instrumentation field of high energy accelerators. The beam current in the transfer lines is usually measured

by integrating produced SE from the thin aluminium or titanium foils placed in the vacuum beam pipe. The position of the beam in the extraction lines is also measured by the segmented SEE foils. This method can not be used in the circulating accelerators as the foils would be damaged by the intense beams.

The SEE process is exploited also by the Scanning Electron Microscopes [34], where the SE from the surface layers of the scanned material are emitted when the primary electron beam deposits locally the energy. As the SE come only from the surface layer, the produced images are very well suited for the 3D imaging. The standard photomultiplier tubes or multichannel plates use the very high SEY coefficient to generate many secondary electrons from one primary in each multiplication stage.

On the other side, a lot of effort is being done for reducing the SEY of the high luminosity proton accelerator beam pipe surfaces due to the Electron Multipacting process (electron cloud effect). The electrons present inside the beam pipe are accelerated by the very high electric field of the passing bunch and hit the inner wall, where they can produce additional electrons. These electrons will be again accelerated by the next bunch if the bunch spacing is short enough like the 25 ns for the LHC. The created cloud with a high density of electrons is interacting with the accelerated beam, leading to an emittance increase, betatron tune shift and various single or multi-bunch instabilities.

## Chapter 4

# Geant4 Simulations

In the high energy accelerator physics environment, two particle physics simulation codes are competing in some sense. The FLUKA[9] code usually gives very good results for the energy deposition studies like radiation shielding and dosimetry, where very high statistics for particle transport are needed. The GEANT4 is on the other hand more suitable for individual particle tracking and is the main choice for the LHC experiments. The radiation transport and shower simulations were performed by the BLM team in the past by GEANT3 and for the continuity reasons, GEANT4 stays the main tool for the radiation simulations within the team. Due to the requirement of precise tracking and electron production models, GEANT4 was chosen as the main code for modeling the response of the SEM.

### 4.1 Introduction to GEANT4 code

GEANT4 is an object-oriented Monte-Carlo particle physics simulation toolkit based entirely on the C++ language. Its development started in 1993 in a worldwide collaboration effort RD44 [6] and the first release was available in 1998. It is an open source project with updates released usually twice a year available on the official website[8] of the project.

The GEANT4 code is very complex as it can describe a considerably wide range of processes and yet is quite flexible and allows the user to modify the code and have a full control over the simulations. “Its kernel encompasses tracking; geometry description and navigation; material specification; abstract interfaces to physics processes; management of events; run configuration; stacking for track prioritization; tools for handling the detector response; and interfaces to external frameworks, graphics and user interface systems. Geant4 physics processes cover diverse interactions over an extended energy range, from optical photons and thermal neutrons to the high energy

reactions at the Large Hadron Collider (LHC) and in cosmic ray experiments. Particles tracked include leptons, photons, hadrons and ions. Various implementations of physics processes are offered, providing complementary or alternative modeling approaches. Moreover Geant4 provides interfaces to enable its users to interact with their application, and save their results. Visualization drivers and interfaces, graphical user interfaces and a flexible framework for persistency are included in the toolkit.” [7]

There are several steps required to be done by the user before a standalone application can be produced. It is mandatory to define the physics processes to be used for the given energy ranges by defining the so-called Physics List. The structure of the entities to be simulated has to be defined in the Detector Construction file together with the materials to be used. The main file calling the constructors of these classes and starting the Run manager has to be defined and also a random generator should be started within the main file. Additional User Actions can be defined in order to extract or control the required informations from different steps of the simulation. The application can be easily interfaced with another object oriented framework like i.e. ROOT, which was used in this work for saving and analyzing the data from the simulations.

#### 4.1.1 Hadronic models

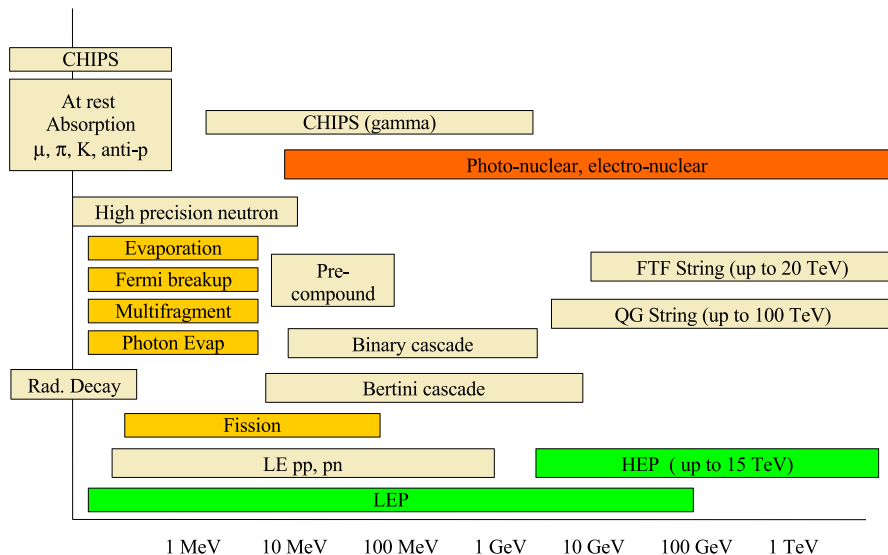


Figure 4.1: Overview of the GEANT4 hadronic model inventory. From [66]

Non-electromagnetic interactions of hadrons in GEANT4 are based on cross-sections and models covering a wide energy range. The predefined models are selectable by the user, which can often choose between simulation speed or greater precision. Most of the available models are summarized on the Figure 4.1.

When a high energy (above  $\sim 12$  GeV) projectile (proton, neutron, kaon or pion) interacts with a nucleus, the initial stage of the collision can be provided either by the Quark-Gluon String (QGS) model or by the Fritiof-like string (FTF) model, both of which are theory-driven and therefore rather CPU-time expensive. Another alternative would be the High Energy Parametrized (HEP) model derived from the GHEISHA parametrization previously used by GEANT3.

For the hadrons below  $\sim 10$  GeV, the Bertini-type cascade [68] or the Binary cascade are available. The later one is more CPU-time demanding and has a smaller energy validity range. After the initial collision, the nucleus is often left in a highly excited state. The de-excitation can be driven internally or for example by the Precompound model followed by other processes (like i.e. a fission or multi-fragmentation).

The small gap between the cascade type models and the string models is usually covered by the Low Energy Parametrized (LEP) model derived from the GHEISHA parametrization like the HEP.

The interactions of the low energy particles (below 20 MeV) can be treated by the High Precision (HP) processes for neutrons or the Photo-Evaporation routines, both of which are based on the specialized libraries with experimental data sets provided with the GEANT4 distributions. More details of the available processes can be found in [66].

#### 4.1.2 Electromagnetic models

The electromagnetic interactions are by default provided by the *G4EmStandardPhysics* [70] package. The detailed description can be found for example in [69].

“Geant4 standard electromagnetic physics provides a variety of implementations of electron, positron, photon and charged hadron interactions. Photon processes include Compton scattering,  $\gamma$  conversion into electron and muon pairs and the photo-electric effect. Electron/positron processes handle bremsstrahlung, ionisation and  $\delta$ -ray production, positron annihilation and synchrotron radiation. The energy loss process manages the continuous energy loss of particles due to ionisation and bremsstrahlung.” [6]

Some electromagnetic processes (bremsstrahlung and delta electron production by ionisation) in GEANT4 require a lower limit for the production of secondary particles, because the infrared divergence of these processes would otherwise cause a production of very large amounts of very low energy particles. Such behavior would extremely slow down the simulations and in majority of cases bring no further benefits. Hence gammas, electrons and positrons need a production threshold, which is expressed as a range cut-off. This distance is then converted into energy cut-off for each material

individually during the initialization phase. It is possible to define geometrical regions and attribute a different range cut-off for each of them.

### 4.1.3 Photo-Absorption and Ionisation module

The ionisation model of the standard GEANT4 EM package describes well the EM interactions of particles down to about 1 keV. Nevertheless, if the energy of the projectile should not be only lost and deposited in the media but also an electron should be produced and tracked, the standard package is not very suitable anymore. The Photo-Absorption Ionisation (PAI) module on the other hand handles correctly the production of the ionisation electrons down to about 250 keV effectively produces ionisation delta-electrons.

For a given length of track, the number of ionising collisions is simulated by the Poisson distribution with the mean number proportional to the total cross section of ionising collisions:[18]

$$\sigma_i = \int_{I_1}^{\omega_{max}} \frac{d\sigma_i(\omega')}{d\omega'} d\omega' \quad (4.1)$$

while the energy transfer in each collision is simulated according to the distribution proportional to:

$$\sigma_i(\omega) = \int_{\omega}^{\omega_{max}} \frac{d\sigma_i(\omega')}{d\omega'} d\omega' \quad (4.2)$$

where  $d\sigma_i/d\omega$  is the differential cross section of ionising collisions with the energy transfer  $\omega$  produced by a relativistic charged particle in matter,  $I_1$  is the first ionisation potential of the target material and  $\omega_{max} \sim 100 \text{ keV}$ . The differential cross section is expressed in terms of the photo-absorption cross section.

When the selected electron production cut is very low (i.e. below 1 keV), the computing time due to the production of many individual electrons by the PAI model can be drastically increased. The model has to be therefore activated only in a given region (physical volume) and it is recommended for use with only very thin absorbers or gases. In this work, the PAI model was activated in the Titanium electrodes, which allowed very reasonable simulating times.

### 4.1.4 Physics List

For practical reasons, the physics models suitable for a specific type of application are grouped into the so-called Physics Lists, which can be called by the user without further

changes or only its submodule (like i.e. the decay processes from the QGSP list) can be used.

The simulations of the secondary showers initiated by the lost protons of very high energies are very complex and require accurate (or reasonable in the unexplored regions) models from the maximum beam energy down to the thermal energies of neutrons. It was found to be quite difficult to match the simulated shower profile mainly at the longitudinal or transverse tails (see i.e. [26]), where most of the standard beam loss measurements occur. After discussions with the GEANT4 developers, it was decided to use the QGSP\_BERT\_HP physics list for the loss simulations, as it covers all the required energy range and most successfully reproduces the shapes of the experimentally obtained hadronic showers. The main disadvantage of this list is mainly its considerably lower speed compared for example to the LHEP list, which uses the fast parameterizations of LEP and HEP.

The chosen list uses the QGS model with the Precompound nucleus model and the Bertini cascade with the LEP parametrization in between them. The low energy interactions of neutrons are handled by the HP model. The list contains also the Standard electromagnetic package.

For reasons of continuity, the same QGSP\_BERT\_HP physics list is used for the model of the SEM, but without the standard EM package, because the additional PAI module was used and could not be initialized otherwise. The actual implementation of the physics list is based on the *G4VModularPhysicsList* where the following classes are called:

- PhysListParticles
  - constructs leptons, bosons, baryons, mesons, short-lived particles and ions
- HadronPhysicsQGSP\_BERT\_HP
  - implements hadronic physics as described earlier
- G4HadronElasticPhysics
  - implements the elastic interactions of hadrons
- G4DecayPhysics
  - handles the decay channels for all unstable particles defined in the physics list
- G4QStoppingPhysics

- processes for particles at rest (i.e. capture, annihilation or absorption)
- G4IonPhysics
  - implements inelastic processes and models for the deuteron, triton and alpha
- G4EmExtraPhysics
  - implements mainly the gamma-nuclear and electro-nuclear reactions
- PhysListEmModelPai
  - implements the basic EM processes together with the PAI module

The PhysListEmModelPai class defines the following processes for the selected particle types. The PAI module was activated as a part of the ionisation process only for the selected geometrical region, otherwise the standard ionisation model took place:

- gamma
  - photo-electric effect, Compton scattering, gamma conversion (pair production)
- electron
  - ionisation + PAI, Bremsstrahlung, multiple scattering (MSC)
- positron
  - ionisation + PAI, Bremsstrahlung, annihilation, MSC
- muon +/-
  - ionisation + PAI, Bremsstrahlung, pair production, MSC
- ions
  - ionisation, MSC
- other charged and not short lived particles
  - ionisation + PAI, MSC

## 4.2 Secondary Emission Model in Geant4

The Secondary Electron Emission (SEE) process is not implemented in any of the GEANT4 libraries. In order to accurately simulate the response of the SEM, a customized solution had to be created. It was decided not to create an additional process within the framework, as this approach would be very time consuming due to the surface nature of the phenomenon.

When the Secondary Electron (SE) is emitted from the surface of the signal electrode, it drifts in the electric field towards the positively biased electrodes. During the drifting process, the signal in form of a current pulse is generated. In order to correctly model such a behavior, the generation of the SE has to be implemented together with a dedicated signal readout procedure.

### 4.2.1 Choice of the Model

Due to the apparent lack of purely theoretical treatments of the SEE process, it was necessary to implement one of the available semi-empirical theories. Probably the most successful treatment in reproducing the measurements was published by Sternglass in 1957. The theory is described in Section 3.7.

The theory combines two main production channels of the SE into a single formula. The SEY is proportional to the  $dE/dx$  lost by electronic interactions and the mean penetration depth of the low energy SE. The production of the SE caused by the emitted delta electrons is added as a multiplication factor (see Eq. 3.14). In fact, as GEANT4 individually tracks all the produced particles, it is possible to separate the contribution of the delta electrons by considering them as primary particles, which can in their turn also create additional SE. The original formula was then simplified to the following form:

$$SEY = 0.01L_S \left. \frac{dE}{dx} \right|_{el} \quad (4.3)$$

with SEY standing for the probability of emission of a secondary electron when a projectile is traversing the surface of the material, the penetration distance  $L_S$  in cm is defined in the Eq. 3.14 and  $dE/dx$  in eV/cm. The validity is assumed to hold for all the charged particles, as the charge is the main parameter for the Coulomb interactions, so the validity should be limited only by the accurate knowledge of the  $dE/dx$ . It was shown in [72], that to modify the Sternglass formula to the case of electrons as projectiles, only the contribution of the backscattered primary electrons producing additional SE had to be included. This confirms the validity of our approach,

because the backscattered electrons will be again considered as projectiles and therefore can not be included in the equation.

It was further decided to assume, that every SE produced from the signal electrode will reach the bias plates and produce the same output signal. Due to the very low initial energy of the SE, they should be collected with a very high efficiency due to the relatively high bias field strength. The integral of the resulting current pulse will be the elementary charge of the electron. Under these assumptions, it is not necessary anymore to produce the individual SE and track them in the electric field, which largely simplifies the model. The energy or the emission angle does not have to be attributed to the SE and it can be in fact only counted as a unit signal (elementary charge).

### 4.2.2 Parametrized generation of Secondary Electrons

The custom Monte-Carlo SE generator is based on the Equation 4.3 specified above and was implemented inside the `G4UserSteppingAction` class, which is evoked every time a particle moves (makes a step) during the tracking. Every time a charged particle crosses an interface Vacuum /  $TiO_2$  of the signal electrode in either direction, the probability of the SE emission (SEY) is calculated and a random number is generated. If the number falls below the value of the SEY, one SE is recorded as a signal for the corresponding side of the electrode.

The SE are in reality emitted also from the bias electrodes, but they are forced to return to the electrode by the electric field and therefore do not contribute to the signal.

In order to calculate the SEY, the electronic  $dE/dx$  has to be calculated. The `G4EmCalculator::ComputeElectronicDEDX` function is used for this purpose. It needs three input parameters: the kinetic energy of the projectile, the particle type and the material type, which are all extracted from the `G4Track` class. This approach gives the correct electronic  $dE/dx$  (energy lost into the non radiative interactions) for example for protons.

For some particles nevertheless, a correction is required, because the  $dE/dx$  calculated by the `ComputeElectronicDEDX` function includes also the contribution from some radiative processes. The produced gammas do not contribute directly to the SE creation, but like for example the neutrons, they have to interact first by producing charged particles, which are then able to produce SE. Consequently, when the projectile is an electron or positron, the  $dE/dx$  from the Bremsstrahlung process has to be subtracted. The contribution is calculated by the function `G4EmCalculator::ComputeDEDX`, with the process name as the extra parameter ("eBrem" for Bremsstrahlung of electrons). The same process has to be subtracted for the case of muons ("muBrems"). At high

energies, the dominating radiative process for muons is the  $e^-/e^+$  pair production, so it has to be subtracted as well ("muPairProd"), otherwise an important rise of the SEY for the relativistic energies is observed.

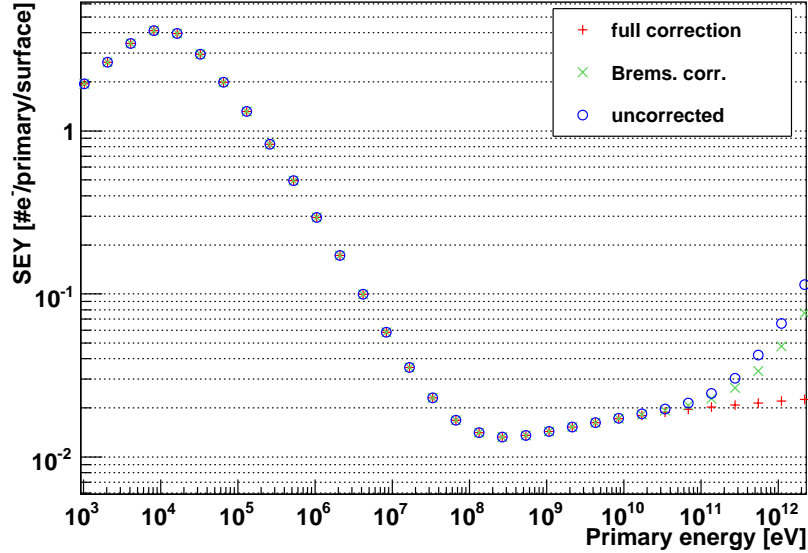


Figure 4.2: Secondary Emission Yield of  $\mu^+$  hitting the  $TiO_2$  surface for different methods of  $dE/dx$  calculation.

An example of the resulting SEY curves can be found on the Figure 4.2. The uncorrected curve has the  $dE/dx$  calculated just by the `ComputeElectronicDEDX` function, while the middle curve has only the contribution of the Bremsstrahlung subtracted and the last one has also the pair production subtracted from the  $dE/dx$ .

### 4.2.3 Charge balance and signal generation

The low energy secondary electrons produced by the custom parametrization form only a part of the resulting signal of the SEM. When a projectile passes through the signal electrode, the high energy  $\delta$  electrons are produced by the PAI model mostly in the forward direction. These electrons are produced also in the bias electrodes and if they do not have enough energy to penetrate the signal electrode, the contributions from the ones produced in the bias and in the signal electrode should statistically cancel out, because they produce opposite signals as illustrated by the particle (1) on the Figure 4.3. The negatively charged particles traveling from the signal to the bias electrode (like the SE) produce a positive pulse, hence if they travel towards the signal electrode against the direction of the bias field, the pulse has to be negative. The  $\delta$  electrons can travel against the bias field because their energy is mostly higher than the applied

1.5 keV.

On the other hand, if the  $\delta$  electrons start penetrating the signal electrode, which happens beyond  $\sim 420$  keV, the  $\delta$  electrons produced in the signal electrode still give a positive pulse, but the ones produced in the bias electrode generate subsequently a negative and a positive pulse, which cancel each other. The same cancellation happens also for all the charged primary particles, if they do not get absorbed within the signal electrode. As a result, the high energy electrons emitted from the signal electrode produce a net positive signal.

On the other hand, if the  $\delta$  electrons start penetrating the signal electrode (see particle (2) on Fig. 4.3), which happens beyond  $\sim 420$  keV, they generate subsequently a negative and a positive pulse, and therefore cancel each other, but the  $\delta$  electrons produced in the signal electrode still give a positive pulse. The same cancellation happens also for all the charged primary particles, if they do not get absorbed within the signal electrode. As a result, the high energy electrons emitted from the signal electrode produce a net positive signal.

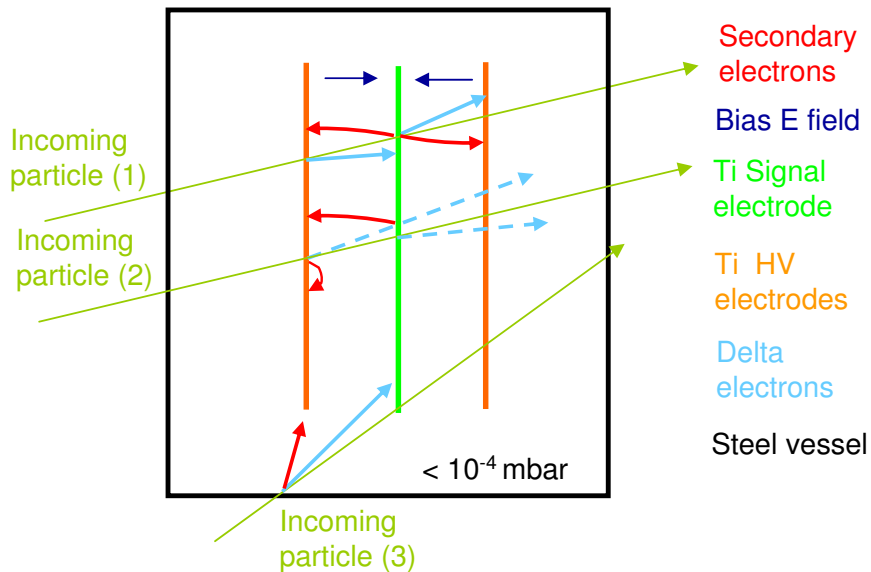


Figure 4.3: Schematic illustrating the contribution of different particles to the response of the SEM. The dashed line delta electrons have enough energy to penetrate the electrode.

Another possible source of signal within the SEM are for example the electrons emitted from the steel walls beside the electrodes (initiated by particle (3) on Fig. 4.3). The SE produced from the wall travel directly to the bias electrode, because the wall is at the same potential as the signal and will not create any signal in the measurement chain. The  $\delta$  electrons on the other hand can hit the signal electrode directly without

passing through the bias plate and if absorbed create a negative signal. A very similar situation happens if a primary particle enters the gap between the electrodes from the side (like the particle (3) on Fig. 4.3) and crosses only one gap. The response will depend on its charge and direction and does not have to be a unit signal in this case, because the gap can be crossed only partially.

In case a positively charged primary particle has just the right energy to get absorbed inside the signal electrode, it will produce a net positive signal as no cancellation occurs. In the same way, a negatively charged particle will give a negative signal.

One possible way to simulate all the above mentioned effects is to integrate the track length of all the charged particles between the electrodes, respectively the longitudinal component of the track perpendicular to the surface of the electrodes. The contribution of the various charged particles will then be equal to the total integral divided by the distance between the electrodes to assure the unit contribution of a charged particle leaving the signal and reaching the bias electrode.

An alternative simplified approach is possible, if the number of all the charged particles entering and leaving the signal electrode is registered. The particles have to be registered with their charge and the resulting signal  $S_Q$  calculated by the charge balance will be

$$S_Q = Q_{IN} - Q_{OUT} \quad (4.4)$$

where  $Q_{IN}$  is the total charge entering and  $Q_{OUT}$  the charge exiting the signal electrode. The charge balance was found to give more consistent results than the track integration method. This method was used in all the simulations for generating the signal, which was added to the contribution of the parametrized secondary electrons.

The same charge balance method was applied also for all the metallic components connected to the signal electrode, because they also contribute to the signal formation. For example a delta electron leaving the copper wire of the signal feedthrough will reach either the vacuum vessel or the bias electrode, which would produce in both cases a positive signal.

#### 4.2.4 Model Calibration

After the model for the secondary electron generation was chosen, it was necessary to compare the available published SEY data produced by a simple setup preferably at high energies with the output of the simulation.

The available literature data covering primary energies of more than just a few MeV are considerably rare. Concerning the materials, Aluminium (respectively  $Al_2O_3$ ) was

considered for the construction of the SEM and also the  $TiO_2$ . The available publications with the highest primary proton energies were produced by Borovsky in 1988[71] up to 24 MeV and by Castaneda in 1997[12] up to 67.5 MeV. The CERN report[30] was used as a next calibration point for very high energies, as it was carefully measured at proton energy of 450 GeV.

The experiment from Borovsky was using a simple rotating target holder in high vacuum of maximum pressure  $2.7 \cdot 10^{-5}$  mbar. The targets (Al covered by  $Al_2O_3$  and Ag target) were thick enough to stop completely the projectiles and the secondary emission current was simply measured by subtracting the beam current from the current between the target and the ground. It was found that the bias voltage of 20 V allowed a collection of about half of the SE, but already at 80 V, all the SE were collected. The experiments were conducted using a bias voltage of 300 V.

The experiment of Castaneda was conducted using two bias and one signal  $25.4 \mu m$  thick  $Al_2O_3$  covered Aluminium foils in high vacuum of about  $1 \cdot 10^{-6}$  mbar. A Faraday cup was placed downstream the foils to measure the total beam current. The secondary emission current was measured directly by a Keithley 485 pico-ampermeter connected between the signal electrode and the ground. The SE were produced from both sides of the signal foil but apparently only half of the signal is presented as a result, as the author compares the data directly with the Sternglass theory and the data of Borovsky, which are both obtained for the projectile entering the surface and not exiting.

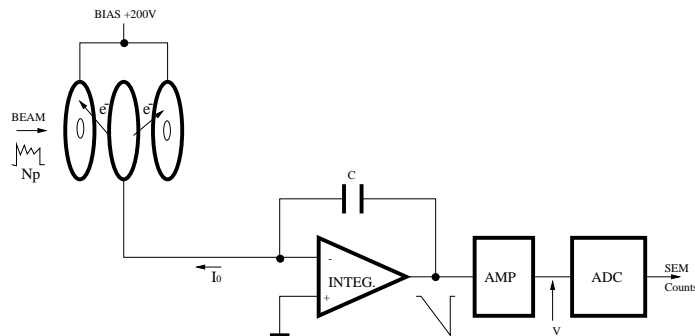


Figure 4.4: Schematic of the SEM beam current monitor in the North experimental area of CERN and its readout chain[30].

The CERN calibration data were obtained with a secondary emission beam current monitor placed in the 450 GeV extracted proton beam in the North experimental area of CERN. The  $20 \mu m$  titanium signal foil was covered with  $TiO_2$  as it was exposed to air during installation. The two surrounding bias foils (set to 200 V) were hollow in the middle as illustrated on the Fig. 4.4 in order to not generate additional delta

electrons and also inhibit the signal contribution of the delta electrons produced in the middle foil and ejected in the forward direction. In order to increase the precision of the measurements, the foil activation method and cross calibration with high precision beam current monitor were employed, so the final measurement error was 2%. The secondary electrons were emitted from both sides of the foil, the result was therefore divided by two assuming a symmetric emission yields.

All the above described data sets were included in the same plot and compared with the simplified Sternglass formula 4.3 for primary protons hitting the titanium or aluminium oxide. The systematic difference between the data points and the Sternglass curve was found to be 20%, so a calibration factor ( $C_F$ ) 0.8 was added to the formula. The result is presented on the Fig. 4.5.

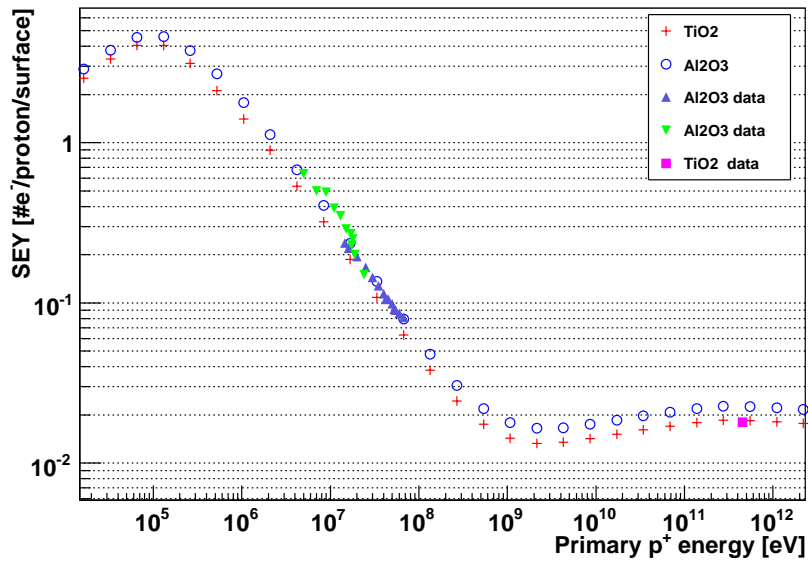


Figure 4.5: Secondary Emission Yield calculated with calibrated Sternglass formula and compared with published data. The oxidized Aluminium data are from [12] (blue triangles) and from [71] (green triangles) and the oxidized Titanium data point (violet square) is from [30].

#### 4.2.5 Detector geometry

The geometry of the prototype F was implemented in the `G4DetectorConstruction` class and used for the simulations of the test beam experiments. This design is very similar to the final production SEM, so it is supposed to be also a good approximation of the detector installed in the LHC.

The geometry of the detector is presented in the Fig. 4.6 as a transparent view and

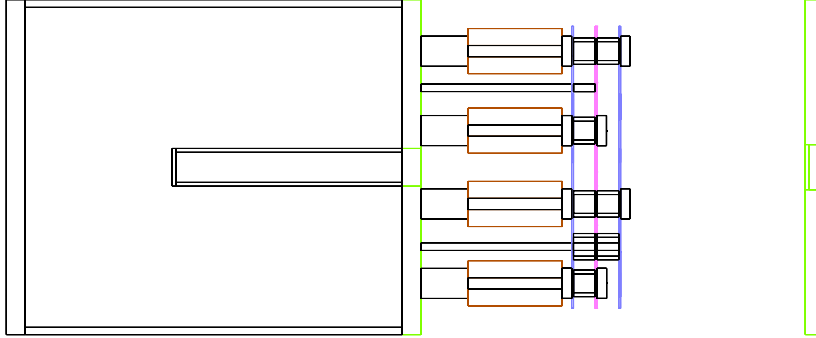


Figure 4.6: SEM geometry implemented in GEANT4 shown from the side.

on Fig. 4.7 as a shaded model. The blue Al bias electrodes are surrounding the violet Ti signal electrode. The surfaces of the signal electrode are covered by a 200 nm thick layer of  $TiO_2$ . The steel parts have a gray color except for the cover plates shown in green. The bottom cover includes a circular dip with a 0.5 cm radius and a thickness of 1 mm centered to the axis of the detector. The top cover contains a pumping hole of a 0.5 cm radius connected with a copper pumping tube. The implementation of the electrode holders was simplified by using the ceramic (brown) middle part and steel outer parts. The holders are connected to the electrodes with steel spacer tubes and fixed with screws. The electric feedthroughs except the copper wires were not implemented in the model. One wire is connected to the signal and one to the bias electrode.

The space inside the vacuum vessel is filled by air (nitrogen and oxygen) at  $10^{-6}$  mbar pressure. The static bias electric field of  $\pm 2600$  V/cm is applied in the cylindrical space between the electrodes.

The definitions of the basic materials were taken directly from the NIST[79] tables included in GEANT4. The compound materials like steel or alumina ceramics

When the production curves for the final SEM were produced, only the thickness of the electrodes were changed from 0.5 mm to 0.25 mm and the material of the bias electrodes was changed from Al to Ti.

#### 4.2.6 Electrode thickness dependence

During the final design phase, it was necessary to estimate the impact of the electrode thickness on the signal yield of the SEM. It is clear that the material thickness has no direct influence on the SEY of the detector as it is strictly a surface phenomenon.

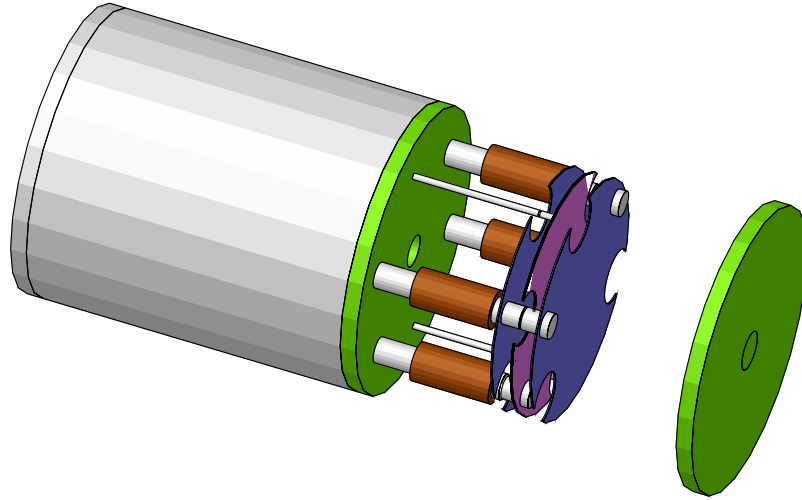


Figure 4.7: SEM geometry implemented in GEANT4. The steel vacuum cylinder is invisible.

Nevertheless as the thickness of the electrode increases, the projectile loses more energy and at low impact energies, the loss can induce a significant difference between the SEY upon entering and exiting the electrode.

The dependence of the detector response on the thickness of the electrodes was simulated. The thickness of all the electrodes was varied from  $1 \mu\text{m}$  to  $1 \text{mm}$  and the result for a round Gaussian  $1.4 \text{ GeV}$  proton beam is presented on the Fig. 4.8. The red points were calculated with the standard method by adding the parametrized SE to the charge balance signal. The blue points were obtained only by counting the parametrized SE. Every point was produced by averaging the result of 5 runs, each with 10000 primaries.

The delta electron production scales directly with the thickness of the electrodes, because of their origin in the bulk of the material. Most of the delta electrons produced in the signal electrode contribute to the charge balance signal due to their high energy. When the number of the delta electrons increases, the number of the secondary electrons produced by the delta electrons increases as well, so it seems like an increase of the SEY as it can be observed on the plot. On the other hand, the response of the SEM is entirely dominated by the SE for the thicknesses in the order of few microns, because of the low delta electron emission probability.

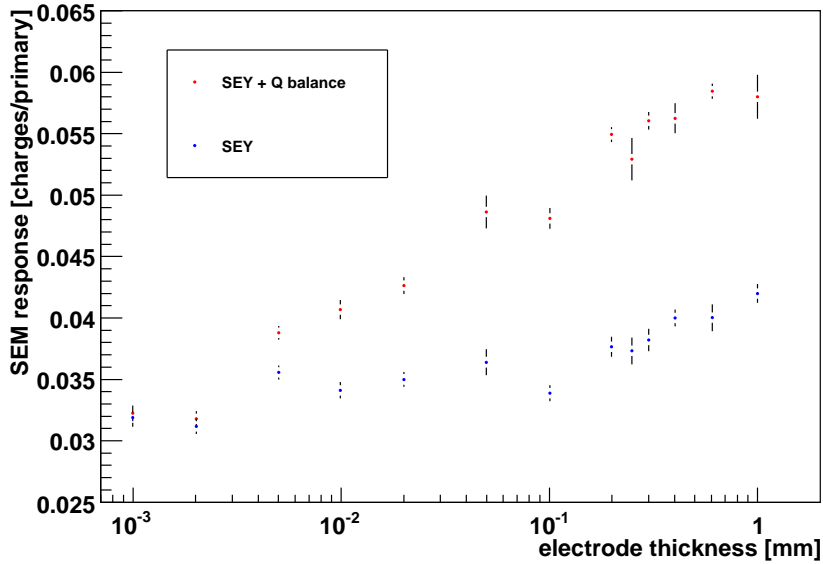


Figure 4.8: Simulated response of the SEM for different thicknesses of the electrodes for 1.4 GeV protons. Response was calculated using only the “true” secondary electrons or also the charge balance on the signal electrode.

#### 4.2.7 Range cut-off dependence

In GEANT4, the ionisation process needs a threshold for the production of delta electrons to avoid infrared divergence, as described earlier in this chapter. The range cut-off controls the number of the produced delta electrons, therefore it has a direct impact on the simulated response of the SEM and is in fact the only free parameter of the simulation model. The parametrized generation of the SE does not depend on the cut-off value, because the  $dE/dx$  is calculated by the `ComputeElectronicDEDX` function, which does not take into account the cut-off selected in the simulation model.

The comparison with the published data allowed only the calibration of the secondary emission model, so the cut-off parameter had to be found by the calibration measurements of the SEM. The first available calibration measurement was obtained with the 62.9 MeV proton beam (see Fig. 6.8) and was reproduced by the simulations using different cut-off values. The simulated circular proton beam had a sigma of 10 mm and energy of 62.9 MeV. The resulting simulation data with the response calculated only from the secondary electron parametrization and also with the delta electron contribution are shown on the Fig. 4.9. By comparing the result of the measurement ( $0.27 \pm 0.014$  charges/primary) to the simulation, an optimum value of  $9 \mu\text{m}$  was found and used later in all the simulations. This value corresponds to the cut-off

in energy of 40.1 keV for  $e^-$  in Ti and of 1.2 keV for gammas.

It can be seen for the cut-off values larger than  $12\ \mu m$ , that the response of the SEM slightly decreases, if the charge balance is included. This effect is caused by the constant cut-off value of  $10\ \mu m$  applied in the other parts of the detector (mainly in the bias electrodes) and for the cuts higher than this value, the number of the electrons impacting on the signal electrode is larger than the number leaving it. If the cut in the bias electrodes changes as well, the contribution of the charge balance stays positive.

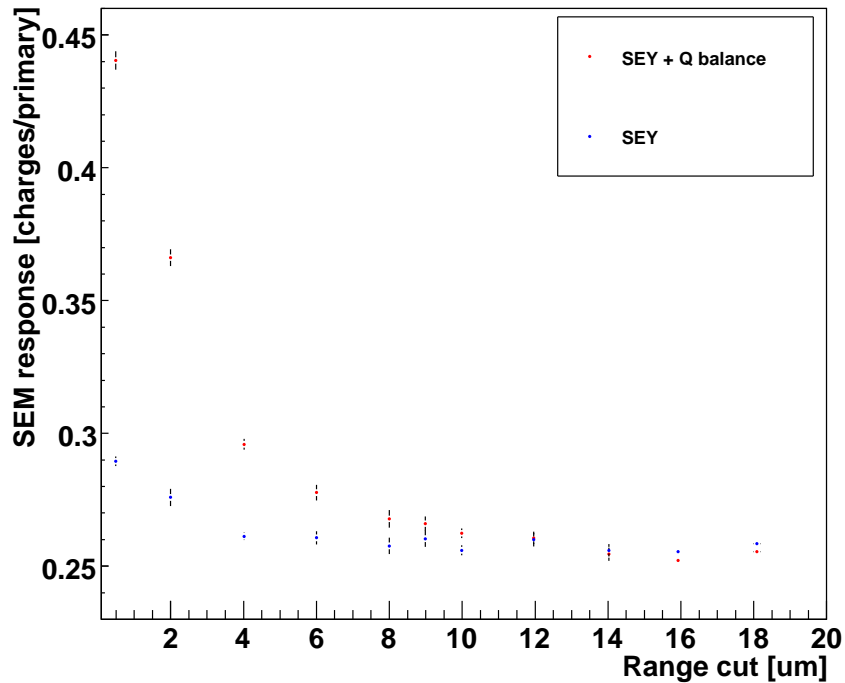


Figure 4.9: Simulated response of the SEM for different range cut-off thresholds. Values for 62.9 MeV protons impacting on the bottom plate. The default cut-off used in all the simulations is  $9\ \mu m$ .

For comparison, the same type of plot was produced for the 1.4 GeV proton beam to simulate the experiment in the PS Booster (see Fig. 6.10). It can be seen on the Fig. 4.10, that the contribution of the delta electrons is constant and therefore the response of the SEM does not vary for the cut-off values larger than  $9\ \mu m$ , which is caused by the relatively high energy of the emitted delta electrons.

#### 4.2.8 Response for different particle types

The SEM detector will be used mainly in the mixed radiation fields of particle showers (i.e. after the collimators) created by the lost primary protons. It is therefore necessary

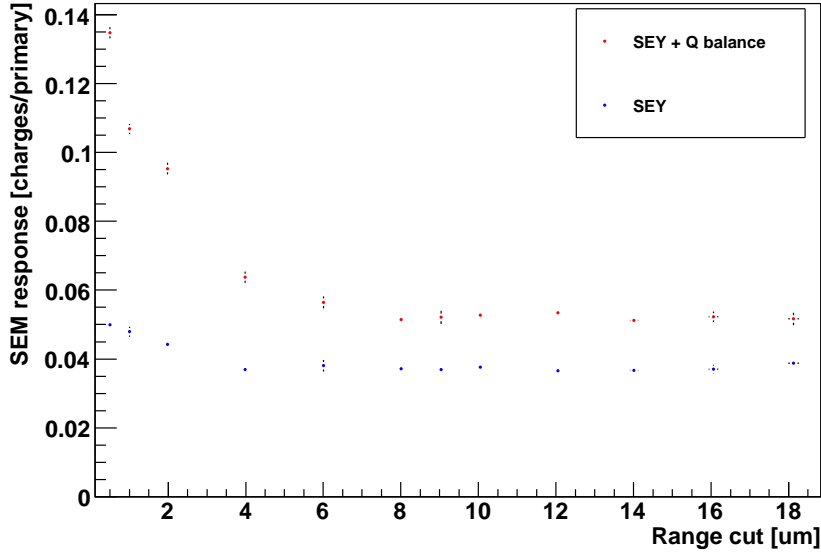


Figure 4.10: Simulated response of the SEM for different range cut-off thresholds. Values for 1.4 GeV protons impacting through the bottom plate.

to predict the response for a wide energy and particle type range. These curves will be used for generating the beam abort request thresholds. The Figure 4.11 shows the result of simulations using GEANT4.9.0 and a round gaussian beam impacting on the center of the bottom plate. The signal was generated by summing the parametrized secondary electrons and the charge balance contribution. Each simulation point is obtained by averaging the result of 10 runs with 10k or 5k primaries each. The values between two simulation data points are obtained by linear interpolation.

When a primary particle has just the right energy to get fully absorbed inside the signal electrode, the output is dominated by the charge balance. If the charge of the particle is negative, its charge balance contribution will be negative as well. Such effect can be observed for the electrons of approximately 8 MeV, but the negative peak is quite low because many electrons will be elastically scattered and will not enter the electrode. It is clear, that electrons of even lower energy will be absorbed already in the bias electrode and their response beyond this energy will be nearly zero. It will not be completely null, because the statistical fluctuations in the electron energy loss will allow some electrons to reach the signal electrode.

The charged hadrons show a relatively sharp threshold behavior due to a much lower energy loss straggling in contrary to i.e. electrons. When a proton has the kinetic energy of up to around 40 MeV, it will be absorbed within the steel bottom cover plate or the

bias electrode. If its energy is slightly increased, it will reach the middle electrode with a very low residual energy and therefore a very high  $dE/dx$  and consequently a very high SEY. The positive charge balance during absorption will increase the peak for the protons.

The signal rise for hadrons at very high energies is caused by the hadronic interactions initiated in different parts of the detector, mainly in the steel walls. The secondary particles from the interactions can then produce more secondaries than a single particle. The error bars for these energies are rather high due to a small number of events with a very large number of secondaries and thus a large signal contribution.

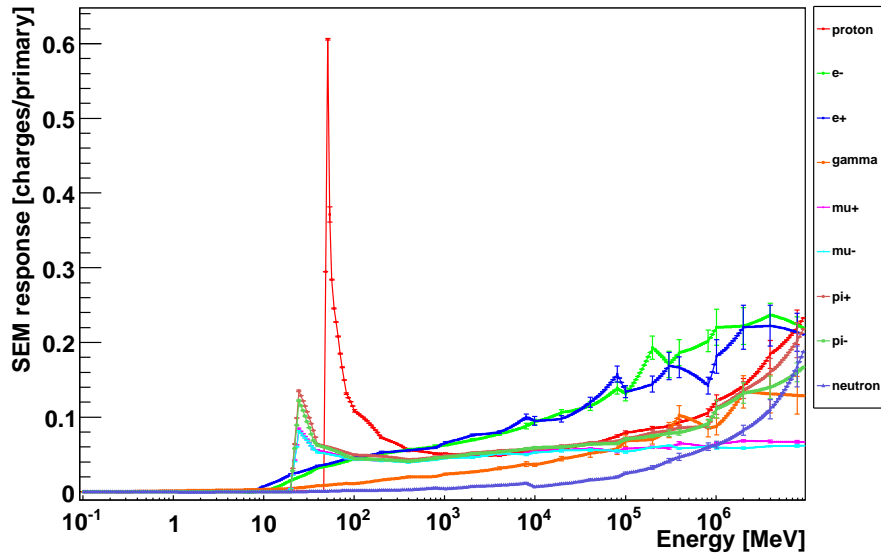


Figure 4.11: Simulated response curves for the main particle types and wide energy range.

As mentioned previously, the neutral particles can not produce SE directly and first have to undergo an inelastic interaction and the produced charged secondaries have to reach the signal electrode, where the SE can be finally generated. The response of the SEM to these particles is therefore considerably lower than for the charged ones. Moreover, the neutral particles do not present a sharp absorption threshold and contribute even at low impact energies as it can be seen for neutrons and gammas.

### 4.3 Estimation of the SEM signal in the LHC dump region

The LHC beam dumps are one of the most critical elements for the operation of the accelerator. They were designed to withstand the impact of the ultimate intensity LHC

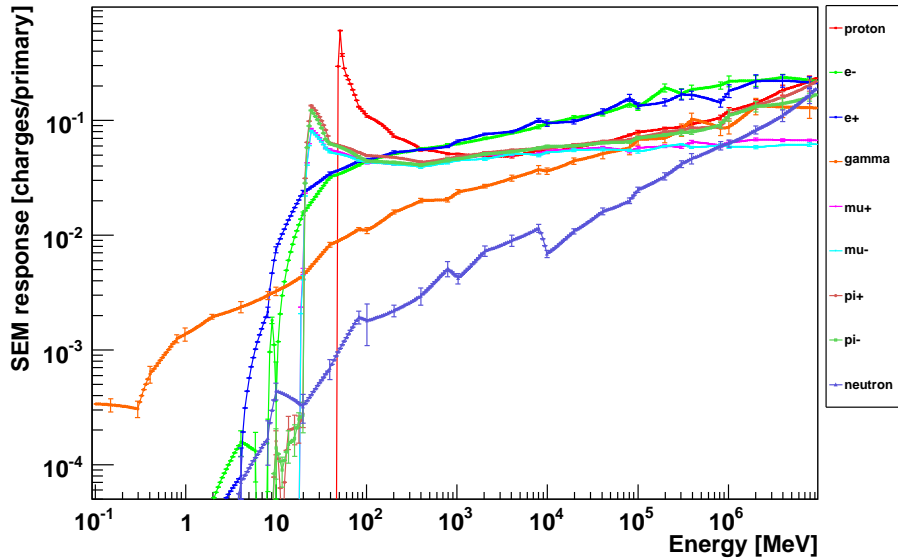


Figure 4.12: Simulated response curves for different particle types and wide energy range produced with uniform irradiation of the bottom plate.

beam at 7 TeV even if all the dilution kickers fail and the beam is very narrow. The parameters nevertheless do not present a big safety margin and the 7 TeV simulations were based on the extrapolations from the known data with a maximum of 1 TeV.

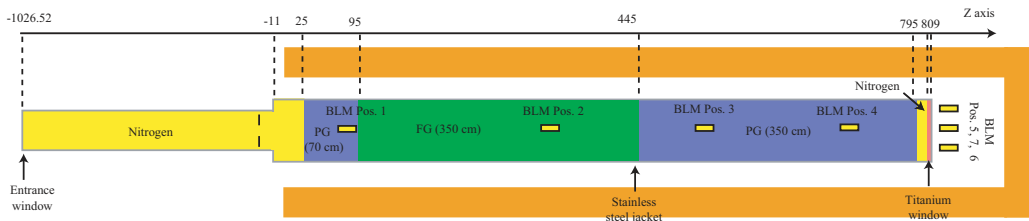


Figure 4.13: Layout of the LHC beam dumps as implemented in FLUKA for the calculations of energy deposition and particle spectra at the BLM locations [19].

To monitor the integrity of the dump setup seven SEM detectors were installed around the dump core. Their placement is shown on the Fig. 4.13. Four chambers are placed just below the core along the longitudinal axis of the dump, where they should measure the radiation proportional to the longitudinal profile of the hadronic shower. Three chambers are located behind the end face of the dump and should measure the fluence of particles leaking from the core in the direction of the original beam.

The radiation field simulations of the dump were performed in the Fluka program

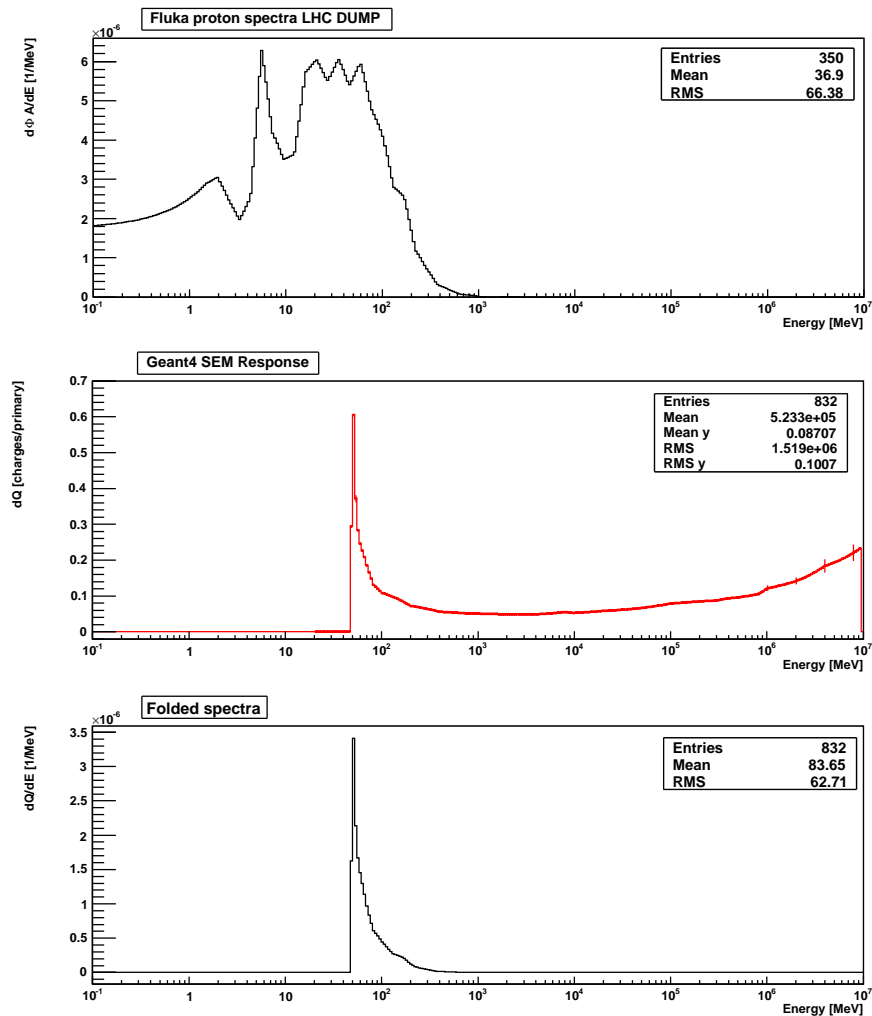


Figure 4.14: LHC Dump monitor signal simulations, Top: Total fluence spectra at the monitor 1 of the dump, Middle: Response spectra of the SEM for primary protons, Bottom: SEM signal spectra obtained by multiplying the Top and the Middle spectra.

and reported in [19]. The track length (dL) inside an empty cylindrical volume (dV) (with similar dimensions like the SEM) of the main particle types was scored in the locations of the SEM detectors and recorded in a text file, which was then used by the author to estimate the corresponding SEM signal. The histogram with the particle fluence was folded with the SEM response, which was simulated for the different particle types as described in the previous section. The example (for protons hitting the SEM number 1) of the fluence histogram, the corresponding response curve and the combined histogram is presented on Fig. 4.14. The resulting charge is obtained by integrating the combined histogram.

The integrated track length obtained from Fluka was converted into fluence using

the known scoring volume but had to be multiplied by the expected active surface  $A$  of the SEM in order to match the unit of the response curves which is given in units of charges produced per primary particle. The total number of charges passing by the sensitive part of the detector fluence histogram ( $dN/dE$ ) is then defined as follows

$$\frac{dN}{dE} = A \frac{d\Phi}{dE} = A \frac{\sum dL}{dV dE} \quad (4.5)$$

where  $\Phi$  is the standard fluence expressed as the number of particles per unit surface. When the two histograms are folded together (multiplied bin by bin), the resulting histogram is

$$\frac{dN}{dE} \cdot \frac{dQ}{e dN} = \frac{dQ}{e dE} \quad (4.6)$$

In order to get the expected charge  $Q_{sim}$  for the given particle type, the integration has to be done in the following way

$$Q_{sim} = e \int \frac{dQ}{e dE} dE \quad (4.7)$$

The simulated signal of the SEM is dominated by the contribution from gammas followed by electrons and positrons. The maximum simulated dose for the ultimate beam was obtained for the SEM number 5 behind the dump core, where 77.4 kGy/dump are expected. This means in terms of charge 59  $\mu\text{C}$  which will be produced by the SEM during the duration of the dump  $t_{dump}$  of about 89  $\mu\text{s}$  (one LHC revolution). The results of the folding of the Fluka fluence spectra and the GEANT4 response curves is summarized in the Table 4.1.

SEM number	Simulated dose
1	146 $\pm$ 16 Gray
2	2.42 $\pm$ 0.27 kGray
3	2.75 $\pm$ 0.30 kGray
4	1.67 $\pm$ 0.18 kGray
5	70.8 $\pm$ 7.8 kGray
6	25.4 $\pm$ 2.8 kGray
7	13.9 $\pm$ 1.5 kGray

Table 4.1: Estimation of the SEM signal in the LHC dump region produced by folding the Fluka simulation results with the GEANT4 response curves.

The peak calculated charge is apparently too high for the CFC electronics and would cause saturation, as the maximum allowed continuous (pulse duration  $\geq 40 \mu\text{s}$ ) current is 1 mA, which would result in a charge of 89 nC in 89  $\mu\text{s}$ . For this reason,

each of the SEM signal cables will be equipped with a shaping filter to lower the peak current by extending the signal duration. The signal of the chamber will first charge a large capacitor, which will then slowly discharge through a resistance to the CFC electronics. The maximum capacity for the chosen filter integration type is limited to  $1 \mu F$ . The filter will transform the original square pulse into an exponential decay with the time constant calculated as

$$\tau = RC$$

Assuming the integral of the signal remains unchanged, the peak current will scale with the ratio

$$\tau/t_{dump}$$

The maximum possible number of current to frequency converter counts in  $40 \mu s$  is 256, but the expected 59  $\mu C$  would theoretically produce 295500 counts in  $89 \mu s$  or 133000 counts in the first  $40 \mu s$ , which is about 519 times 256 counts. The signal has to be therefore slowed down at least 519 times, which translates to  $\tau = 46 ms$ . By applying a safety factor of 2, the resulting filter resistance is  $100 k\Omega$ .

The peak voltage on the filter capacitor should be

$$V_{peak} = Q/C = 59 \mu C / 1 \mu F = 59 V$$

which is conform with the 100 V rating of the capacitor.

#### 4.4 Simulation of the fixed target experiment for production testing and absolute calibration

The complete production of the SEM detectors was tested in a dedicated fixed target experiment located on the secondary beam line H4 in the CERN North Experimental Area. The experiment is described with more details in the Section 6.8 of this work. This type of experiment reproduces very well the mixed radiation field conditions expected in the LHC collimation areas, because the detectors are placed in a hadronic shower created by high energy protons.

The geometry of the experimental setup was partially reproduced in GEANT4 as presented on the Fig. 4.15. The 20 cm long copper cylinder was added to the model, otherwise the geometry remained the same as for the simulation of the sensitivity curves. The cut-off value in the target was set to 10 mm to keep the CPU time per primary reasonable. The last 10 mm part of the target facing the detectors had a smaller cut-off value of  $10 \mu m$  to allow the production of low energy secondaries, which could enter the SEM.

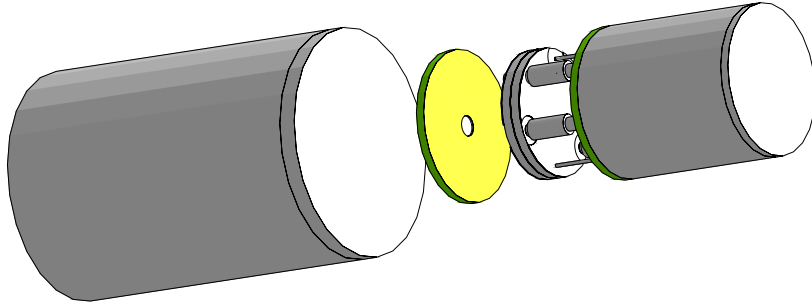


Figure 4.15: Experimental setup of the SEM and the Cu target implemented in GEANT4. The steel cylinder covering the vacuum part is not drawn.

The detectors were placed in a wooden<sup>1</sup> box (low density material with low impact on the radiation field) and placed on a movable table, which was not included in the model. Due to the fixation of the target, thickness of the wooden wall and the geometry of the table, the space between the edge of the target and the bottom cover of the SEM was 8 cm. The parameters of the Gaussian proton beam were set to 5 mm for the vertical  $\sigma$  and 3 cm for the horizontal  $\sigma$  according to the measurements performed with a Polaroid film fixed on the target during the alignment procedure. It was found, that the simulation result does not depend (within the statistical error) on the beam size if it is kept in the order of few cm.

#### 4.4.1 Absolute calibration of the SEM

The SEM beam loss monitor will be used in the LHC together with the ionisation chambers (IC) mainly to increase the dynamic range of the BLM system. In order to allow such combination, the absolute calibration of the SEM preferably in a mixed radiation field has to be made. The calibration could be performed relatively to the IC, because it's absolute calibration is known, but both detectors would have to “see” exactly the same radiation field, which is very difficult due to their different dimensions.

The aim of the calibration is to find a single value characterizing the response of the SEM to a mixed radiation field. The preferred unit is [C/Gray], which relates the charge produced by the detector to the energy deposited in a unit mass.

The response of the ionisation chamber [26] was measured in various beams and

---

<sup>1</sup>It is normally not advised to use any wooden materials in the radiation areas, as contaminated samples are impossible to be cleaned.

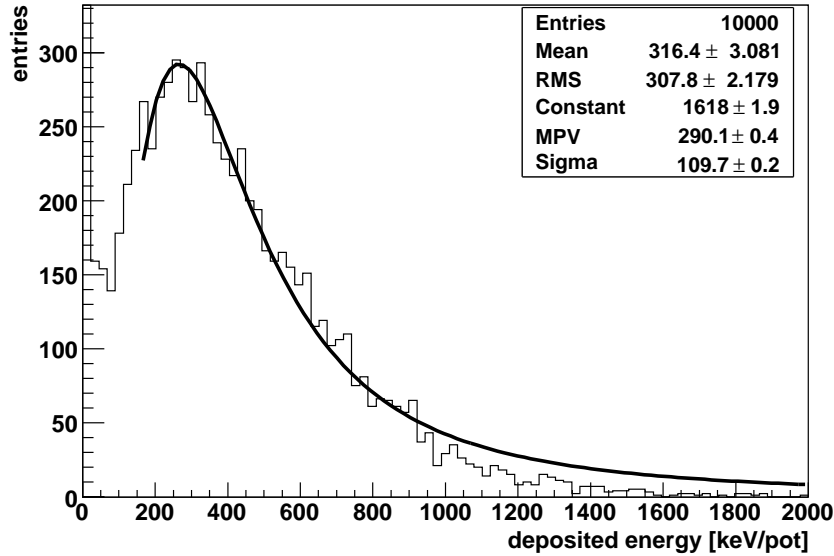


Figure 4.16: Simulated energy spectra of an air filled SEM in the H4 target experiment using  $10^4$  protons hitting the target at 300 GeV fitted with a Landau function.

also simulated in GEANT4. The gas in the IC serves as the active medium and each particle produces a given number of electron-ion pairs per unit path length. When the charge pairs are produced, they can be characterized by the so-called “W factor”, which is the average energy lost from the projectile per produced electron-ion pair. The W factor is very well known and can be found in the ICRU tables[78]. The beauty of the factor lies in its very low dependence on energy of the projectile, so it is a very good measure of the deposited energy in the gas. This energy can be easily transformed into dose ( $Gray \equiv J/kg$ ) by dividing it with the mass of the gas inside the sensitive region.

For the SEM detector, there is no similar value like the W-factor reliably estimating the energy deposition. The SEM was therefore calibrated against the detector with the same dimensions but filled by air. An air filled SEM was placed behind the target in the H4 experiment and measured together with other monitors.

The air filled SEM was also implemented in GEANT4. The energy deposition in the gas at 1 bar between the electrodes was recorded. The cut-off in the air was set to  $10 \mu m$  as suggested by [26]. The parameters of the model were otherwise the same as for the standard H4 simulation. For each proton incident on the target (pot), the energy deposited in the gas is saved. In total 10000 protons are simulated.

The resulting energy spectrum histogram is presented on the Fig. 4.16. The histogram is fitted with a Landau function[73] characteristic for the energy deposition in thin absorbers. The fit is not representing very well the high energy tail neither the low

energy part of the data with large number of events with small energy deposition. This is caused by the mixed radiation field, where different particle types are present with a wide energy ranges. When a similar simulation is performed for a mono-energetic beam of i.e. muons, the Landau function corresponds very well to the data, as it can be seen on the Fig. 4.17. The value important for the calibration is nevertheless the mean value of the deposited energy, as the measurements are always done by integrating the produced charges.

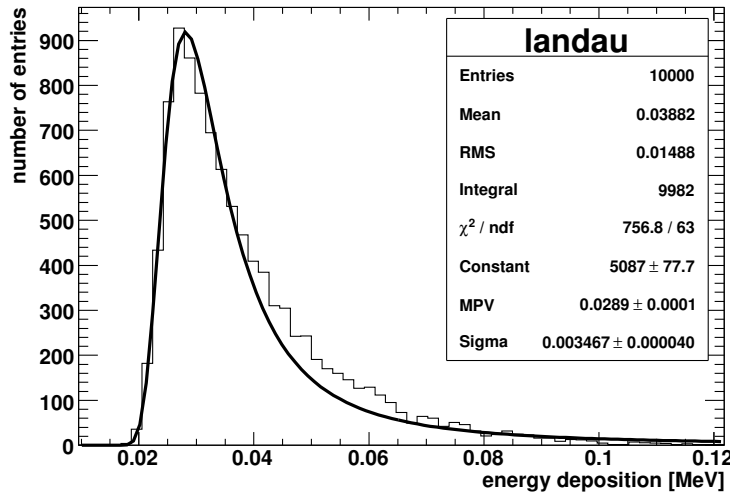


Figure 4.17: Landau distribution. The deposited energy in the SPS ionisation beam loss monitor for a 1 GeV  $\mu^+$  is fitted with the Landau function [26].

The results of both simulations normalized to one primary proton, the standard SEM and the SEM filled by air, are presented in the Table 4.2. The parameters necessary for the calculation of the dose deposition in the SEM are included as well. The W factor for dry air was taken from [78] and the corresponding uncertainty was increased to 1% due to the possible influence of humidity. The uncertainty of the sensitive volume was estimated to 10% due to the complicated geometry and possible edge effects. The simulated value of  $E_{dep}$  was taken as the mean value from the Fig. 4.16.

The energy deposition  $E_{depM}$  in the air filled SEM was calculated from the measured number of produced electron-ion pairs simply by multiplying with the  $W_{air}$  factor. The difference between the simulated and measured energy deposition is very low (3.9%), so the simulated value can be safely used for the calibration. The simulated dose deposited in the gas can be calculated as

$$D_{SEMair} = \frac{E_{dep} e}{m_{air}} = \frac{E_{dep} e}{\rho_{air} V_{gap}} [Gray/N_{pot}] \quad (4.8)$$

where  $e$  is the elementary charge and  $m_{air}$  is the mass of air in the sensitive volume.

#### 4.4. SIMULATION OF THE FIXED TARGET EXPERIMENT FOR PRODUCTION TESTING AND

Variable	Quantity	Description
$E_{dep}$	$316.4 \pm 3.1 \text{ keV}/N_{pot}$	energy deposited in air filled SEM - simulated
$Q_M$	$8984 \pm 28 \text{ 1}/N_{pot}$	charge pairs produced in air filled SEM - measured
$E_{depM}$	$304.1 \pm 3.2 \text{ keV}/N_{pot}$	energy deposited in air filled SEM - calculated from $Q_M$
$S_{SEM}$	$3.95 \pm 0.17 \text{ e}^-/N_{pot}$	response of SEM
$V_{gap}$	$50.8 \pm 5.1 \text{ cm}^3$	volume of the sensitive region
$\rho_{air}$	$1.205 \text{ mg}/\text{cm}^3$	density of air at 1 bar
$W_{air}$	$33.85 \pm 0.34 \text{ eV}$	W factor for dry air

Table 4.2: Results of the Geant4 simulations for the SEM and air filled SEM placed behind the copper target and parameters for the calibration of the SEM.  $N_{pot}$  stands for “proton on target”.

The dose calibration factor  $C_{SEM}$  of the SEM is then calculated by relating the dose deposited in the air filled SEM to the charge produced by the standard SEM under the same irradiation conditions.

$$C_{SEM} = \frac{D_{SEMair}}{S_{SEM} e} = \frac{E_{dep}}{\rho_{air} V_{gap}} \frac{1}{S_{SEM}} [\text{Gray}/\text{C}] \quad (4.9)$$

When the values from the Table 4.2 are inserted to the equation above, the following number is obtained.

$$C_{SEM} = (764 \pm 84) \text{ pC}/\text{Gray}$$

The calibration uncertainty obtained by summing the squares of the relative errors, is dominated by the uncertainty of the sensitive volume estimation.



## Chapter 5

# Design and Production of the SEM

The SEM monitor requires for its specified functioning a very high vacuum to keep the ionisation signal level safely below the secondary electron emission. All the materials were chosen according to the UHV standards, as the outgassing needs to be strictly minimized for being able to achieve the lifetime of 20 years in a very high radiation environments.

The basic geometry of the detector is derived from the LHC Ionisation Chamber (IC) BLM. The vacuum compartment of the SEM is enclosed in a  $\sim 100$  mm long cylindrical tube with a 2 mm thick wall. The cylinder is closed on each side by a welded 5 mm thick covers. The top cover houses a 120 mm long copper tube (used for pumping during the production) and two signal feedthroughs with copper wires and ceramic insulation. Additional active pumping getter was added inside the chamber to absorb gases released during the lifetime of the SEM from the internal components. The copper tube is hermetically sealed-off at the end of the production cycle, when the required vacuum is reached. The sensitive part of the detector is composed of three parallel plate electrodes with the bias voltage connected to the two outer ones and the inner electrodes is connected to the front end electronics. The insulation between the biased parts, the signal electrode and the grounded walls is ensured by the ceramic electrode holders and the feedthroughs. Additional contact insulation was applied on the external part of the signal feedthrough.

The electrical connections are placed in the cylindrical compartment around the copper tube. One BNC signal connector and two high voltage (HV) connectors are fixed to the 5 mm cover plate. The signal connector wire is shielded from the high voltage wires by an additional grounded plate. Most of the SEM detectors do not contain any additional electrical components, but some special ones contain also a large HV capacitor and a resistor placed inside the electric box.

During the design and production, an effort was made in order to assure the cleanliness of all the surfaces and the minimization of possible unpumped gas volumes or leaks. All the steel components (without threads) were vacuum fired at  $950^{\circ}\text{C}$  and the Ti electrodes at  $750^{\circ}\text{C}$  to outgas the  $\text{H}_2$  dissolved in the bulk during the production of the metal. A similar procedure was put in place for the electrode holders during the brazing with the ceramics.

A very high sensitivity outgassing test was performed at CERN to estimate the thermal desorption rate of the detector. The results indicated a very slow pumping of the Ti, thus the thermal outgassing could be compensated by this effect. Nevertheless, the radiation induced desorption has a potential to degrade the vacuum considerably, so an additional pumping was needed. A stripe of a high capacity Non Evaporable Getter (NEG) ST707 was therefore inserted in the chamber. The total available surface ( $170\text{ cm}^2$ ) of the NEG has a potential to adsorb the quantity of gas equivalent to 20 mono-layers covering all the detectors' inner surfaces. The NEG has to be activated by heating at the temperature of  $350^{\circ}\text{C}$  for 14 hours, so the pumping cycle of the SEM is extended compared to the IC (see Fig. 5.4). The He leak testing is performed additionally after the activation and the final pressure before the pinch-off is below  $10^{-10}\text{ mbar}$ .

## 5.1 Choice of materials

The SEM detector has to operate in a very high radiation conditions for a considerably long time, while integrating large doses without changing its relative response. It is also required to keep the vacuum inside the closed vessel below the  $10^{-4}\text{ mbar}$  level. The dynamic range requirements impose the use of the detector in the pA range, therefore the leakage currents in the feedthroughs and the electrode holders have to be minimized.

The choice of the materials for the design of the SEM was based on this short list of requirements, which indeed restricts the available options considerably. The materials used for the SEM construction are listed in the Table 5.1.

### 5.1.1 Signal electrode

The electrode material has a direct impact on the detector response and variations of more than a few percents can not be tolerated. The Secondary Emission Yield (SEY) of each material depends on its surface properties. Because metals are normally covered by a thin oxide layer if once exposed to air, its properties are the most relevant for the SEY stability. The foils of pure metals without surface contamination could be theoretically used but the handling of such a foils during production would be extremely



Figure 5.1: Assembly of the interior of the SEM detector without the NEG pump.

difficult. Aluminium is one of the most common metals in the UHV applications due to its very low thermal degassing and easy machining. The electrodes in the LHC ionisation chambers are made of Al and were considered also for the SEM.

A serious degradation [29], [31] of the Al SEY was observed in various large current high energy accelerators. When an Aluminium foil covered by  $Al_2O_3$  is exposed to the integrated flux of  $10^{20}$  *protons/cm<sup>2</sup>*, its SEY drops by almost 40% as can be seen on the Fig. 5.2. The usable range of the Al foil is extended if coated by a thin layer of gold, which doesn't have a surface oxide, but the best material seems to be the Titanium covered by  $TiO_2$ . It shows an increase in the response in the order of 15% after the passage of  $10^{19}$  *protons/cm<sup>2</sup>*, but the SEY tends to return to the previous values for higher doses.

The degradation could be explained by the progressive removal of the surface oxide layer causing the decrease of the SEY, which is approaching the level expected for a clean metal. The difference between the SEY of Al and  $Al_2O_3$  predicted by the Stern-glass theory is effectively 40%, but a drop of 31% should normally be expected also for the  $TiO_2$ . As this is not the case, we assume that the  $TiO_2$  is much harder to remove than the  $Al_2O_3$ . Unfortunately, it was not possible to study the foils from [29]

SEM number	material type	remark
SS 304L	stainless steel	low outgassing
SS 316L	stainless steel	low outgassing
$Al_2O_3$	ceramics	zero porosity
Cu	annealed copper	low outgassing
Ti	metal	SEY stability
Kapton	insulator	radiation tolerant
Dilver	metal	for ceramics brazing

Table 5.1: Materials used for the components of the SEM.

without exposing them to air. The Titanium with 99.6% purity was finally selected as the electrode material for the SEM because of the proven SEY stability.

The shape of the SEM electrodes is for cost reasons kept the same as for the Ionisation Chambers (IC), so the same production tool could be used. In order to reduce the risk of breaking the dye, which was designed for the 0.5 mm thick Aluminium plates by using the almost twice harder Titanium, the thickness of the Ti electrodes was therefore reduced to 0.25 mm. The thickness of the signal electrode does not influence the SEY, only the emission probability of delta electrons at high energies decreases with smaller thickness (see Fig. 4.8). Titanium was also chosen as the material for the bias electrodes for its more favorable dynamic outgassing properties than Aluminium as already mentioned in the previous section.

### 5.1.2 Electrode holders

The design of the first SEM prototypes was derived directly from the IC, so all the electrodes were supported by one single ceramic disc (Fig. 6.1) made from a very high resistivity alumina ceramics (more than 97% of  $Al_2O_3$ ) by the SCT company [49]. The ceramics has a zero porosity, so it is suitable for the UHV applications. For the IC, the leakage current is in the order of 1 pA when the 1.5 kV bias voltage is switched on, which would be acceptable for the SEM as well. However, the tests performed under continuous proton beam irradiation revealed important transient “memory” effects in the SEM response every time the bias voltage was changed not depending on the time evolved from the change (Fig. 6.5). The effect was attributed to the charging of the ceramics surface and disturbing the electric field of the chamber. The phenomenon is usually called the “Schalt-effect” [51] and is related to the secondary emission from the insulating materials.

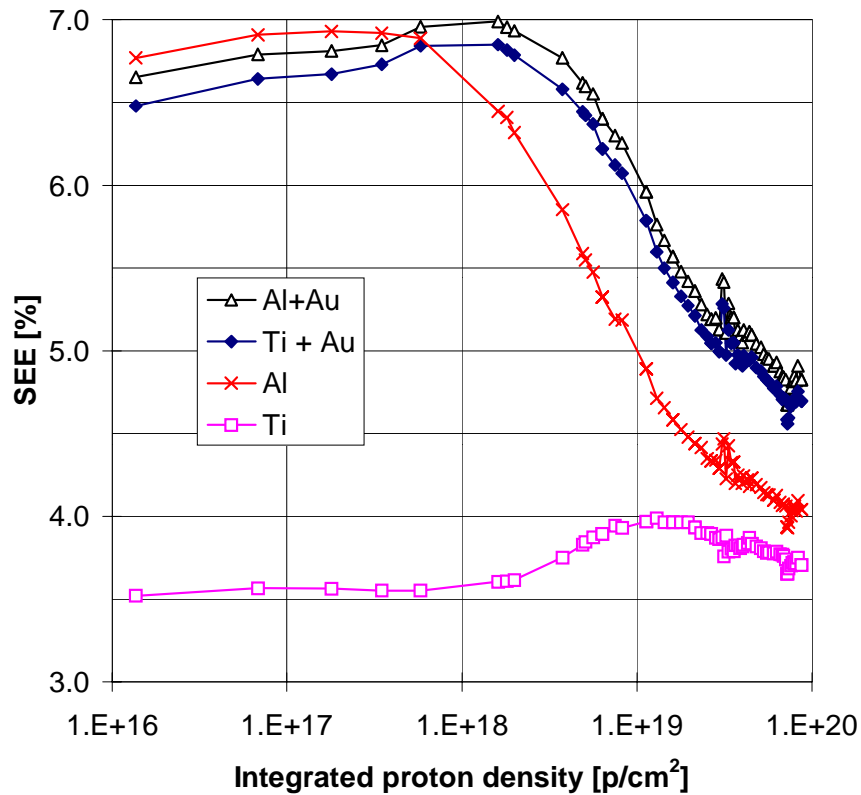


Figure 5.2: Change in SEE of Gold coated Aluminium and Titanium foils, comparison with oxidized Aluminium and Titanium foils [29].

The memory effect was successfully suppressed by a grounded shielding plate placed on the ceramic disk, but such a solution is not very favorable from the vacuum point of view. Un-pumped gas pockets could be produced in some cases, so the design of the electrodes support was changed. The guard-ring design (p.136 of [36]) was adopted, as it lowers the requirements for the resistivity of the insulator and a much smaller amount of the ceramics can be used. In the guard-ring system, a grounded electrode (or ring) is placed around the signal electrode to avoid any direct path for the leakage currents between the signal and the bias electrode. The guard electrode is maintained in the ideal case at the potential of the signal electrode, so no leakage currents should flow between them.

In our case, the whole steel cover plate is connected to the ground and serves therefore as the guard electrode. The insulated electrode holders are welded to the cover plate on one end and screwed to the bias or signal electrode on the other end. Both sides of the holder are equipped with holes allowing the pumping of the otherwise closed volumes. The top part houses an additional hole, which is used during the assembly

to hold the piece while tightening the nuts. The material of the insulator ceramics is of the same type like the disk of the IC. The ceramics has a form of a tube to assure better pumping and minimize the cross section of the insulator and consequently the resistance. The metallic parts are made from the Dilver P1 (iron-nickel-cobalt 29-18 alloy) material which is very suitable for the brazing with the ceramics as it has the same coefficient of thermal expansion (CTE) as the ceramics at room temperature and lower CTE at the brazing temperatures, so a good contact between the materials is assured. A short plateau of about two hours was introduced to the high temperature part of the brazing cycle to outgas the hydrogen dissolved in the metal. The brazing was performed in vacuum to allow the outgassing. The bottom part of the holder was made long enough to minimize the risk of damaging the brazing during the welding.

The copper feedthroughs were used as the additional supports of the signal and bias electrodes, so that only four ceramic holders are needed per chamber. The additional holder is made of stainless steel 316L and contains two pumping holes.

### 5.1.3 Stainless steel components

The most common austenitic stainless steel materials suitable for the UHV applications were chosen for the design of the SEM. The AISI 316L and 304L alloys have a very low carbon content ( $< 0.03\%$ ) to assure the corrosion resistance even after the welding or vacuum firing. The materials are non magnetic due to their austenitic structure and therefore will not disturb the operation of the detector. The 304L is composed of Fe, Cr(18%), Ni(11%), and C(0.03%). The 316L steel has an improved corrosion resistance and is composed of Fe, Cr(18%), Ni(14%), Mo(3%) and C(0.03%). The outgassing rates of these steels are very low [52] if cleaned properly and the permeation of gases through the bulk is generally inhibited as well [53].

During the fabrication process of the steel, the atmospheric hydrogen dissolves in the bulk of the material and as it diffuses towards the surface, it outgasses into the vacuum. Such a behavior is minimized by heating the steel to  $950^\circ\text{C}$  while keeping it in a high vacuum for 2 hours. At high temperatures, the diffusion coefficient of the  $H_2$  increases (see Fig. 5.3) and if the material thickness is higher than diffusion length, the concentration of  $H_2$  in the bulk is determined only by the pressure in the furnace through the Sieverts' law [54]:

$$c \left[ \frac{\text{Torrr } l(H_2)}{\text{cm}^3} \right] = 8.21 \cdot 10^{-2} \sqrt{P[\text{Torrr}] \cdot e^{-\frac{2650}{1.99 \cdot T[\text{K}]}}} \quad (5.1)$$

The temperature during the firing must remain below  $1050^\circ\text{C}$ , because the grain size of the metal starts to grow considerably. On the other hand, when the temperature

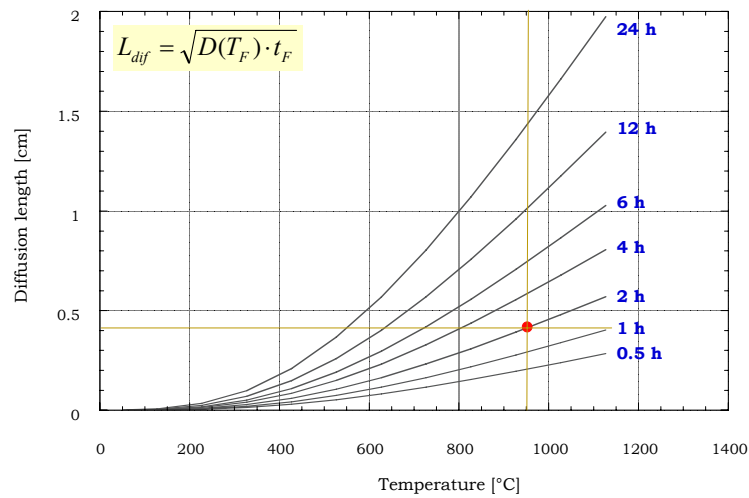


Figure 5.3: Diffusion length of  $H_2$  in stainless steel as function of temperature and the firing duration [55].

is lower than  $900^\circ C$ , the carbides can precipitate on the grain boundaries and induce a sensitivity to the corrosion and a sigma phase transformation making the metal brittle can occur as well.

## 5.2 Vacuum

### 5.2.1 Getter Pump

A surface may provide a useful pumping action when able to retain adsorbed gas molecules for the duration of a given experiment. To fulfill this condition at room temperature, strong binding forces, as those resulting from chemical reactions, are required. Materials able to react with gases to form stable chemical compounds are called getters [57].

The most widely used evaporable getter in the vacuum instrumentation is the Titanium sublimation pump. Its pumping capacity is defined only by the quantity of Ti available in the filament, which can be released by repeated high temperature sublimations. Unfortunately, such a system can not be used inside the SEM detector, because the sublimated Ti could deposit on the ceramic insulating components and produce undesired leakage currents.

The Non Evaporable Getters (NEG) on the other hand do not have to be periodically heated and can be activated only once. During the activation heating, the oxide layers from the surface dissolve in the bulk of the material and expose a clean highly porous surface ready to adsorb molecules on its surface and absorb hydrogen in the bulk.

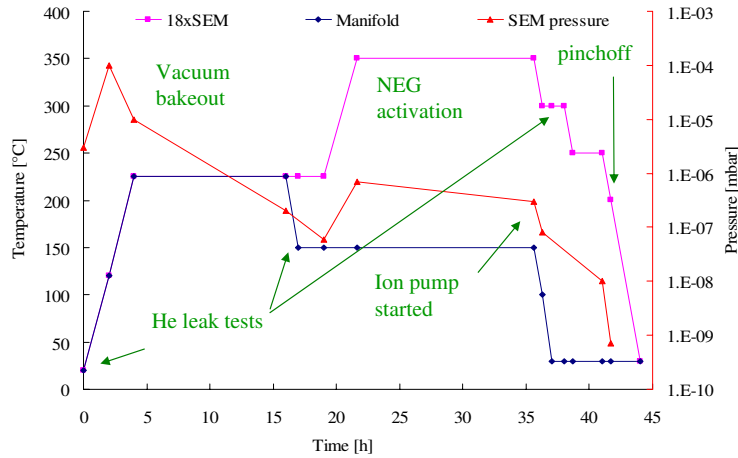


Figure 5.4: Vacuum bakeout and NEG activation cycle during the SEM production in IHEP Protvino. The temperature of the 18 detectors processed in parallel is in pink.

The NEG type St707[56] chosen for the SEM design combines a very high pumping capacity and a moderate activation temperature. It is a powder composed of 70% Zr, 24.6% V and 5.4% Fe (weight fraction) pressed on two sides of a 3 cm wide Kapton stripe. The NEG has to be activated at  $400^{\circ}\text{C}$  for about 45 min or at  $350^{\circ}\text{C}$  for 14 h as reported in [16]. The total pumping capacity [16] of the NEG for the most important gases in UHV stainless steel environment, if the pumping speed is irrelevant like in our case, is 0.5 Torr l/m for CO or  $\text{CO}_2$  and 200 Torr l/m for  $\text{H}_2$  (linear weight of 10 g/m of the NEG strip assumed). The major inconvenience of the getter pumps is that they can not pump methane and noble gases, because no chemical bonds can be formed between these gases and the getter. Nevertheless, recent measurements indicated, that most of the  $\text{CH}_4$  detected in the UHV systems is not produced by degassing of the inner surfaces. It is very likely that methane is not outgassed from clean stainless steel; the methane contamination is all released by the QMA (quadrupole mass analyzer)[47].

### 5.2.2 Thermal and radiation induced outgassing

In order to know the length of the NEG stripe needed for keeping the vacuum at reasonable levels for the 20 years lifetime of the SEM, the quantity of gases that could be desorbed has to be estimated. The gases can originate from the thermally induced outgassing process or from the radiation induced outgassing.

The rate of the thermal outgassing of a cleaned vacuum fired and in-situ baked-out stainless steel surface is in the order of  $2 \cdot 10^{-13} \text{ Torr l/s/cm}^2$ [60], where the dominant element is hydrogen. If the total internal surface (see Table 5.2) of the SEM was assumed to be steel, the outgassing rate would be about  $1.5 \cdot 10^{-10} \text{ Torr l/s}$ . If the

rate now remains constant, after 20 years of operation the accumulated quantity of gas would be 0.1 Torr l. As the internal volume of the SEM is 0.58 l, the final detector pressure would be 0.17 Torr (0.22 mbar), which is much above the specified  $10^{-4}$  mbar. This estimation is very pessimistic, because it assumes a constant outgassing for the whole lifetime. Normally, the outgassing slows down as the concentration of the hydrogen in the steel lowers.

variable	quantity	description
$A_{SS}$	502 cm <sup>2</sup>	steel walls area
$A_{Ti}$	88 cm <sup>2</sup>	Single electrode area
$V_{SEM}$	583 cm <sup>3</sup>	Inner SEM volume

Table 5.2: SEM dimensions relevant for the outgassing estimations.

In a highly radioactive environment, the major contribution to the outgassing is expected to come from the energy deposition by the incoming particles and the subsequent release of molecules from the inner surfaces. It is clear from very rough estimations for the LHC collimation areas, that the dose received by the SEMs during the 20 years of operation assuming 200 days per year of nominal beam will reach levels of the order of  $10^{18}..10^{19}$  MIP/cm<sup>2</sup> (minimum ionising particles). This number has to be compared for example with the well documented electron stimulated gas desorption of Copper[46]. When the Cu surface is irradiated with  $10^{20}$  e<sup>-</sup>/cm<sup>2</sup>, the desorption yield for H<sub>2</sub> and CO decreases by almost 3 orders of magnitude. Apparently, there is an upper limit to the amount of gas releasable from a unit surface of a metal given by the treatment of the material and should be considered for the dimensioning of the NEG pump of the SEM.

The estimation of the total amount of CO on the surface of the steel can be estimated by using the results of the Cu desorption, which has the outgassing properties similar to steel. The total amount of released CO during the experiment was  $10^{16}$  molecules/cm<sup>2</sup>, which gives 0.15 Torr l if the total inner surface of the SEM is considered at 20 °C. A very similar number can be obtained by calculating the absolute oxygen content in a few nm thick Cr<sub>2</sub>O<sub>3</sub> surface layer (see i.e. [63]).

The observed[64] initial outgassing rate of H<sub>2</sub> from stainless steel 316LN was three times higher than that of CO, so the previous result can be just scaled by this number giving 0.45 Torr l of H<sub>2</sub>. It can be seen from the Tab. 5.3, that the required length of the NEG stripe is determined by the CO content as the H<sub>2</sub> capacity of the NEG is very high. Each produced SEM finally contains a NEG stripe of 32 cm held by two steel wires welded to the bottom cover.

Gas Type	NEG capacity	Desorbed quantity in 20y	required length of NEG
CO/CO2	0.5 [Torr l/m]	0.15 [Torr l]	30 [cm]
H2	200 [Torr l/m]	0.45 [Torr l]	0.22 [cm]

Table 5.3: The length of the NEG St707 stripe required for pumping all the releasable gases from the inner surfaces of the SEM.

### 5.2.3 Test production at CERN

The outgassing estimations for the dimensioning of the NEG stripe were very approximate and a validation measurements had to be performed with the SEM produced from the final components. The isolation pressure rise technique[47] was used for estimating the outgassing of the SEM after two different bakeout cycles without the NEG inside.

The SEM was first baked out at  $225^{\circ}C$  to be sure, that no activation of the Ti electrodes could happen and a “true” outgassing rate of the chamber could be measured [61]. The resulting outgassing rate was  $5 \cdot 10^{-11} \text{ Torr l/s}$ . During the second measurement, the SEM was heated up to the  $350^{\circ}C$  like during the activation of the NEG. In this case, a very slight pumping of the Hydrogen was observed. The pumping was apparently due to the partial activation of the Ti (a small fraction of the Oxygen from the surface TiO2 dissolved in the Ti bulk and allowed an additional sorption of gases) and was estimated to be about  $10^{-6} \text{ l/s}$ . This result indicates, that if there was no NEG in the SEM and the pumping speed of the Ti remained the same as measured, the pressure inside the SEM would stabilize at  $5 \cdot 10^{-5} \text{ Torr}$ , which is just below the required maximum pressure.

## 5.3 Serial production at IHEP Protvino

The serial production of the SEM detectors for the LHC was assured by the Russian Institute of High Energy Physics in Protvino. All the detector components were supplied by CERN and transported to IHEP by lorries. The stainless steel components and the Ti electrodes were cleaned and vacuum fired at CERN before the shipping. These components were wrapped in Aluminium foil and protected by a Nitrogen atmosphere.

All components for the production of one batch (with the exception of ceramics components) are cleaned in IHEP shortly before assembly, following the CERN standard for UHV requirements [62]. The stainless steel components are cleaned in an UHV ultrasonic bath with NGL<sup>1</sup> (20 g/l) in distilled water at  $65^{\circ}C$  during 30 minutes. After that, they are rinsed in distilled water at room temperature and again in an UHV

<sup>1</sup>NGL 17.40 SP ALU, NGL Cleaning Technology S.A. Nyon, Switzerland

ultrasonic bath during 5 minutes. The last step of the cleaning procedure is baking at  $150^{\circ}\text{C}$  in air. After the cleaning, all components are transferred to the clean room for assembly in a closed packing.



Figure 5.5: Vacuum production stand in IHEP Protvino with 18 SEMs equipped by temperature probes before pumping.

### 5.3.1 Vacuum stand

The vacuum production stand (Fig. 5.6) was designed in collaboration with CERN and built in IHEP. The ultra high vacuum pumping part consists of the pre-vacuum pump, one turbo-molecular pump - TMP56 (pumping speed of 56 l/s), and an ion molecular pump (pumping speed of 100 l/s), which can work only in the high vacuum conditions. Two penning vacuum gauges are of the type PKR261 (range of operation from  $5 \cdot 10^{-9}$  to 1000 mbar) and three piezzo gauges of the type APR262 (range of operation from 0.2 to 2200 mbar). The Prisma QMS 200F2 quadrupole mass spectrometer is used for detecting the composition of the gases inside the system. The pumping system is equipped with two branches called manifolds with 18 connection ports with individual valves for the IC or the SEM detectors each.

During the SEM production, only one manifold was used in order to reach a better vacuum conditions, as only a single turbo molecular pump was employed. The performance of the stand had to be improved, because the requirements for the SEM production are more strict than for the IC. Several piezoelectric pressure gauges were removed from the system, as they could not be baked out at the nominal temperature and consequently the water content in the system was too high. The Viton (plastic)

gasket of the turbo pump had to be replaced by the Helicoflex (metallic) gasket as the former material is not conform with the UHV requirements due to its strong outgassing. Additionally, a relatively high hydrocarbon content was detected during the production of the ICs, which was traced to the sub optimum working mode of the turbo pump during the pumping of air or  $N_2$  after the filling at atmospheric pressure. Consequently, a variable leak valve (V7 on Fig. 5.6) was introduced to keep the high rotation speed of the turbo pump constantly.

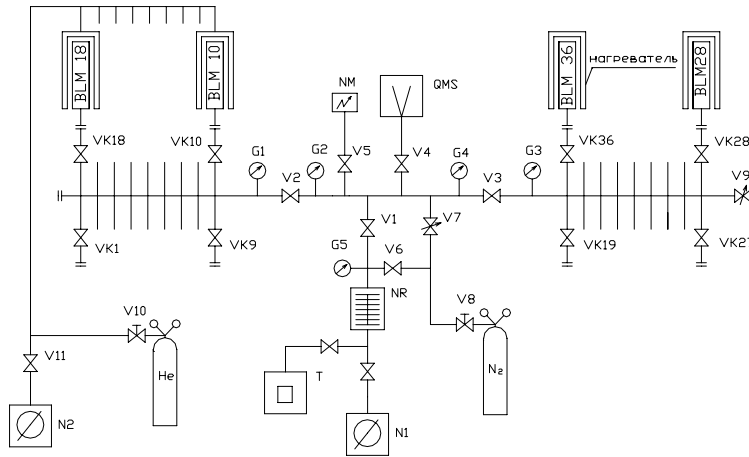


Figure 5.6: Schematic of the vacuum production stand in IHEP Protvino. The right branch starting by the valve V3 is used only for the IC production. symbols used: G-pressure gauge; V-valve; T-He leak detector; N-high pressure rotary pump; QMS-quadrupole mass spectrometer; NM-Ion pump; NR-turbomolecular pump. V3 and V1 are permanently closed.

### 5.3.2 Quality control

The welds have been executed by TIG (tungsten inert gas) arc welding under argon shielding without a filler material and with 100% penetration of the welds. Several different tests were performed at IHEP before, during and after the production to verify the quality of chambers.

The quality of the cleaning processes was regularly checked by cleaning the standardized samples and analyzing their surface contamination at CERN. All the components were visually inspected before the assembly and the leakage currents of the feedthroughs and the electrode holders were tested with a pico-ampere meter. All welds were He leak tested. Before heating, the outgassing of the chambers and the stand was measured to estimate the quality of the component cleaning by using the QMA. The same procedure was repeated after heating. The analysis of the rest gas composition after a bakeout of the stand without the SEMs installed is presented on

the Fig. 5.7. The main pressure contribution comes from hydrogen as in all cleaned vacuum systems. At CERN, a standard UHV system is considered as well baked, when the water peak is 100 times smaller than the  $H_2$  peak [60]. The vacuum stand is slightly below this requirement after 24 h pumping indicating a presence of lower temperature parts, but it was still considered as satisfactory for the SEM production. In any case, water is well pumped by the NEG.

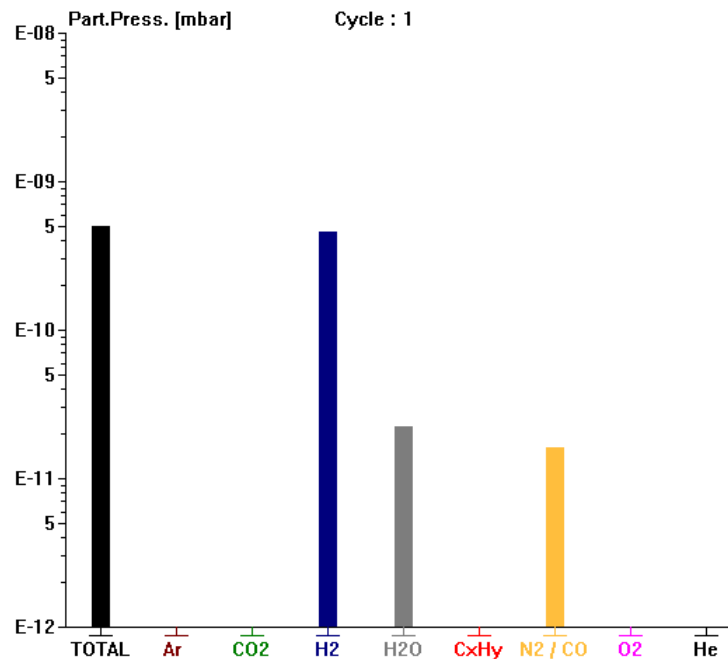


Figure 5.7: Rest gas analysis of the vacuum production stand in IHEP after 24 hour pumping and bakeout at 220 °C.

The Helium leak testing was performed after the initial pumping before the bake-out (see Fig. 5.4), before the activation of the NEG and after the activation during each production cycle. The testing was done by blowing He in the heating containers around the SEMs and detecting the possible leaks by observing the signal of the QMA for He or directly by using the dedicated He leak detector. For tracking purposes, the temperature of each SEM and the vacuum measurements were recorded for each cycle.

The final acceptance tests of the SEMs were performed in a dedicated fixed target experiment in the North experimental area of CERN in November 2007 and June 2008. These measurements are described in the section 6.8.



## Chapter 6

# Test and Calibration Measurements

It is expected that the SEM response is low but linear in very high radiation fluxes. In the development phase, the detectors have to be tested in a well defined radiation field in order to verify the operational parameters and compare the response to the simulations. Preferably, it should be a continuous charged particle beam. Continuous form is preferred, because it enables the use of very high sensitivity femto-amp meters. The charged beams are better than i.e. a neutron field of a reactor, because the response per particle is considerably higher, the flux of the beam can be easily measured and the energy spread is very small. The possibility of frequent access to the irradiation zone is also very important.

On the other hand, the response to very short and intense radiation pulses can be measured directly by an oscilloscope but the setup has to be installed directly inside a synchrotron accelerator area (transfer or dump line). The access conditions are very limited, so this approach can be used only for the calibration purposes.

Several prototype versions of the SEM detector were produced at CERN and tested under different irradiation conditions. The main testing site was the Paul Scherrer Institute in Villigen[15], which has high proton current cyclotron beams and a very user friendly access to the test areas. The detectors were also tested at CERN in the dump line of the PSB (Booster), the transfer line TT20 from SPS to the North area and on the internal dump of the SPS.

The samples of the final production were placed in the LHC test collimation area of the SPS and the muon beam of the COMPASS fixed target experiment. The complete production was tested using a gamma radiation source and a dedicated fixed target experiment, which was built in the H4 line of the SPS North area.

The tested versions of the SEM design are summarized in the following list

- Type C - first prototype directly derived from the IC design with the signal electrode in Ti and 2 Al bias electrodes (Fig. 6.1)
- Type CII - second prototype version derived from the C type with additional grounding plates on the ceramic disk to eliminate the charging of the ceramic surface and 2 Al bias electrodes; vacuum fired steel components (Fig. 6.7(a))
- Type F - prototype with 4 ceramic electrode holders based on the guard ring design with 2 Al bias electrodes; vacuum fired steel components (Fig. 6.7(b))
- Type Fb - prototype subversion with 2 Ti bias electrodes and shorter length to fit in the small space of the TT20 experiment; vacuum fired steel components (Fig. 6.12)

## 6.1 Early stage prototype tests

The first prototypes of the SEM were produced in November 2005 at CERN. The design was directly derived from the LHC IC but containing only 2 aluminium bias and one titanium signal electrode held by a large ceramic disc (Type C version). The assembly without the stainless steel housing or the connector box is shown in the Fig. 6.1. The detectors were tested in the CERN PSB and PSI proton beams in November and December 2005 and the second generation prototypes were produced based on the experience of these measurements.

### 6.1.1 Experimental setup in PSB

The prototype C of the SEM placed on a movable stage in front of the PS Booster (PSB) dump. The chamber was baked out and the pumping was stopped at a pressure of the group of about  $3 \times 10^{-8} mbar$ . The copper pumping tube was closed by a vacuum valve.

The electronic connection box was equipped with the standard low pass filter on the HV side. The signal wire was shielded from the HV connector by a steel half cylinder, but the cover of the box was not installed and the connections were very poorly shielded. The experimental setup will be described in greater detail in the section 6.3.

The beam was aligned to the center of the bottom plate and the current produced by single bunches of 1.4 GeV protons was recorded directly by a Tektronics TDS440A scope with a  $50 \Omega$  termination and a 10x attenuator. The output charge was also integrated by the SPS SEM beam screen electronics later during the same session. It uses a simple charge integrator with an A/D conversion of the resulting capacitor voltage. The measurement uncertainty was estimated to 1% for the low noise SPS electronics

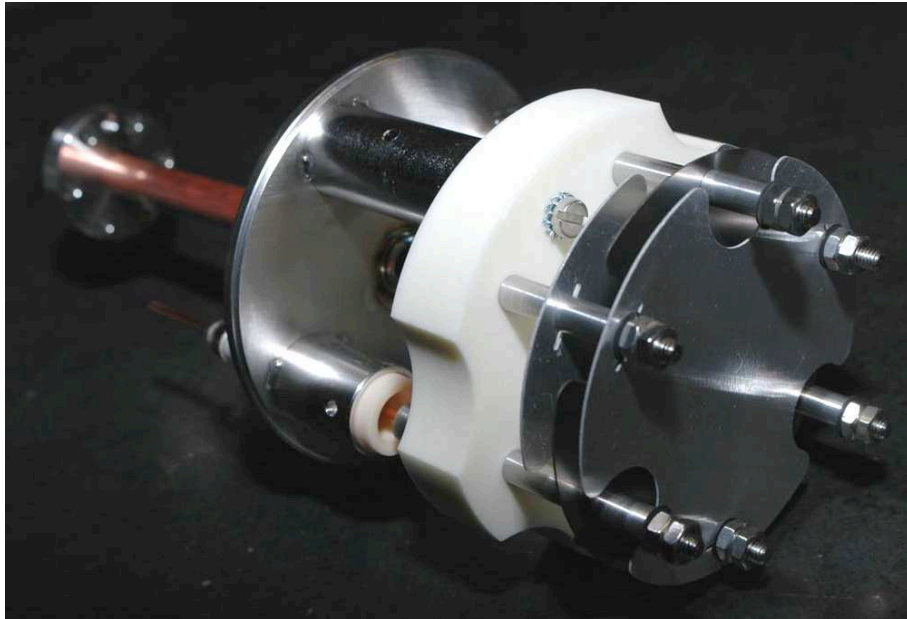


Figure 6.1: First SEM prototype (type C) assembly derived from the Ionisation Chamber design.

and a maximum 5% for the offline integration method of the oscilloscope data (driven by the beam current measurement error). The data of Figure 6.3(a) were obtained by manually changing the bias voltage and integrating the response current offline by a Matlab script. The average bunch intensity during the bias voltage scan was  $2 \times 10^{12}$  protons.

For voltages higher than 50 V, a flat Secondary Emission Yield (SEY) dependence on bias voltage was expected according to the experience from the CERN secondary emission beamline screens[27]. As no saturation is expected for the secondary electron emission effect, the response normalized to the beam intensity should be constant for different bunch currents (see Fig 6.3(b)).

### 6.1.2 Experimental setup in PSI

A very similar prototype was built for the beam tests in the PSI 250 MeV [15] proton beam line. It had a steel half-cylinder shielding between the signal and the bias connectors, but the box was otherwise opened to air. The measurements were performed in November and December 2005. The detector was placed directly in the beam line in front of a temporary beam dump, which stops the protons from entering the Gantry1 medical facility. The beam fluence is measured by a thin ionisation chamber with a 5 % accuracy. The chamber output current was measured by a Keithley electrometer

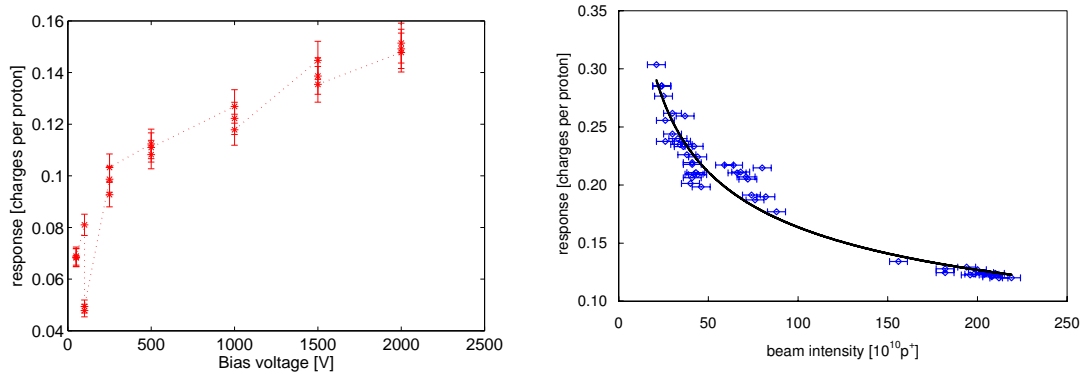
6517A. The SEM prototype was tested with different beam impact angles, positions and bias voltages. The chambers were insulated to avoid ground loops (yellow tape on Figure 6.2).



Figure 6.2: SEM C prototype irradiated transversally in PSI by a 250 MeV proton beam centered to the electrodes.

### 6.1.3 Results and discussion

The resulting shape of the curves on the Figure 6.3 points to an important contribution of the ionisation to the SEE signal.



(a) Normalized response for different bias voltages with  $200 \times 10^{10} p^+ / \text{bunch}$  (b) Normalized response for different bunch intensities for 1000 V bias

Figure 6.3: First prototype tests of type C version in the 1.3 GeV proton beam in the PSB dump line.

The plot 6.3(b) clearly shows saturation caused either by the space charge effect and the volume recombination or saturation due to the lack of neutral atoms because of the low gas pressure. The shape of the plot 6.3(a) indicates a problem with the ionisation in a non-homogeneous electric field or a field with higher electrode separation than

inside the SEM. With voltages of more than 500 V and the separation gap of 0.57 cm, the signal of the parallel plate LHC IC no longer depends on the applied voltage as the collection efficiency is nearly 100%.

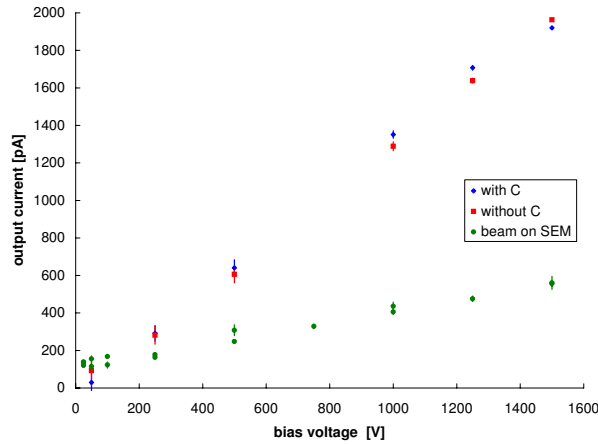


Figure 6.4: SEM C prototype irradiated transversally in PSI by a 250 MeV proton beam. The blue and yellow points are for the beam centered on the connector box (with or without the HV capacitor) and the green on the electrodes.

The signal nonlinearity was clearly traced to the connection box with the vacuum feedthroughs during the tests in the 250 MeV beam. The measured output current was noticeably higher with the proton beam centered on the box than compared to a centered beam to the signal electrode (the copper pipe was oriented vertically). As the box contains a high voltage capacitor, it was disconnected and the detector tested again in the same position. It can be seen on the Fig. 6.4, that there is no influence of the capacitor (red box on Figure 6.2) as it was expected. The excessive output current is therefore caused by the ionisation in the air around the connectors and a drift of charges in the nonlinear electric fields around them.

There was another unexpected effect observed, when the bias voltage of the Type C prototype was changed. After a sufficiently long waiting time when the current produced during the charging or discharging of the HV capacitor decayed below the pA level, the beam was turned on and the response of the SEM recorded. The result is shown on on the top of Fig. 6.5. The effect was not observed anymore, when the acquisition was repeated with the same voltage (bottom plot). This behavior was independent of the beam energy or the chamber position, because the later measurements of the same detector revealed the same effect (see Fig. 6.6).

The charging of the ceramic disk to a certain stable level caused by the secondary emission from the disk itself seems like the most probable cause of the transient signal variation. During the charging, the main bias field of the SEM is disturbed and the

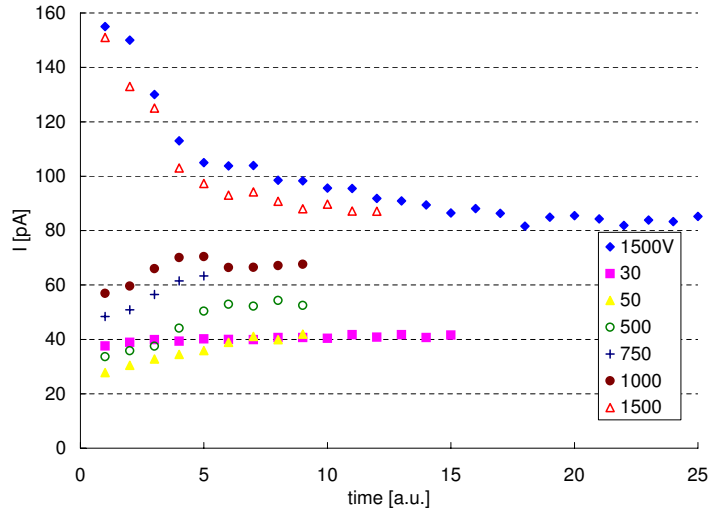


Figure 6.5: Evolution of the signal of the SEM C prototype in a longitudinal position in the 250 MeV  $p^+$  beam after a bias voltage change. Top: acquisition after the voltage change; Bottom: repeated acquisition.

effect disappears, when the potential of the ceramics stabilizes. A second SEM prototype with the ceramic disk was produced containing a grounded plate on the side of the ceramics facing the bias electrodes. No transient effects were observed on that prototype.

## 6.2 Calibration in Cyclotron proton beam at 63 MeV

The second version of the SEM (CII) with the ceramic disk holder and a grounded aluminium plate (Fig.6.7(a)) was tested in the low energy cyclotron beam in PSI. Another SEM (F) prototype (Fig.6.7(b)) based on the guard ring design was tested under the same conditions. All the steel components were vacuum fired to reduce the thermal outgassing like for the final production.

The F type SEM is very similar to the final version, only the electrode holders are slightly different, the thickness of the electrodes is 0.5 instead of 0.25 mm and there is no active pumping NEG stripe. The calibration of the F type can therefore be considered as if the final design was used.

### 6.2.1 Experimental Setup

The chambers were tested in the 62.9 MeV proton Optis line of the PSI cyclotron complex[15]. Protons were entering through the 5 mm thick steel bottom cover of the detector. The output current was measured by the Keithley electrometer 6517A. The

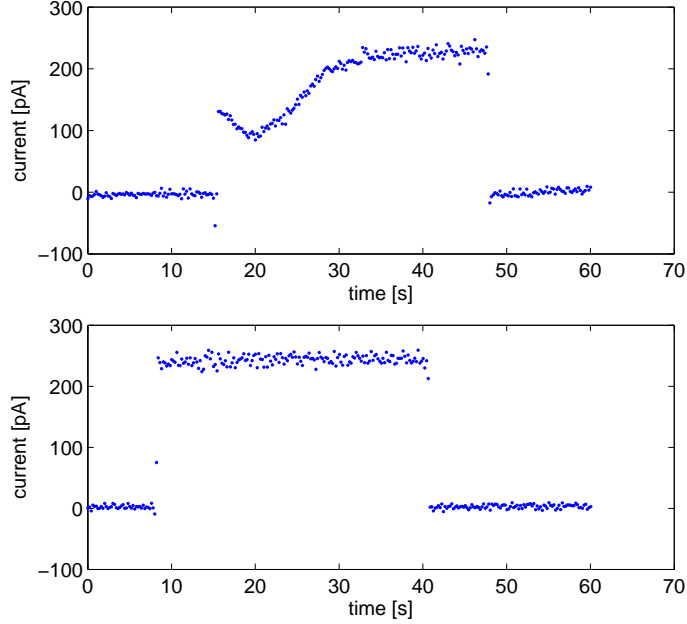


Figure 6.6: Evolution of the signal of the SEM C prototype in a transverse position in the 63 MeV p+ beam after a bias voltage change from 500 to 250 V.

FUG HLC14 high voltage power supply was connected to the bias electrodes. The data acquisition was done with help of a LabView program running on a laptop with a GPIB interface. The power supply was operated by the same program. The beam was operated via a standard PSI interface and was tuned to a maximum available flux of about  $5 \cdot 10^8 p^+ / cm^2 / s$ . The round beam had a 8 cm diameter with a quite uniform intensity distribution up to 7 cm. The data acquisition was always started before the beam run and finished after the end of the run.

The number of impacting protons was calculated by using the active area of the electrodes of  $44.2 cm^2$  and assuming a uniform beam distribution. The value of the output current was obtained by averaging the acquired current sample. Several points after the start and before the end of the beam run were excluded to eliminate the interference caused by the movement of the beam stopper located close to the SEM and the settling time of the electrometer at low currents. The SEM yield  $\eta$  for the given bias voltage was calculated by dividing the mean signal current by the beam current. The relative error  $\epsilon_\eta$  was calculated as follows.

$$\epsilon_\eta = \sqrt{\epsilon_{beam}^2 + \frac{\hat{\sigma}_\eta^2 / N}{\eta^2}} \quad (6.1)$$

Where  $\hat{\sigma}_\eta^2$  is the variance of the acquired current data set,  $N$  is the number of the



(a) Prototype CII assembly with a grounded Al plate

(b) Prototype F assembly

Figure 6.7: SEM Prototypes without their steel housings used for calibration with beam.

samples in the data set and  $\epsilon_{beam} = 0.05$  is the relative error of the beam intensity.

## 6.2.2 Results and comparison with simulations

The bias voltage was varied from 2 V to 1.5 kV and the resulting plots for both detector types are presented on the Fig. 6.8. The corresponding simulation of the Type F SEM was performed with Geant 4.9.0 with the parameters listed in the Table 6.1.

Beam energy	62.9 MeV
Beam shape	round
Beam radius	4 cm
Energy spread	0
Beam divergence	1.7 mrad
Range cut	9 $\mu m$
Primaries	10 000
Runs	11

Table 6.1: Geant4 simulation parameters for the 63 MeV tests in PSI.

The Type CII SEM has a considerably higher signal than the F type due to a stronger backscattering caused by the large ceramic disk. A very weak dependence of the response on the bias voltage can be observed for both detectors when using the logarithmic scale. This behavior could not be reproduced by the simulations, because there was no energy spectrum of the secondary electrons implemented and the delta electrons were not produced at the energies comparable to the field strength. This

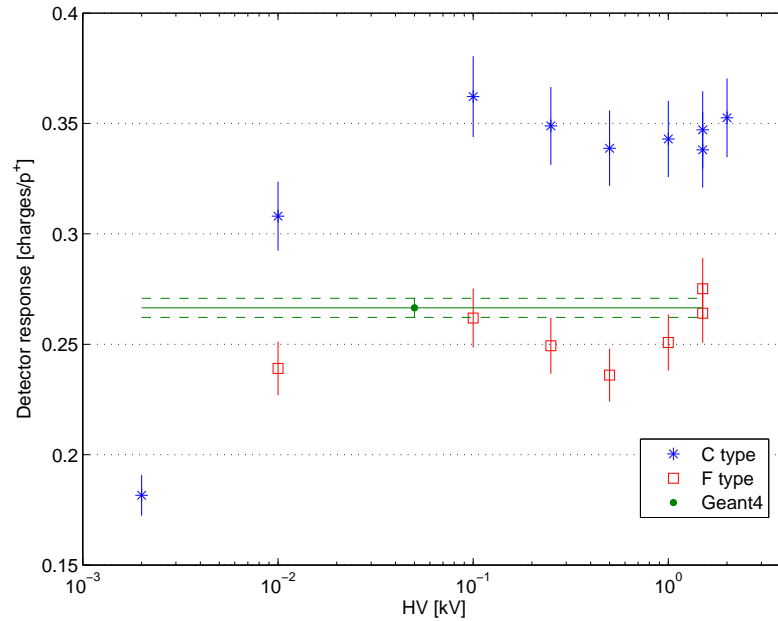


Figure 6.8: Response of the SEM normalized to the beam current for different bias voltages and two detector versions (63 MeV cyclotron proton beam in PSI) compared to the simulation.

effect was not further investigated as it has no impact on the normal operation of the detector.

The size of the primary beam in Geant4 was comparable to the one in PSI and the same scaling by the active electrode surface was used as was the case for the measurements. The simulation result is in a very good agreement with the measurement and validates the simulation model for low energies. The Bragg peak of the protons with the energy of 63 MeV before entering the chamber lies in the steel bottom cover of the SEM. The energy of the primary protons is largely degraded in the bottom cover, therefore the protons passing the signal electrode have a very low energy causing a high  $dE/dx$  and thus a high SEY which strongly changes with energy as can be seen on the Figure 4.11. At this energy, there are nearly no delta electrons produced, so this is a test of mainly the SEY parametrization.

### 6.3 Calibration by bunched proton beam at 1.4 GeV

Measurements in the CERN PSB were performed in May and June 2006. Due to the access restrictions and a delay in production only an older prototype CII version of the SEM could be tested.

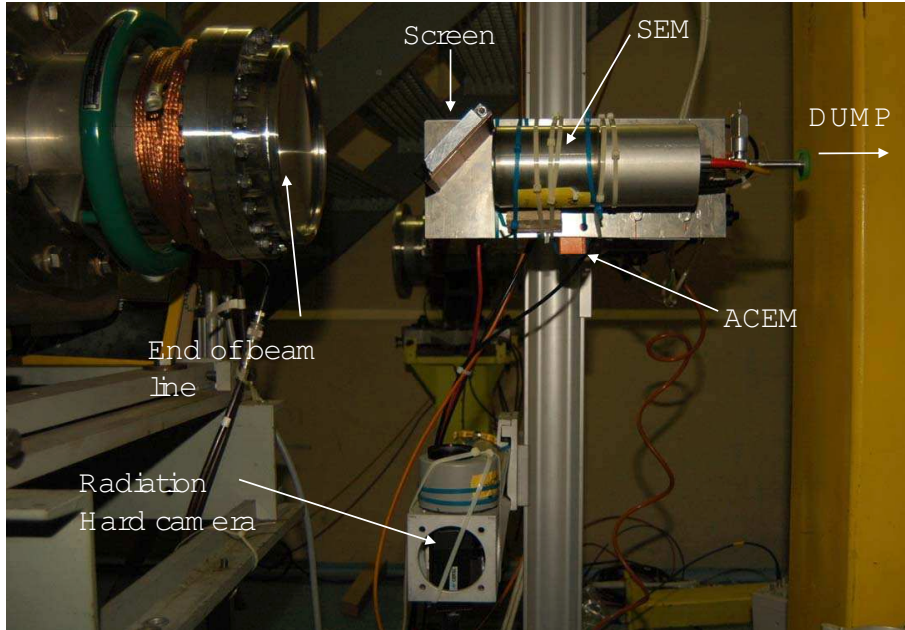


Figure 6.9: measurement setup in the PS Booster dump line.

### 6.3.1 Experimental setup

The Type CII SEM was installed at the end of the PS Booster dump line on a movable support. The bias voltage was connected by a 180 m CBH50 cable to the high voltage power supply installed in the surface building. The signal was collected by a digital oscilloscope TEK TDS440 terminated by a  $50\Omega$  resistor and connected via 180 m of a coaxial CB50 cable. A reference Aluminum Cathode Electron Multiplier tube (ACEM) detector with a fast response time was installed close to the SEM but outside of the beam. The beam was aligned using a luminescent screen centered to the longitudinal axis of the chamber and an intensified radiation tolerant CCD (Cidtec[32]) camera recording the produced images. Unfortunately, the camera was not operational during the second session, so the alignment was done just by using the chamber output current. The beam intensity was measured by a Beam Current Transformer (BCT) in the extraction line.

The setup overview can be found on the Figure 6.9. The beam was entering the SEM through the bottom cover and ending up in the beam dump block few meters downstream. The beam cycle (TSTPS) had only a single bunch from the ring 4 of the PSB. The beam intensity was limited to a maximum of about  $2 \cdot 10^{12}$  protons due to the radiation alarms caused by the secondaries created in the chamber. The lower limit was set by the resolution of the BCT to  $5 \cdot 10^{10}$  protons per bunch.

The integration of the output current was done by a Matlab script. The peak current was found for every profile and the threshold was set to 5% of the peak, as the

noise level was quite low. The response was calculated by dividing the integrated output charge by the bunch charge. The error of the integration method was estimated to 1.5% caused mainly by the uncertainty of the termination resistance. The measurement error of the BCT was estimated to a rather optimistic 1% of the measurement range ( $4 \cdot 10^{12}$  charges) and 5% of the actual value. The errors were added in quadrature as they should not be correlated. The solid line on the Figure 6.10 was produced as a weighted mean by the following formula[33].

$$\bar{x} = \frac{\sum x_i/\sigma_i^2}{\sum 1/\sigma_i^2} \quad (6.2)$$

And the variance of the weighted mean is given by

$$\sigma_{\bar{x}}^2 = \frac{1}{\sum 1/\sigma_i^2} \quad (6.3)$$

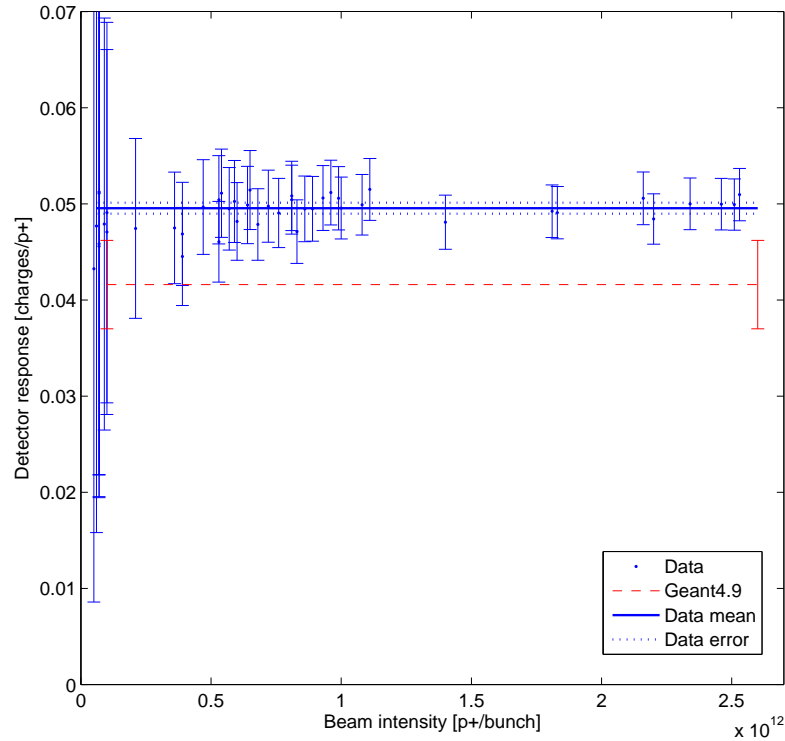


Figure 6.10: Normalized response of SEM (type CII) to a 1.4 GeV proton bunch passage compared to the Geant4 simulation.

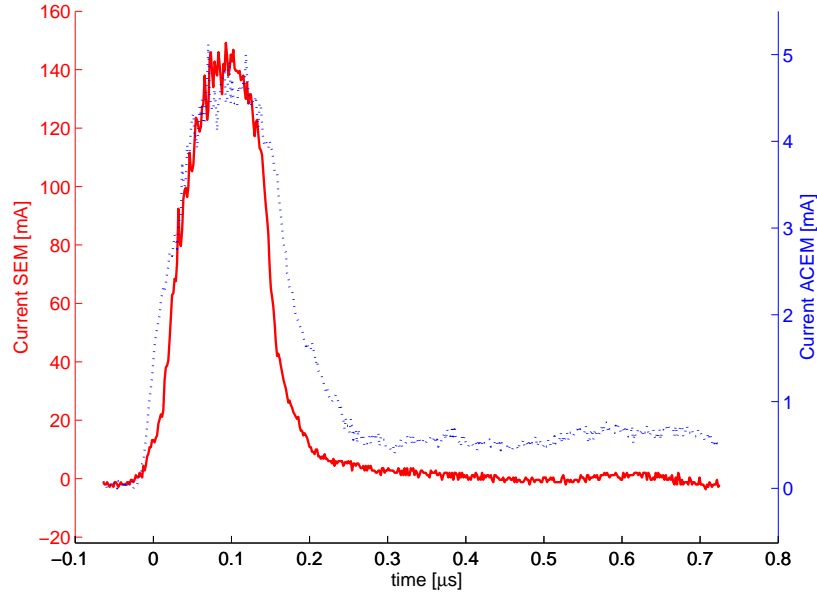


Figure 6.11: Response to single bunch of  $1.1 \cdot 10^{12}$  1.4 GeV protons compared to a reference ACEM detector. The maximum current corresponds to 180 MGy/s.

### 6.3.2 Results and comparison with simulations

The simulation parameters in Geant4.9.0 were set according to the Table 6.2. The setup contained only the F Type chamber and excluded the luminescent window or the support of the detector. The radial beam profile was set to a symmetrical Gaussian distribution. The observed beam shape was rather asymmetric, but it was found that the beam size had a little influence on the result (i.e. dividing the size by 2 increases the result by 3%).

Figure 6.10 shows a very good linear behavior of the detector without any signs of saturation as it is the case on Figure 6.3. When the dose calibration of the SEM is applied to the response, the maximum measured dose rate during the experiment was  $\sim 400 \cdot 10^6$  Gy/s. The SEM response is a factor 5 smaller compared to the measurement with the 62.9 MeV beam. The absolute response is higher than the one simulated, but only the Type F design was implemented in Geant4 and not the actually measured CII Type. The response difference between the two detectors previously measured (see Fig. 6.8) with the 63 MeV beam was 21% at 1.5 kV bias, which is comparable to the 16% between the simulation and the measurement. Additional unknown calibration errors of the BCT might also influence the measurements.

The response time to a single bunch passage was compared to the fast ACEM detector (blue curve on Figure 6.11). The signal of the ACEM is produced by secondary

electrons drifting in vacuum and passing through the multiplication dynodes. The signal of the SEM is driven only by electrons drifting in vacuum without the multiplication, so its signal should be slightly faster than for the ACEM. It is the case on the falling edge of the Figure 6.11, but the ACEM is faster on the rising edge, which is most likely caused by the saturation and therefore a nonlinearity of the dynodes. The longitudinal bunch length was set to 160 ns ( $4\sigma$ ) and was correctly measured by the SEM.

## 6.4 High energy proton beam scan across the SEM

The agreement with the simulations was already tested for protons at the energy very close to the entrance threshold (PSI) and close to the minimum ionising energy (PSB). To cover the possible energy range of the LHC radiation field, a measurement at a very high proton energy was necessary. It is very difficult to execute such a tests with the CERN SPS primary beam as even the dump line is completely under vacuum. The only accessible area is a small gap between the end of the transfer line to the North Experimental Area and a dipole just before the primary target.

### 6.4.1 Experimental setup

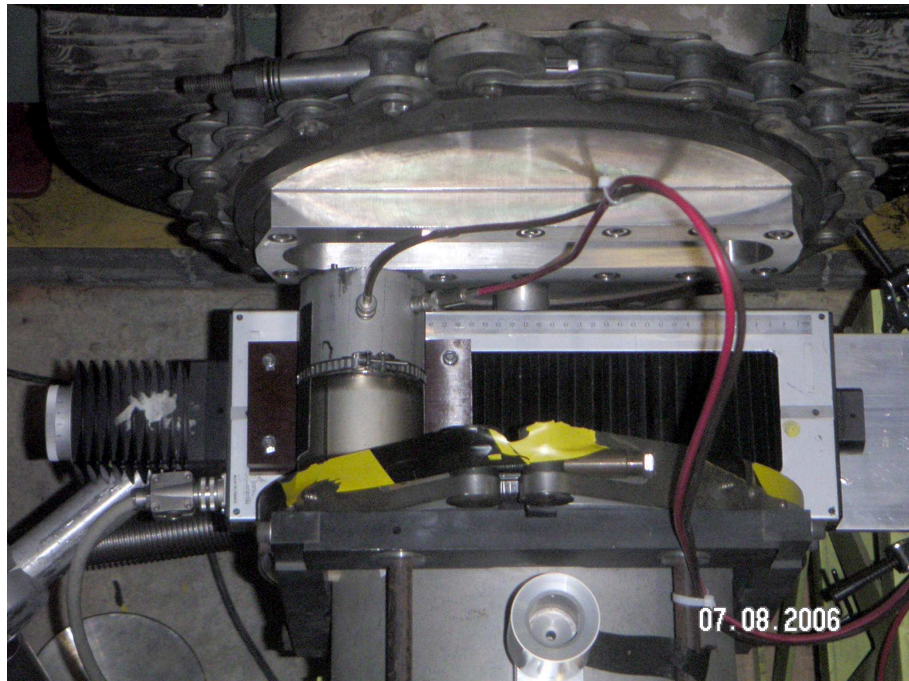


Figure 6.12: SEM version Fb installed in the 400 GeV TT20 transfer line on a movable stage. The beam is coming from the bottom of the picture.

A shorter version of the SEM (Type Fb) was installed in the SPS TT20 transfer line for the calibration purposes. It was placed on a movable stage between two vacuum sections of the beam pipe few meters before the primary target T2. The top view of the setup is presented on the Figure 6.12.

The table was moved horizontally by a precise stepping motor with a reproducibility of 0.1 mm. The steel cover tube of the SEM was shortened to fit the detector longitudinally in the small gap. The connectors were passing through the side of the connection box to avoid an accidental damage of the thin titanium vacuum windows of the beam pipes. The signal connector was fixed just against the signal feedthrough, so it could be used for the radial alignment of the chamber. The transverse profile of the proton beam was estimated to be about 2 mm rms (from previous experience [27]) and a conservative misalignment of  $1^\circ$  with respect to the longitudinal detector axis was assumed, as the measurement shows a left-right asymmetry. The charge produced by the SEM during each slow extraction (4.7 s) was integrated by the standard SPS low noise secondary emission beam screen electronics and the beam intensity was measured by a secondary emission beam screen of the corresponding transfer line.

When the SEM chamber is placed in the beam, the quality of the extracted beams produced after the target is greatly reduced, so the measurement time was very limited. Only one complete and one rough scan could be therefore acquired. The uncertainty of the integrated measurements was estimated to 10%.

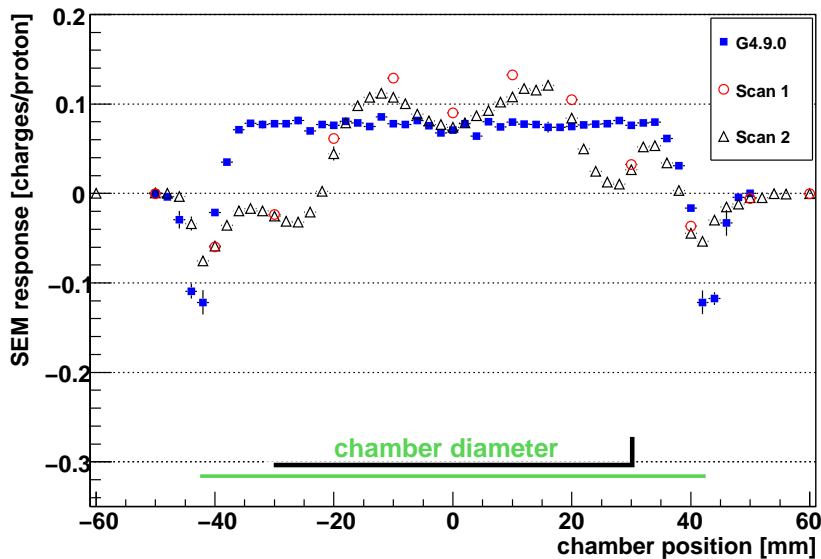


Figure 6.13: Simulation and measurement of the SEM response while moved stepwise through a 400 GeV proton beam.

### 6.4.2 Comparison of measurements with simulations

Each measurement point (see Fig. 6.13) represents one slow extraction passing through the bottom of the detector transverse to the surface of the electrodes.

The negative signal peaks are created when the beam passes through the detector walls (and parallel to it) and produces a large number of low energy ionisation electrons. The electrons have enough energy to overcome the opposite electric field and hit the signal electrode without passing through the bias electrodes. This effect is discussed in detail in the Sect.4.2.3 (for the corresponding schema see Fig. 4.3). The simulation was successful in reproducing the signal pattern only partially, probably due to the not very well known alignment and the angular spread of the beam during the experiment. Another parameter, which very likely influencing the measurement result is the structure of the electronics box cover plate. In the simulation model, it was implemented as a full round plate, whereas in reality it had holes prepared for the feedthroughs and an additional asymmetric hollow part. Unfortunately, their position and orientation was not documented before the experiment. The relevant relative disagreement between the measurement and the simulation is obtained after integration of the area under the data points from the Figure 6.13.

The disagreement between the individual measured and simulated points on the Fig. 6.13 is not relevant for the estimation of the accuracy of the simulations. During the operation, the SEM will be exposed to the radiation fields larger than the detector size, so the comparison of the above mentioned integrals is much more relevant. The relative disagreement between the two integrals is 29%. The results are presented in the Table 7.1 summarizing all the calibration measurements of the SEM.

## 6.5 Test in muon beam at 160 GeV

The SEM was also tested in the relatively high flux muon beam of the fixed target COMPASS experiment. The beam is produced by a slow extraction process from the SPS, so it comes in 4.8 s long spills with the average intensity of  $2.2 \cdot 10^8$  muons.

The detector was fixed on a steel construction in front of the fixed target area. The output was connected via 15 m of CK50 double shielded coaxial cable to the Keithley 6517A electrometer. The produced charge was integrated during each spill and the beam intensity was provided by the wire chambers belonging directly to the COMPASS experiment. There was unfortunately only a little time available, so the acquired statistics is poor and the signal to noise ratio very low. Nevertheless, the measured response was  $0.059 \pm 0.016 e^-/\mu$  while the corresponding Geant4 simulation provides  $0.08 \pm 0.008 e^-/\mu$ , which results in a relative difference of 26%. The measured current

corresponds to about 0.5 mGy/s when the dose calibration of the SEM is applied.

## 6.6 BLM system tests in the SPS collimation area

A prototype of the LHC secondary graphite collimator (TCSG) was installed in a Long Straight Section (LSS5) of the SPS accelerator in 2004 (see Fig. 6.16). The setup was used as a "testbed" for the LHC BLM system in the collimation region including the complete measurement and data acquisition chain. It was equipped with several LHC type BLM ionisation chambers and in 2007 also with SEM chambers.

During November 2007, a test was performed with a PS 26 GeV proton beam injected directly onto the TCSG. The measured loss data were acquired by the LHC BLM electronics and saved in the LHC measurement database. The simplified setup used for the measurements and described in the following section was implemented into the Fluka[9] simulation program by T. Böhlen and the simulated energy deposition was compared to the measurements.

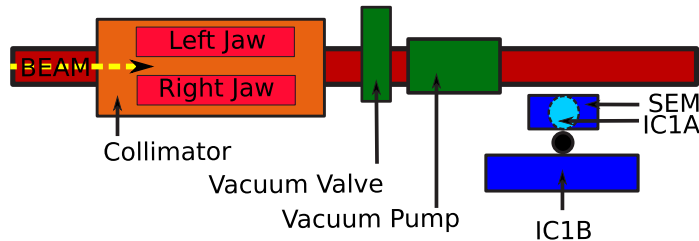


Figure 6.14: Schematic top view of the experimental setup in SPS. The beam impacts on the jaws of a horizontally mounted LHC secondary collimator (TCSG). Two ICs and one SEM detector are mounted downstream of the collimator. The beam pipe between the collimator and the detectors contains a vacuum valve and a vacuum pump. Courtesy of T. Böhlen.

### 6.6.1 Experimental setup

The region downstream the TCSG was finally equipped in November 2007 with a simplified system consisting of two ionisation chambers (IC1A and IC1B) and one SEM detector on a single support (see Fig. 6.14). The signals were connected to three individual CFC front-end cards with about 200 m long signal cables.

The SEM was connected to the HV power supply via a large capacitor and a  $1M\Omega$  resistor exactly like in the LHC collimation areas. The IC1A was also connected in the same way as in the LHC, so it contained an additional current limiting resistance (see Fig. B.1 in the attachments). The ground of the high voltage cable is disconnected at

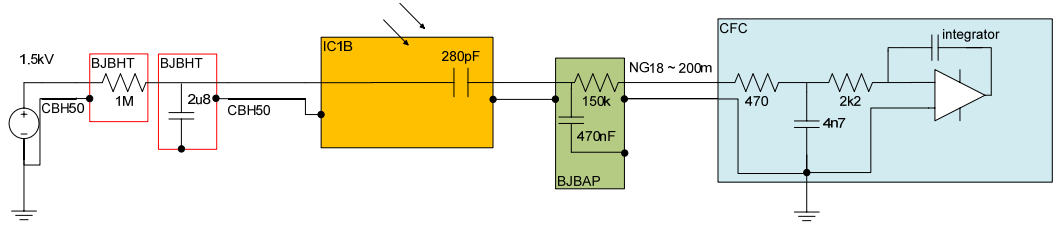


Figure 6.15: Schema of the signal and bias voltage connections for the ionisation chamber IC1B equipped with a long time constant RC filter.

the level of the HV capacitor to avoid a ground loop, as the chamber is grounded also by the signal cable.

The second chamber IC1B was equipped with an RC filter to slow down its response and therefore limit the peak current measured by the CFC as presented on the Fig. 6.15, in order to be able to measure the secondary shower particles of the collimator jaw at the same time as the SEM for large fast losses. Due to the presence of the filter, the protection resistance ( $150\text{ k}\Omega$ ) was removed from the electronic box of this chamber.

The beam intensity respectively the number of protons hitting the collimator was measured by a fast beam current transformer (FBCT) in the transfer line TT10 from PS to SPS. Due to the beam losses occurring during the injection process, the beam intensity in the SPS ring was measured with a slow BCT with the collimator fully retracted. The relative difference between the two transformers was then subtracted from the FBCT values. The beam intensity was varied by changing the number of bunches and not by varying the bunch current. The beam profile was measured by rotating wire scanners.

The Fluka model was used for simulating the energy deposition in the collimator jaws (during a proton beam impact) and at the same time in the sensitive volumes of the two ionisation chambers.

The signal of the SEM had to be estimated indirectly in two different ways. First, only the steel vacuum container was included in the model and every particle entering the inner volume triggered a scoring procedure, which saved the type, kinetic energy, position, momentum vector and the statistical weight<sup>1</sup> of the corresponding particle into a text file. The produced list was then used in a GEANT4 SEM simulation as an input for generating particles. The combined result of the two simulations was the number of electrons produced per proton impacting on collimator ( $1/N_{poc}$ ).

The other way to simulate the response of the SEM was similar to the method used in the H4 experiment described in Sect.6.8. The volume inside the SEM vacuum

<sup>1</sup>Fluka program uses biasing methods, which help to decrease the statistical fluctuations of the simulation results. More details can be found in [80].

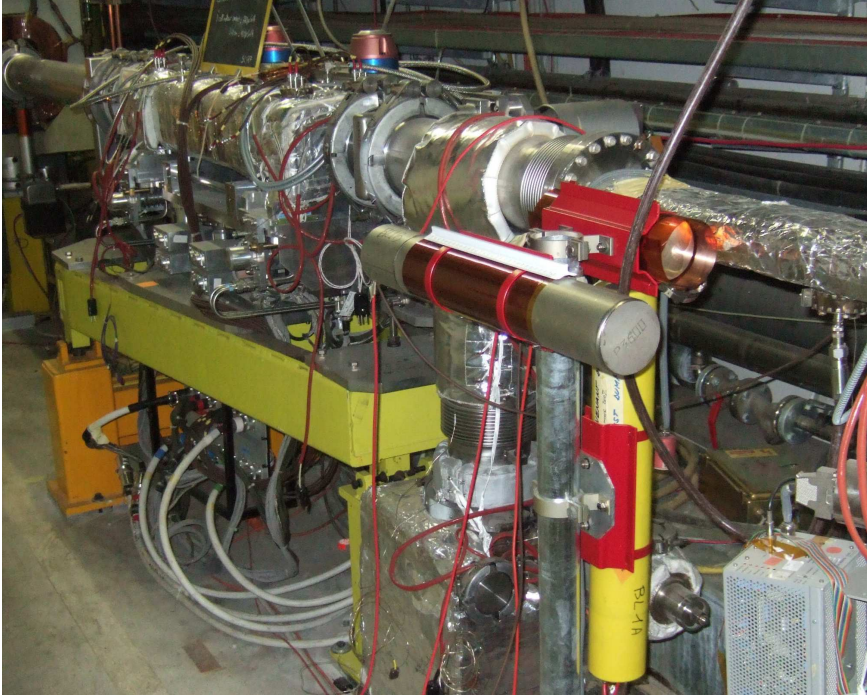


Figure 6.16: Secondary LHC collimator (TCSG) installed in the straight section LSS5 of SPS. The support with the SEM (small chamber), one vertical ionisation chamber (IC1A) and one horizontal (IC1B) is located on the right from the collimator beside a vacuum pump.

container was filled by air at 1 bar pressure and the total energy deposited in the gas was scored for every impacting proton. The mean deposited energy per  $N_{poc}$  was divided by the weight of the air inside the SEM, to give the mean dose deposited per  $N_{poc}$ .

### 6.6.2 Results and comparison with simulations

The statistical weight attributed to every particle in the output Fluka file was often lower than one. The common practice in energy deposition studies, where ionisation signal is involved, is to treat all the primary particles in the same way and only scale the final energy deposition by the weight of the original particle. This method is nevertheless not very well suited for the SEM simulations as the signal produced per primary is an integer number of charges, which is often zero assuming a SEY of few %. The variance of such simulations would be too high, so another method was employed to decrease the variance of the result. Each weight was multiplied by a factor 100 (the minimum weight was 0.1) and every particle from the list was sent weight times through the SEM detector. The resulting signal had to be divided by 100 and also by the number of primary protons ( $N_{poc}$ ) used in the Fluka simulation.

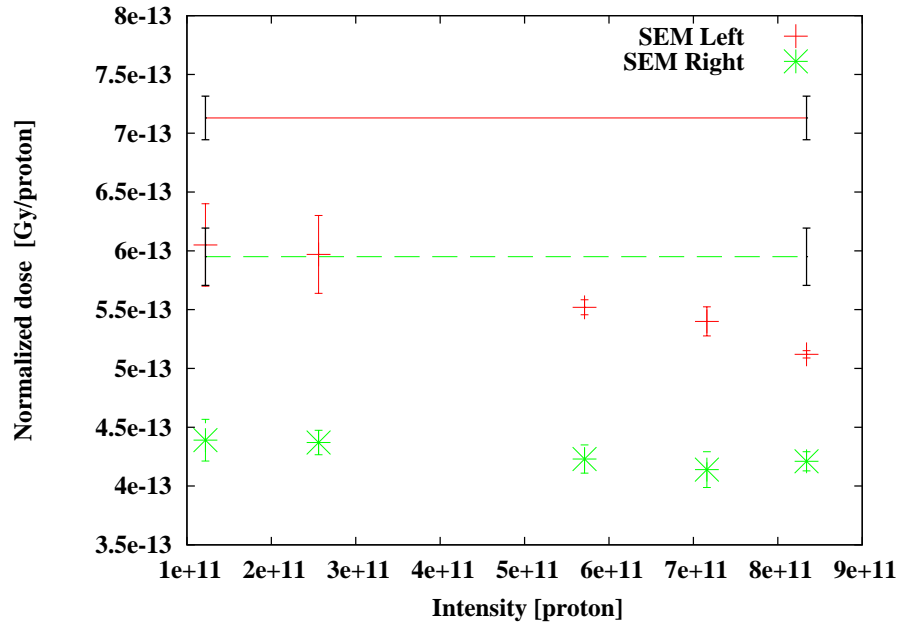


Figure 6.17: Normalized response of SEM during the LHC collimator tests in the SPS for a 26 GeV proton beam dumped on the left or the right jaw for different beam intensities. Horizontal lines represent the results of the Fluka simulations.

The resulting normalized response of the SEM (see Fig. 6.17) is decreasing by about 20% for higher intensities but only for the beam impacting on the left jaw. A systematic effect related to the transverse bunch position change and a longitudinal misalignment of the jaw is most probably causing the signal decrease. A detailed analysis of this effect can be found in [80].

The results of the simulations and the corresponding measurements are summarized in the Table 6.4. It includes also the response estimated by launching the secondaries saved by Fluka through the SEM in GEANT4. The difference between the dose estimation performed only by the energy scoring in the gas directly in Fluka and this method is 20% respectively 26% for the left jaw. Such a relatively small difference allows to use the simplified energy scoring procedure for estimating the signal in the LHC collimator areas.

The relative difference between the simulation and the measurements for the high beam intensity Session 1 is consistent with the Session 2 measured at lower intensities and with larger beam size. The jaw position, on which the beam impacts on has a little influence (of only 2% if moved by 5 mm) on the simulation result according to [80]. In contrary, the positioning of the complementary jaw has a large impact on the simulated SEM signal.

## 6.7 Linearity measurements in the SPS beam dump area

The linearity of the SEM monitor response was tested in the 1.4 GeV proton in PSB, but the behavior of the SEM under high flux mixed field radiation similar to the one expected in LHC had to be assessed as well. The experiment was used also for testing the response of the LHC ionisation chamber (IC) in direct comparison to the SEM. The standard LHC BLM electronics was employed to measure the output signals.



Figure 6.18: SPS high energy internal beam dump (green block) with SEM and IC on a chariot below (lower right corner). The beam impacts on the left side of the dump block.

One of the most radioactive places of the SPS accelerator was chosen as the location of the experiment. The high energy internal beam dump called TIDV (see Fig. 6.18) serves as a beam pipe during the normal SPS injection-acceleration cycle. When the SPS beam has to be safely aborted after the acceleration, a set of fast kicker magnets deflects down the beam vertically and spreads the beam slightly in the horizontal direction. The beam then hits the 2.5 m long graphite core of the dump, which is followed by 1 m of aluminium, 0.5 m of copper and finally 0.3 m of tungsten. The dump core is enclosed in a copper cylinder, which is then inserted in an massive iron shielding.

When a beam abort is requested for beam energies below about 80 GeV, the beam is automatically directed towards the low energy beam dump TIDH located several tens of meters upstream the TIDV.

### 6.7.1 Measurement setup

Due to the high remnant radiation close to the dump (up to 12 mSv/h), the measurement setup had to be made to allow easy and fast installation. One SEM and one IC were placed together on an insulated chariot with small wheels, which permitted a quick placement of the chambers under the dump. The detectors were connected by thick 80 m long CK50 coaxial cables to the LHC BLM front-end electronics installed 80 m downstream the TIDV in the SPS tunnel. Each detector had its own high voltage cable and power supply (set to 1500 V). In order to avoid cross talks inside the front-end cards, each detector was also measured by a separate card. The cards were connected by a pair of long optical fibers to the acquisition boards. The BLM data were integrated by different running sum windows ranging from 40  $\mu$ s to 20 s.

All the running sums were saved every second by an expert application into a text file and the BCT values were saved in the standard LHC measurement database. The timing of the BLM acquisition system and the SPS BCT were not synchronized, so there was a fixed time delay between the corresponding acquisitions. The running sums shorter than 1.2 s show the peak value of the integral obtained during the last second. The rest of the sums show the actual integral at the acquisition time.

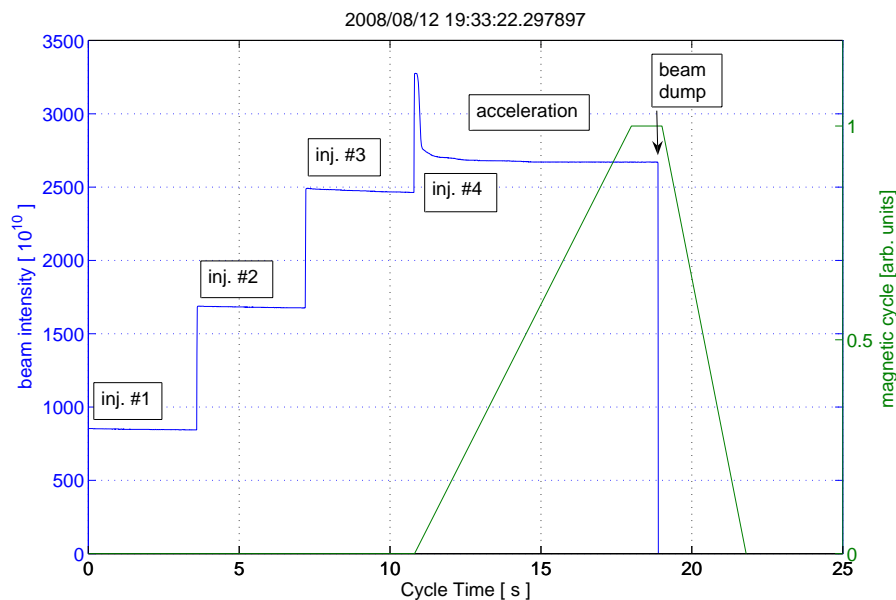


Figure 6.19: Beam intensity in SPS for one cycle with LHC type proton beam. Four batches are injected from the PS and dumped after acceleration to 450 GeV.

The beam intensity was measured by a dedicated fast beam current transformer (BCT). The regular beam dump is normally requested at the end of the cycle for slowly extracted fixed target beams or the LHC test beams. An event trigger is re-

ceived by the electronics few milliseconds before the dump and the last acquisition of the BCT is saved in the database. This method works well for the scheduled regular dumps, but gives often zero values for emergency dumps as the event timing can be incorrect. The measurement error of the BCT was estimated in the same way as for the PSB experiment (Sect. 6.3) to 1% of the measurement range ( $4 \cdot 10^{13}$  p+) plus 1.5% of the measured value. The beam is dumped in  $7.8 \mu s$ , as the LHC type beam fills only about 4/11 of the SPS circumference.

The LHC BLM ionisation chamber (IC) installed beside the SEM would have a far to large peak signal if used only with the standard front-end electronics. The signal cable of the IC was therefore equipped with a simple filter for reducing the peak current by stretching the signal. The filter was composed from a  $4 \mu F$  capacitor and a  $20.7 k\Omega$  resistor forming an RC element with a time constant  $\tau$  of 83 ms. Nearly the entire charge (99.3%) produced by the IC during a single dump should be therefore integrated in about 414 ms, which corresponds to  $5\tau$ .

### 6.7.2 Measurement results

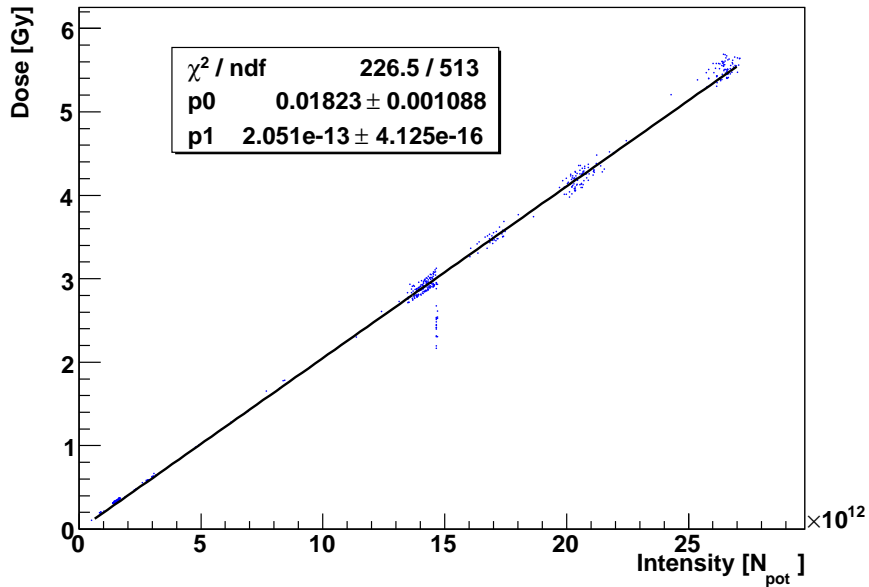


Figure 6.20: SEM linearity measurement with 450 GeV LHC type beam dumped after acceleration. Every point represents a dose integrated during 10.2 ms for the given number of protons dumped ( $N_{pot}$ ).

There are no simulations available for the energy deposition in the area around the TIDV, therefore only relative the comparisons are possible. The data set including a

wide range of beam intensities with constant beam parameters is taken in the period from 12 to 13 August 2008, when only the LHC type cycle was present in the SPS which was dumped regularly each cycle. At the beginning of the measurement, four batches (each containing 72 bunches) were injected from the PS as shown on Fig. 6.19. The large intensity drop after the last injection is caused by the beam losses occurring at the beginning of the acceleration. The number of batches had to be decreased after few hours due to the strong pressure increase inside the TIDV caused by overheating of the graphite core.

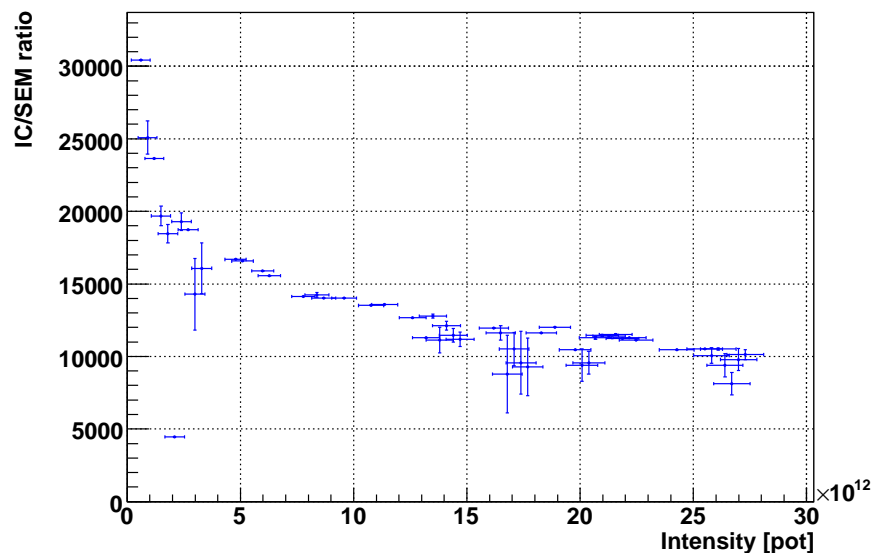


Figure 6.21: Charge produced by the IC during a 450 GeV proton beam dump divided by the corresponding charge from the SEM. The IC signal was integrated for 1.3 s (RS09), the SEM signal for 10.24 ms (RS06).

The resulting response of the SEM for the 10.2 ms sliding integration window (running sum 6) plotted against the beam intensity is shown on the Fig. 6.20. The noise pedestal was estimated from the periods without beam and subtracted from the data. The pedestal is formed mainly by the constant 10 pA offset current. The running sum 6 had the best signal to noise ratio and the shorter integrals had lower values. The pulse length at the electronics input is therefore smaller than 10.24 ms but greater than the next shorter running sum being 2.56 ms long. The long pulse duration is probably caused by the fast decaying radioactive isotopes produced during the dump, but more studies are needed to confirm the origin of the effect.

The data are fitted with a linear function. The same statistical error (3.4%) attributed to all the data points was calculated as a standard deviation of the SEM

response normalized by the beam intensity. One can see that the fitted value for the offset is very small compared to the measured dose values, so it can be then safely assumed, that the line passes by zero.

There are several points with the same intensity of about  $1.5 \cdot 10^{13}$  protons, which apparently do not match the fitted line. The intensity matches two batches after the acceleration loss, so the points correspond most likely to the emergency dumps during the energy ramp and the recorded signal is lower due to the lower beam energy.

The ratio of the signals between the ionisation chamber and the SEM should match in the ideal conditions (low dose rates and no noise) the ratio of their dose to charge calibration factors. The calibration factor of the SEM is  $(764 \pm 84)$  pC/Gy and for the IC  $(54 \pm 10)$   $\mu$ C/Gy. The ratio is then  $(7.1 \pm 1.6)10^4$ . The actual dose rate during the beam dump is so high, that the response of the IC is strongly influenced by the space charge saturation effect making the response non-linear[26]. It should be also noted, that the maximum dose measurable by the IC connected to the standard LHC BLM electronics is 0.92 mGy for the shortest integration interval of 40 us (resp. 23 Gy/s), which is about two orders below the measurement range of this experiment.

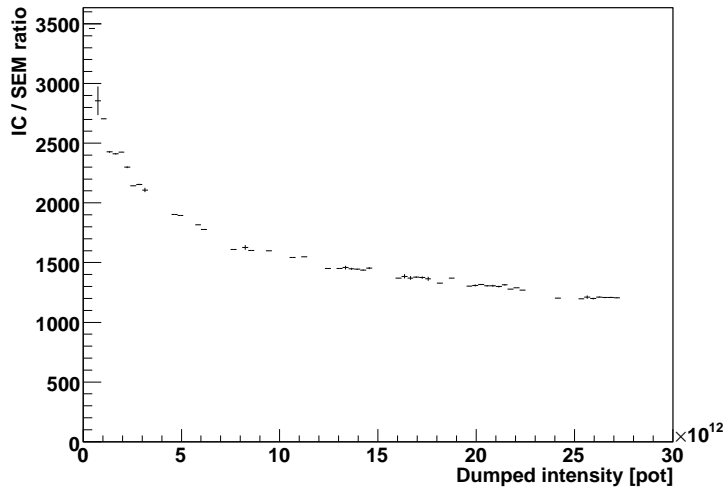


Figure 6.22: Charge produced by the IC during a 450 GeV proton beam dump divided by the corresponding charge from the SEM. The signals were integrated for 10.24 ms (RS06).

The large error bars for some beam intensities on the resulting plot shown on the Fig. 6.21 are caused by the large difference between the two integration periods. The data acquisition frequency is 1 Hz and is not synchronized with the beam dumps. If the beam dump occurs for example several tens of ms before the acquisition, the SEM

signal is integrated correctly, but a large part of the IC signal is still not yet integrated. If the running sun 6 is used for both monitors, the curve is much smoother as presented on the Fig. 6.22. The absolute values of the ratio are much smaller than for the previous plot as only about 10% of the signal from the IC is integrated after 10.2 ms due to the presence of the filter.

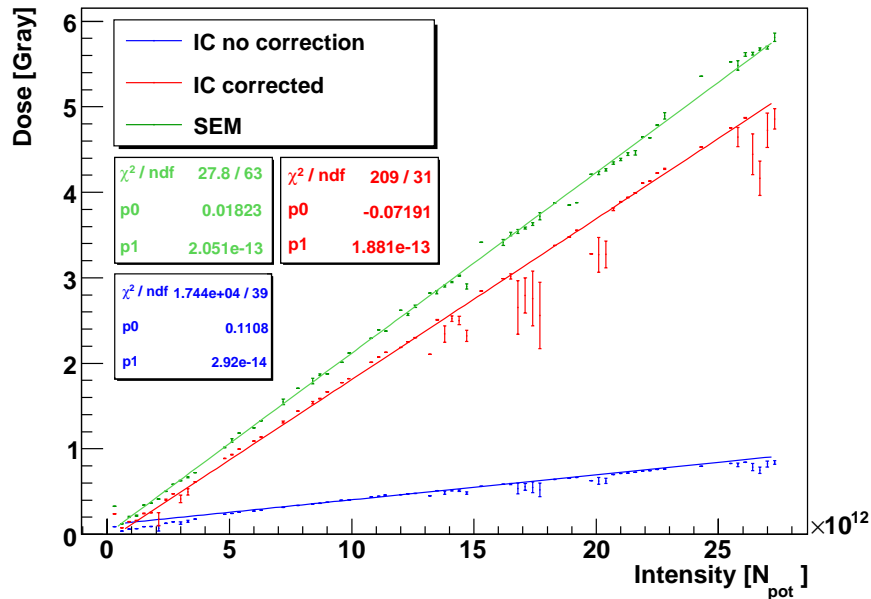


Figure 6.23: Comparison of the SEM response, the IC corrected for the space charge saturation effect and the IC uncorrected. The curves are fitted with linear functions.

The space charge effect mentioned above is caused by the large number of positive ions, which drift to the signal electrode much slower than the electrons. At a given dose rate, the field created by these ions is so high, that it starts screening the bias voltage between the electrodes and a gap without field is created. The ions located in the gap are usually lost by recombination or diffusion, which lowers the response of the detector. The saturation effect can be corrected by using the space charge correction formula from [26]. The data from the IC were therefore corrected and plotted together with the SEM on the Fig. 6.23. The errors of the fitted values were not included to keep the plot readable. The resulting difference between the slope of the SEM and corrected IC is 8.3%.

The SEM measurements in the SPS dump area were particularly difficult not only due to the high remnant radiation complicating the installation, but mainly due to the electromagnetic coupling (EMC) of the fast injection and dump kicker magnets to the

signal cables. The IC chamber is not so much concerned as it has a very high signal, but the SEM operates at considerably lower currents. The kickers are located upstream the TIDV, so the electronics was finally moved to the tunnel downstream the dump, instead of the surface building, where 200 m signal cables passing along the kickers were needed. This modification improved the signal quality.

Also the high voltage cabling could not be shared by the two monitors, because the large currents produced by the IC were considerably decreasing the voltage on its high voltage capacitor while the SEM capacitor had a stable voltage. The current was then flowing between the two capacitors, which produced a negative current in the SEM. The HV power supply lines were separated, but the best signal quality was obtained by charging the SEM HV capacitor to 1.5 kV and disconnecting the HV cable from the power supply. The SEM was properly working without a recharge of the capacitor for several months without an observable degradation of the signal.

Assuming the SEM works properly until a 50 V bias voltage, the total charge available in the capacitor is  $1450 \text{ V} \times 0.47 \mu\text{F} = 6.8 \cdot 10^{-4} \text{ C}$ , which is equivalent after conversion to dose to approximately 900 kGy.

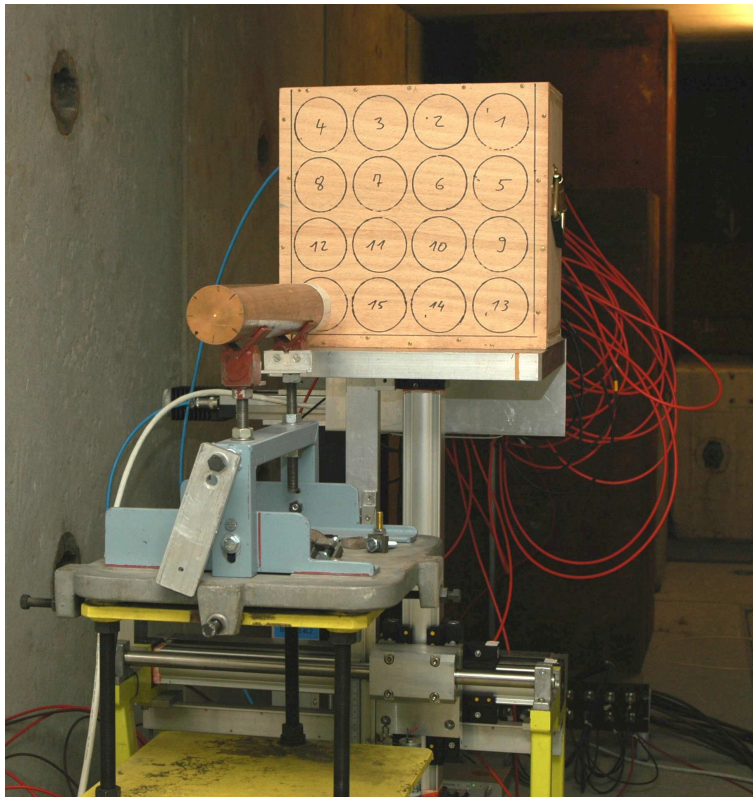


Figure 6.24: Test beam setup with a 20cm Cu target and a container with 16 SEMs on a movable table.

## 6.8 Production validation in a mixed radiation field

One of the possible production non-conformities is a leak in the vacuum container. As the chamber has no internal pressure probe, an upper limit on the pressure can only be established by using a particle beam. The aim of the test beam program is to verify the pressure inside every SEM detector, dark and leakage currents and if possible, the SEY.

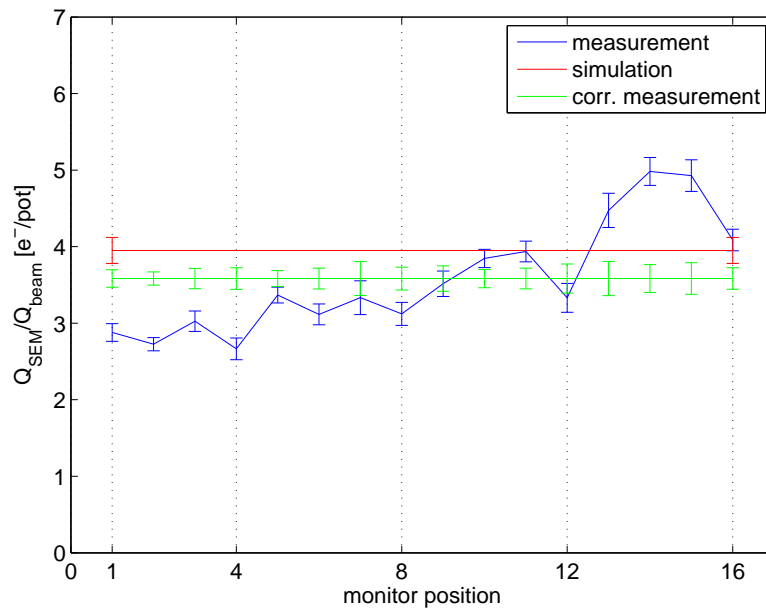


Figure 6.25: Response of 250 SEM detectors for each of the 16 positions in the sample holder. Tests performed in November 2007.

It was decided to build an experiment for testing all the SEMs in a mixed radiation field of a fixed Cu target in the H4 secondary beam line of the North Experimental Area during the high current tests dedicated for the CERF++ studies [41]. It is the only viable solution (at CERN) when a high particle flux and a frequent access to the test area is required.

### 6.8.1 Experiment requirements and setup

The primary requirement for the verification tests is a sufficient Secondary Emission current well above the leakage current of the SEM. Taking into account the maximum available beam current in the H4 area, which is about  $7 \cdot 10^7$  protons per spill of 4.7 seconds, and the response for protons at 300 GeV ( $\sim 0.08 N_{e^-}/N_{p^+}$ ), one obtains the expected current of 0.2 pA which is below the level of the leakage current and the noise in the measurement chain. By placing a target into the beam, the number of high energy

secondaries produced by the hadronic shower can be much larger than the number of particles in the original beam. In order to find the maximum multiplicity (number of secondaries escaping from the target per primary proton) possible, the hadronic shower parametrization was used. According [42], the shower maximum in a target is reached after the penetration depth  $l_{max}$  obtained as follows

$$l_{max} = [0.6 \log(E) - 0.2] \lambda_I \quad (6.4)$$

where  $E$  is the energy of the primary beam in [GeV] and  $\lambda_I$  is the nuclear interaction length, which is 15 cm [2] for the case of copper. The maximum in the copper is then obtained at 19.3 cm. Two pieces of 10 cm copper rods were then installed on the target holder.

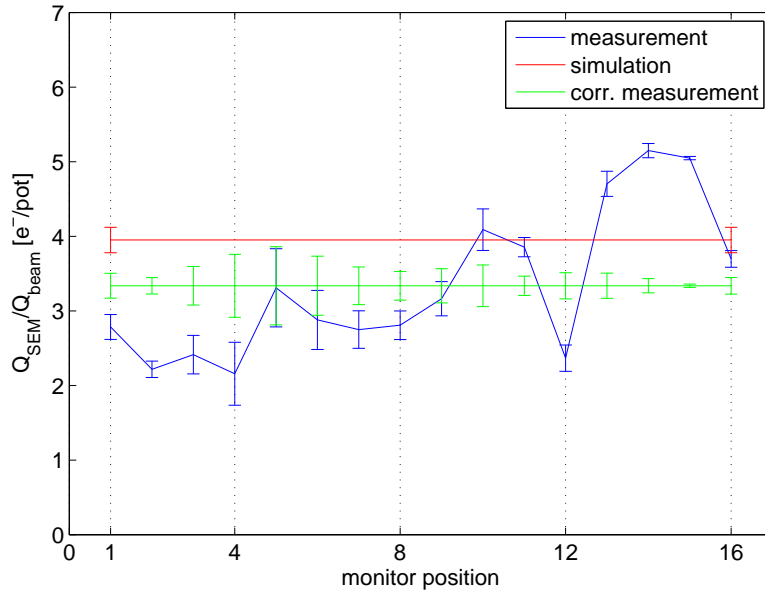


Figure 6.26: Response of 49 SEM detectors for each of the 16 positions in the sample holder. Tests performed in June 2008.

The large amount of the detectors to be tested imposes a use of an automatic or semi-automatic system which could measure several detectors in parallel or at least rapidly one after another with a remotely controlled table movable in  $x$  and  $y$  direction (beam travels along the  $z$  direction). A wooden box housing 16 SEM detectors was placed on the table with the bottom of the detectors at 8 cm from the end of the Cu target. A picture of the setup is presented on the Figure 6.24.

All the chambers were connected in series to a HV power supply set to 1.5 kV. The signal outputs of the SEMs were connected to a custom designed switch array. It was composed of standard relays which provide a very low current in the off state and was remotely controlled. The switch was connected by a low noise 10 m long triaxial cable provided by Keithley.

The resulting charge was integrated by the Keithley 6517A Electrometer and the beam intensity was measured by counting TTL pulses from the calibrated Proportional Ionisation Chamber (PIC) placed in the beam.

### 6.8.2 Results

In total, 250 detectors were calibrated during the H4 test beam in November 2007. Additional beam time was received during June 2008 to test the rest of the production. Unfortunately, only 49 chambers could be tested due to a vacuum leak in the SPS.

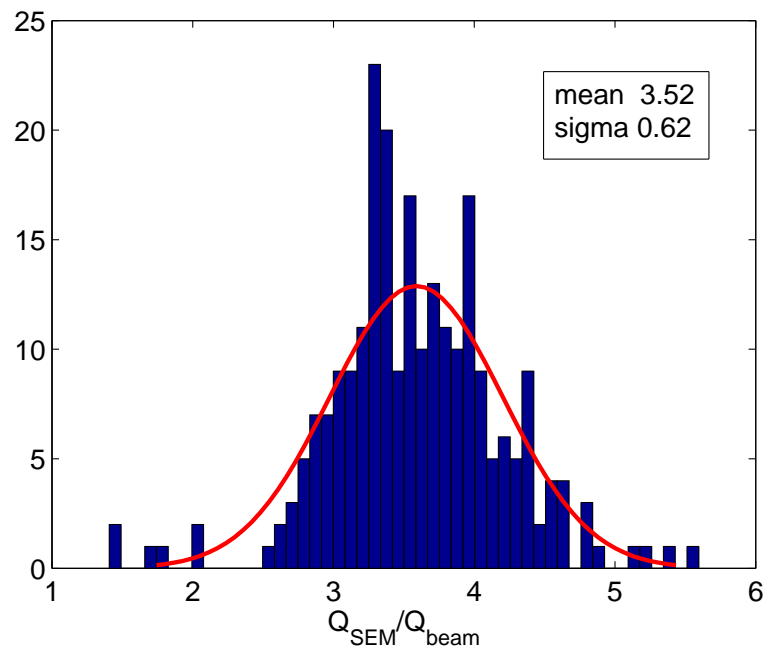


Figure 6.27: Calibration of 250 SEM detectors in a mixed radiation field corrected for systematic position errors. The Geant4 simulation result was  $3.95 \pm 0.17$  charges/proton on target.

There was a systematic offset for each row of the detectors observed. The SEMs located closest to the aluminium plate of the table had the highest response apparently due to the additional scattering of the secondary particles coming from the target. The mean response per position was calculated and the difference from the total mean was subtracted as a systematic error from each detector response. The mean value of the

measured distribution therefore does not change by this correction. The response before and after correction as well as the result of the GEANT4 simulation are presented on the Figure 6.25.

Apart from the signal increase by the table plate, a horizontal misalignment of the beam can be deduced from the plot. All the chambers placed in the positions 4, 8, 12 and 16 corresponding to the left column inside the box (see Fig. 6.24) have a lower response than the other SEMs in the same row, which points to the horizontal asymmetry of the radiation field.

The same effects can be seen on the measurement data from 2008 shown on the Fig. 6.26. The reproducibility is caused by the same beam alignment procedure performed before each of the measurement campaigns. The corrected data used from the plots on figures 6.25 and 6.26 were also plotted as histograms in order to obtain the width of the statistical distribution (see Fig. 6.27 and 6.28).

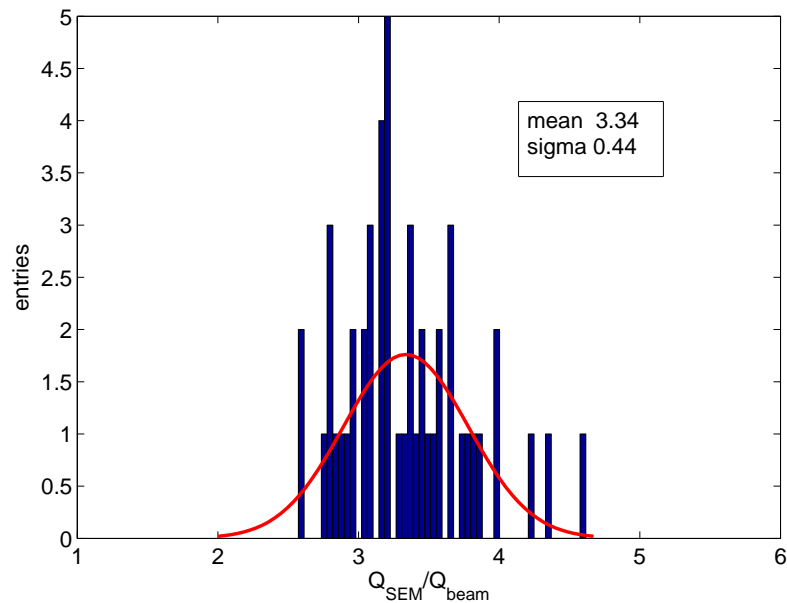


Figure 6.28: Calibration of 49 SEM detectors in a mixed radiation field corrected for systematic position errors. The Geant4 simulation result was  $3.95 \pm 0.17$  charges/proton on target.

The minimum pressure level, which could be measured by the setup depends on the width of the SEM response distribution and the signal produced by the SEM filled by air. Due to the known pressure inside the air filled SEM, the signal rise caused by ionisation adding up to the standard SEM response could be converted into the pressure  $p_{min}$  by the following relation:

$$p_{min} = p_{SA} \frac{3 \sigma_{SEM}}{Q_{SA}} \quad (6.5)$$

where  $p_{SA} = 1$  bar is the pressure inside the air filled SEM,  $Q_{SA}$  is the response of the air filled SEM per proton and the  $\sigma_{SEM}$  is the standard deviation of the measured SEM response per proton. When the parameters from the 2007 measurements are inserted in the formula, the minimum pressure  $p_{min} = 0.21$  mbar is obtained.

The width of the measured distribution is mostly caused by the unequal positioning of the chambers inside the container box, as no particular care was given to the fixation of the detectors. Another contribution to the spread comes from the variations of the beam position between spills, which could not be compensated, because there was no beam position detector close to the experimental area.

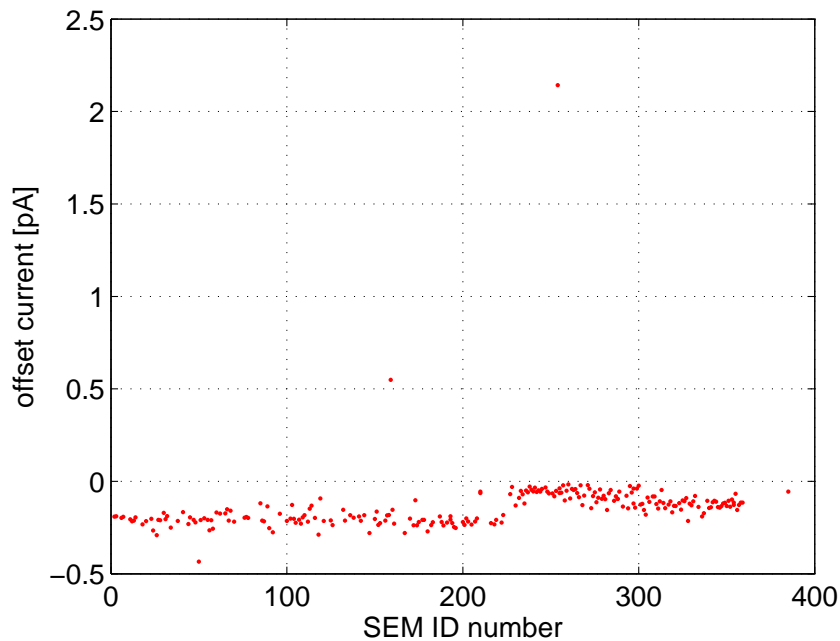


Figure 6.29: Dark current of the 250 SEM monitors plotted versus the production number measured in November 2007. The bias voltage was set to 1.5 kV.

The dark currents were also obtained from the measurement data, as the charge produced by the dark current had to be subtracted from the response data. The actual value was obtained by averaging the charge derivation  $dQ/dt$  for the periods between spills. The limit for the acceptance of the chambers was set to 1 pA.

Only one chamber from the first measurement set had a too high dark current (above 2 pA) otherwise all the detectors measured in 2007 stayed below 0.5 pA. During the measurement campaign from June 2008, three more monitors were rejected due to

their high dark current (see Fig. 6.30). Most of the SEM detectors had a negative offset current (see Fig. 6.29), while the bias voltage was set to +1500 V. Apparently, the guard ring design does not allow the eventual leakage current caused by the bias voltage to enter the measurement chain. Additionally, the offset data shows a sudden change of the mean value for the monitors with a serial number higher than 220. It should be noted, that the detectors were not measured in the order of their serial numbers, but were randomly chosen. The change of the dark current level must be connected to a change in some of the production steps in IHEP, but no apparent reason was found in the production logbooks.

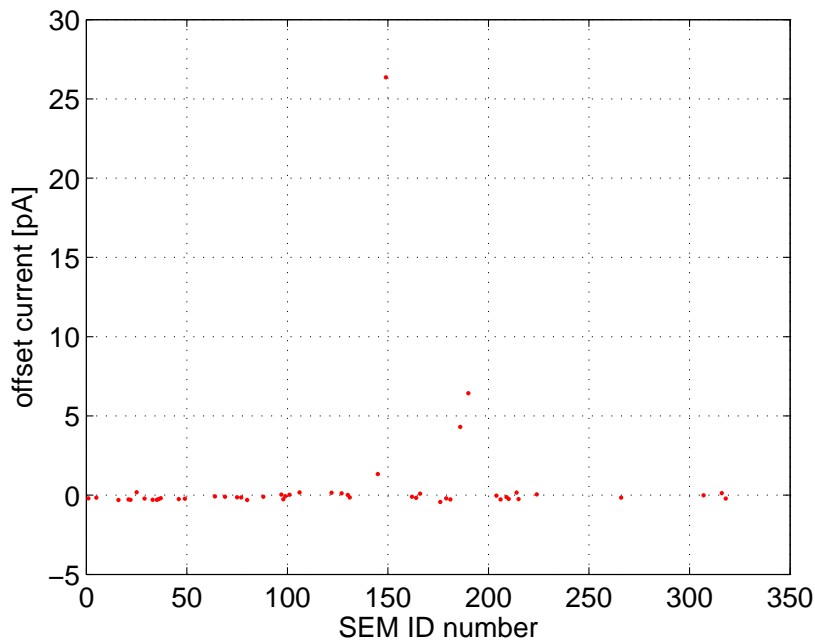


Figure 6.30: Dark current of the 49 SEM monitors measured in June 2008. The bias voltage was set to 1.5 kV.

Beam energy	1.39 GeV
Beam shape	round
Beam sigma	10 mm
Energy spread	0
Beam divergence	$1.7 \mu rad$
Range cut	$9 \mu m$
Primaries	5 000
Runs	11

Table 6.2: Geant4 simulation parameters for the 1.4 GeV proton tests in PSB.

Beam energy	400 GeV
Beam shape	round
Beam sigma	2 mm
Energy spread	0
Beam divergence	$3.5 mrad$
Range cut	$9 \mu m$
Primaries	1 000
Runs	10 per position

Table 6.3: Geant4 simulation parameters for the 400 GeV proton beam scan in TT20.

Session	No. 1	No. 2	
Jaw	Left	Left	Right
Jaw position [mm]	5.5	3.25	1.75
Beam sigma [mm]	1.8	5	5
Beam intensity [ $10^{10}p^+$ ]	1300	13..84	13..84
<b>Measurement</b>	normalized dose/ $10^{-13}$ [Gy/ $N_{poc}$ ]		
SEM (a)	$7.32 \pm 0.12$	$5.73 \pm 0.17$	$4.27 \pm 0.05$
<b>Simulation</b>	normalized dose/ $10^{-13}$ [Gy/ $N_{poc}$ ]		
Fluka (b)	$10.4 \pm 0.3$	$7.13 \pm 0.19$	$5.95 \pm 0.24$
Fluka + Geant4 (c)	-	$9.59 \pm 0.3$	$7.46 \pm 0.17$
<b>Rel. difference (a-b) [%]</b>	30	20	28
<b>Rel. difference (a-c) [%]</b>	-	40	43
<b>Rel. difference (b-c) [%]</b>	-	26	20

Table 6.4: Normalized SEM response measured for direct dumping of the beam on the collimator compared to different simulation methods. Session 2 measurement values are averaged over all intensities. The row with the jaw position lists the jaw position over the center of the beam orbit.

<b>Fluka simulation parameters</b>	
Beam energy	26 GeV
Energy spread	$10^{-3}$
Primaries	10 000 per run
<b>GEANT4 simulation parameters</b>	
Range cut	$9 \mu m$
Weight multiplication	100
Runs	32

Table 6.5: Additional Fluka and GEANT4 simulation parameters for the LHC collimator test in SPS.

## Chapter 7

# Conclusions

At the beginning of the LHC construction, there was no mixed radiation detector available satisfying the requirements for the measurement of very high dose rates with a sufficiently accurate behavior over several orders of magnitude and a high radiation tolerance.

A radiation detector based on the secondary electron emission process was developed, characterized using Monte Carlo tools and calibrated in various radiation environments during this work. In total, 370 Secondary Emission Monitors (SEM) were produced in IHEP Protvino in Russia, tested in a fixed target experiment at CERN and installed in the LHC.

The development of the SEM was conducted according to the ultra high vacuum requirements in order to assure sufficiently low residual pressure during the foreseen 20 year lifetime of the detector to keep the ionisation signal negligible. All the steel components were fired in vacuum to further reduce the outgassing of hydrogen. Thermal and radiation induced outgassing calculations revealed a need of an active pumping element. Therefore, a sufficiently dimensioned non-evaporable getter pump St707 was included in the detector. The vacuum and baking cycle was defined and tested at CERN before the use in the series production. All electrodes were made of titanium because of its large Secondary Emission Yield (SEY) stability and favorable vacuum properties, which were confirmed by an outgassing test performed at CERN.

The first prototypes, directly derived from the ionisation chamber were showing a nonlinear behavior at high dose rates when tested in proton beams at different intensities. Additional measurements with low energy beams traced the source of the nonlinearity to the signal feedthrough, which was collecting the ionisation signal from the surrounding air. This feature was suppressed by adding a contact shielding on the signal wire.

Another effect was observed in the first prototype with the ceramic plate charging

up during irradiation, which was disturbing the internal bias field. The effect was suppressed by adding a grounded plate on the ceramics. To avoid possible vacuum and production nonconformities and to assure a low dark current by using a guard ring system, the design of the electrode holders was entirely modified.

The formula for the SEY derived by Sternglass was modified and implemented in the Monte-Carlo particle simulation code GEANT4. The resulting formula was compared to the available published data, and the systematic difference was compensated by applying a calibration factor of 0.8. The signal generation was divided into two processes, taken into account that:

- any charged particle entering or emerging from the signal electrode can initiate the emission of one electron according to the SEY parametrization.
- the total charge of particles leaving the signal electrode needs to be subtracted from the total sum of charges entering the electrode.
- the simulation result is obtained by adding the two contributions.

A weak dependence of the simulation result on the low energy electron production cutoff value was observed for low energy beams. The cutoff value was therefore chosen by reproducing a proton beam experiment and used in all other simulations.

The SEM response curves for the main particle types and the expected energy range were simulated to allow a signal current determination using the particle fluence reaching the detector.

The absolute calibration of the SEM relating the dose to the output charge was performed using the results of a dedicated high energy fixed target experiment and the corresponding simulations. The dose was obtained by measuring and simulating the energy deposition in a SEM filled by air. The output charge of the SEM under the same irradiation conditions was simulated and the two results were combined. The calibration of the SEM used by the LHC BLM system is then

$$C_{SEM} = (764 \pm 84) \text{ pC/Gray}$$

The detector was tested in the range of dose rates from 0.5 mGy/s to 400 MGy/s. The dynamic range of the SEM limited by the analog front-end used in the LHC BLM system is spanning from 13 mGy/s (equivalent to 10 pA) to 1.7 MGy/s. The LHC BLM ionisation chamber measures with the same front-end electronics in the range from 0.19  $\mu$ Gy/s to 23 Gy/s.

The detector setup from the LHC collimation areas was reproduced in the SPS accelerator, where it was used for the studies of the complete LHC BLM system. The results of these studies were used for the modifications of the LHC BLM installation. The protection resistances were added to the ionization chambers in the collimation areas and the signal and high voltage paths of the SEMs were separated from the ionization chambers. The high voltage capacitors were also removed from the chambers to avoid negative output currents.

The maximum signal expected in the SEM detectors installed around the LHC dump cores was estimated by combining the response curves with the radiation spectra simulated in Fluka. Analog signal shaping filters were chosen according to the results to allow the acquisition of fast and high intensity signals.

Row	Beam type	measurement	error	simulation	error	$\frac{meas-sim}{sim}$
1	63 MeV $p^+$ PSI	0.27	0.014	0.2665	0.0043	+1.1%
2	1.4 GeV $p^+$ PSB	0.0495	0.0006	0.0416	0.0046	+19%
3	400 GeV $p^+$ TT20	0.036	0.004	0.050	0.005	-29%
4	160 GeV muons	0.059	0.016	0.08	0.008	+26%
5	300 GeV mixed	3.43	0.75	3.95	0.19	+14
6	26 GeV mixed L	$2.74 \cdot 10^{-3}$	$0.08 \cdot 10^{-3}$	$4.58 \cdot 10^{-3}$	$0.14 \cdot 10^{-3}$	+40%
7	26 GeV mixed R	$2.04 \cdot 10^{-3}$	$0.02 \cdot 10^{-3}$	$3.56 \cdot 10^{-3}$	$0.08 \cdot 10^{-3}$	+43%
	Beam type	SEM meas.	error	IC meas.	error	$\frac{SEM-IC}{SEM}$
8	450 GeV mixed	$9.79 \cdot 10^{-4}$	$0.02 \cdot 10^{-4}$	$8.98 \cdot 10^{-4}$	$0.10 \cdot 10^{-3}$	+8.3%

Table 7.1: Summary of the obtained experimental results and the corresponding GEANT4 simulations. The units are in charges produced per primary particle hitting the chamber or a target for the mixed radiation fields. L and R stand for the left or right collimator jaw impact.

Several preproduction prototypes and series SEMs were tested in different proton and muon beams and mixed radiation fields including a high energy beam scan across the detector. The results are summarized in the Tab. 7.1 rows 1 to 4. The results showed a very high linearity and speed of the detector response. The SEM was also placed in a mixed radiation field of the SPS beam dump, where it was directly compared to the LHC BLM ionisation chamber. The signal of the ionization chamber was corrected for the space charge saturation effect (see Tab. 7.1 row 8).

The SPS collimation area installation was also used to make a full simulation of the setup and compare it with the measurements. The setup was implemented in the Fluka

code by the collimation team. The response of the detectors during a direct proton beam impact on the collimator was measured and reproduced by the Fluka simulations by calculating the energy deposition in the detector. An intermediate result of these simulations was used as an input to a GEANT4 SEM simulation (see Tab. 7.1 row 6 and 7).

In total 300 SEM detectors out of 370 produced in IHEP were tested in a high energy fixed target experiment, which was producing a mixed radiation field similar to the one expected in the LHC. The experiment served for discovering potential non-conformities from the production. It was concluded, that all the measured detectors had the inner vacuum pressure better than  $\sim 0.21$  mbar and four chambers were rejected because of too high dark current. The experiment allowed another comparison between simulation and measurement (see Tab. 7.1 row 5).

The SEM simulations agree generally very well with the corresponding measurements performed in a wide intensity, energy range and for different radiation fields. The largest disagreement between the GEANT4 simulations and the SEM measurements was -29% obtained for the challenging high energy beam scan. The Fluka simulations combined with the GEANT4 model resulted in a maximum disagreement of +43%, which complies with the required accuracy of the SEM detector of 40%. These initial systematic errors can be reduced during the comisionning of the LHC.

# Bibliography

- [1] DSU Communication Group. CERN's public website.  
<http://public.web.cern.ch/public/>
- [2] W.-M. Yao et al., J. Phys. G 33, 1 (2006) and 2007 partial update for the 2008 edition available on the PDG WWW pages (URL: <http://pdg.lbl.gov/>).
- [3] E.B. Holzer et al., Beam Loss Monitoring System for the LHC, IEEE NSS '05, Puerto Rico, CERN-AB-2006-009 BI.
- [4] D. Hasselkamp et al., Particle Induced Electron Emission II, Springer-Verlag, (1992).
- [5] D. Hasselkamp, S. Hippler and A. Scharmann, Ion-induced secondary electron spectra from clean metal surfaces, Nucl. Instrum. and Methods Phys. Res. B 18 (1987) 561.
- [6] Geant4 - A Simulation Toolkit, S. Agostinelli et al., Nuclear Instruments and Methods A 506 (2003) 250-303.
- [7] J. Allison et al., Geant4 Developments and Applications, IEEE Transactions on Nuclear Science 53 No. 1 (2006) 270-278 .
- [8] GEANT4 official web site, <http://geant4.cern.ch>
- [9] A. Fasso, A. Ferrari, J. Ranft, and P.R. Sala, FLUKA: a multi-particle transport code, CERN-2005-10 (2005), INFN/TC.05/11, SLAC-R-773.
- [10] E.J. Sternglass, Theory of Secondary Electron Emission by High-Speed Ions, Phys. Rev. 108(1957) 1.
- [11] G. Ferioli and R. Jung, Evolution of the Secondary Emission Efficiencies of various materials measured in the CERN SPS secondary beam lines, CERN-SL-97-071-BI, (1997).

- [12] C.M. Castaneda et al., Secondary electron yields from the bombardment of  $Al_2O_3$  by protons, deuterons, alpha particles and positively charged hydrogen molecules at energies in the range of 10 to 80 MeV, Nuclear Instr. and Meth. B 129(1997) 199-202.
- [13] K. Bernier et al., Calibration of secondary emission monitors of absolute proton beam intensity in the CERN SPS North Area, CERN-97-07, (1997).
- [14] B. Svensson and G. Holmén, Electron Emission from aluminum and copper under molecular-hydrogen-ion bombardment, Phys. Rev. B 25(1982) 5.
- [15] Paul Scherrer Institute, Villigen Switzerland, <http://www.psi.ch>.
- [16] C. Benvenuti and P. Chiggiato, Pumping characteristics of the St707 non-evaporable getter (Zr 70-V 24.6-Fe 5.4 wt%), J. Vac. Sci. Technol. A 14 (1996) 3278-3282.
- [17] C. Zamantzas et al., The LHC Beam Loss Monitoring System's Data Contribution to other Systems, IEEE NSS '07, Honolulu Hawaii, conference proceedings.
- [18] V.M. Grichine et al., An implementation of ionisation energy loss in very thin absorbers for the GEANT4 simulation package, Nucl. Instrum. Methods Phys. Res., A 453 (2000) 597-605.
- [19] J. Vollaire, D. Forkel-Wirth, S. Roesler, CERN-SC-2007-074-RP-TN.
- [20] R. Schmidt et al., Protection of the CERN Large Hadron Collider, 2006 New J. Phys. 8 290
- [21] E. Gschwendtner, B. Dehning, G. Ferioli, W. Friesenbichler, V. Kain, The Beam Loss Detection System of the LHC Ring, CERN-SL-2002-021-BI .
- [22] O. Bruning and P. Collier, Building a behemoth, Nature 448 (2007) 285-289.
- [23] M. Benedikt, P. Collier, V. Mertens, J. Poole, K. Schindl, LHC Design Report Volume v.3 : the LHC Injector Chain, CERN-2004-003-V-3.
- [24] J.M. Jimenez et. al, LHC and SPS Electron Cloud Studies, AIP Conf. Proc. June 8, 2005, Vol. 773, pp. 211-215.
- [25] J. Bosser, G. Ferioli, Comparative test results of various beam loss monitors in preparation for LHC, CERN-SL-99-042-BI.
- [26] M. Stockner, Beam Loss Calibration Studies for High Energy Proton Accelerators, Thesis at Vienna University of Technology, 2007.

- [27] G. Ferioli, Private communications.
- [28] J. Camas, G. Ferioli, J.J. Gras, R. Jung, Screens versus SEM Grids for single pass measurements in SPS, LEP and LHC, CERN-SL-95-62 BI 1995.
- [29] G. Ferioli and R. Jung, Evolution of the Secondary Emission Efficiencies of various materials measured in the CERN SPS secondary beam lines, CERN-SL-97-071-BI, 1997.
- [30] K. Bernier et al., Calibration of secondary emission monitors of absolute proton beam intensity in the CERN SPS North Area, CERN Yellow Report, CERN-97-07, 1997.
- [31] K.A. Brown, I.H. Chiang, A. Pendzik, T. Tallerico, Observations of secondary emission chamber degradation from very high intensity proton beams at the AGS, Particle Accelerator Conference proceedings, Vancouver, 1998.
- [32] <http://www.thermo.com/cidtec>.
- [33] [http://en.wikipedia.org/wiki/Weighted\\_mean](http://en.wikipedia.org/wiki/Weighted_mean), viewed on June 2008.
- [34] [http://en.wikipedia.org/wiki/Scanning\\_electron\\_microscope](http://en.wikipedia.org/wiki/Scanning_electron_microscope), viewed on June 2008.
- [35] H. Bichsel, A method to improve tracking and particle identification in TPCs and silicon detectors, Nucl. Inst. & Meth. A (in press, 2006).
- [36] Glenn F. Knoll, Radiation Detection and Measurement, Wiley 1999, 3rd Edition, ISBN 0-471-07338-5.
- [37] L. Austin and H. Starke, Ann. Phys. (Leipzig), vol. 9, 1902.
- [38] P. Koschar et al., Secondary-electron yield as a probe of preequilibrium stopping power of heavy ions colliding with solids, Phys. Rev. A 40, 3632 - 3636, 1989.
- [39] E.F.DA Silveira and J.M.F. Jeronymo, Secondary electron emission from the entrance and exit surfaces of thin aluminium foils under fast light ion bombardment, Nucl. Instr. and Meth. B24/25, 1987.
- [40] J.C. Ashley, C.J. Tung and R.H. Ritchie, Electron Inelastic Mean Free Paths and Energy Losses in Solids, Surface Science 81 (1979) 409-426.
- [41] CERN EU High Energy Reference Field, <http://cern.ch/cerf>.
- [42] Rudolf K. Bock and A. Vasilescu, The Particle Detector BriefBook, Berlin, Springer, 1998.

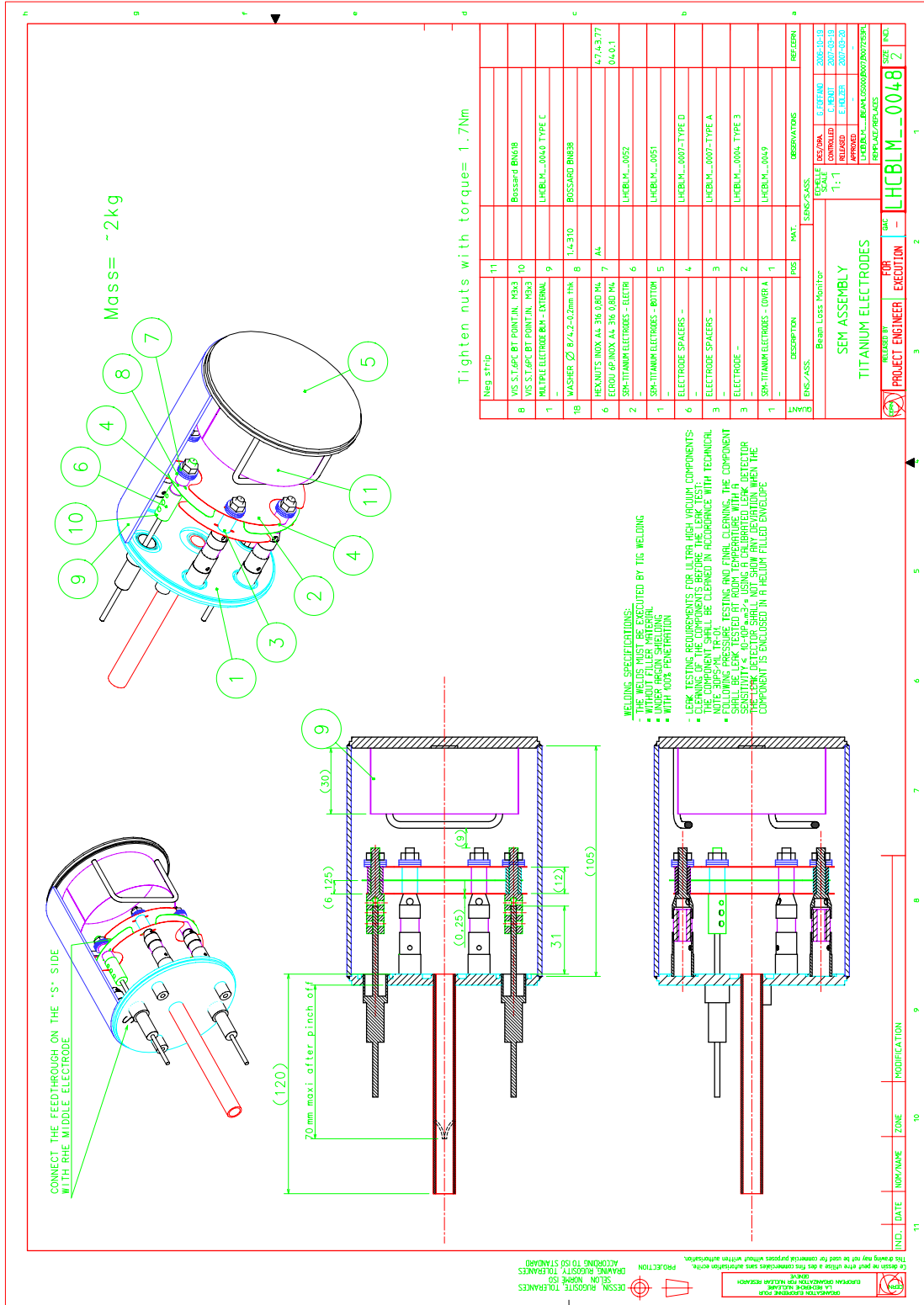
- [43] Laurette Ponce, private communications.
- [44] Institute of High Energy Physics, Protvino, Russia.
- [45] L. Bottura, M. Calvi, A. Siemko, Stability analysis of the LHC cables, Cryogenics Volume 46, Issues 7-8, 2005.
- [46] V.Baglin, G.Vorlaufer, I.Collins, B.Henrist, N.Hilleret, A Summary of Main Experimental Results Concerning the Secondary Electron Emission of Copper, CERN-LHC-Project-Report-472, 2001.
- [47] J.R.J. Bennett, S. huges, R.J. Elsey, T.P. Parry, Outgassing from stainless steel and the effects of the gauges, Vacuum 73, 2004, 149-153 .
- [48] A. A. Lisachenko and R. V. Mikhailov, Point defects as the centers of titanium dioxide sensitization in the visible spectral range, Technical Physics Letters, Vol. 31, Num. 1, 2005.
- [49] <http://www.sct-ceramics.com>
- [50] C. Zamantzas, The Real-Time Data Analysis and Decision System for Particle Flux Detection in the LHC Accelerator at CERN, CERN-thesis-2006-037, Brunel University 2006.
- [51] H. Bruining, Physics and applications of secondary electron emission, Pergamon Press, London, 1954, p.132.
- [52] J.-P. Bacher, C. Benvenuti, P. Chiggiato, M.-P. Reinert, and S. Sgobba, Thermal desorption study of selected austenitic stainless steels, J. Vac. Sci. Technol. A, Vol. 21, No. 1, 2003.
- [53] Boude C. Moore, Thin-walled vacuum chambers of austenitic stainless steel, J. Vac. Sci. Technol. A, Vol. 19, No. 1, 2001.
- [54] A. Sieverts, Z Chemie 88, 451, 1914 .
- [55] P. Chiggiato, Thermal outgassing of hydrogen: models and methods for reduction, CERN Accelerator School, Spain 2006, proceedings to be published.
- [56] SAES Getters S.p.A., <http://www.saesgetters.com>
- [57] C. Benvenuti, CAS - CERN Accelerator School and ALBA Synchrotron Light Facility : Course on Vacuum in Accelerators, CERN-2007-003.

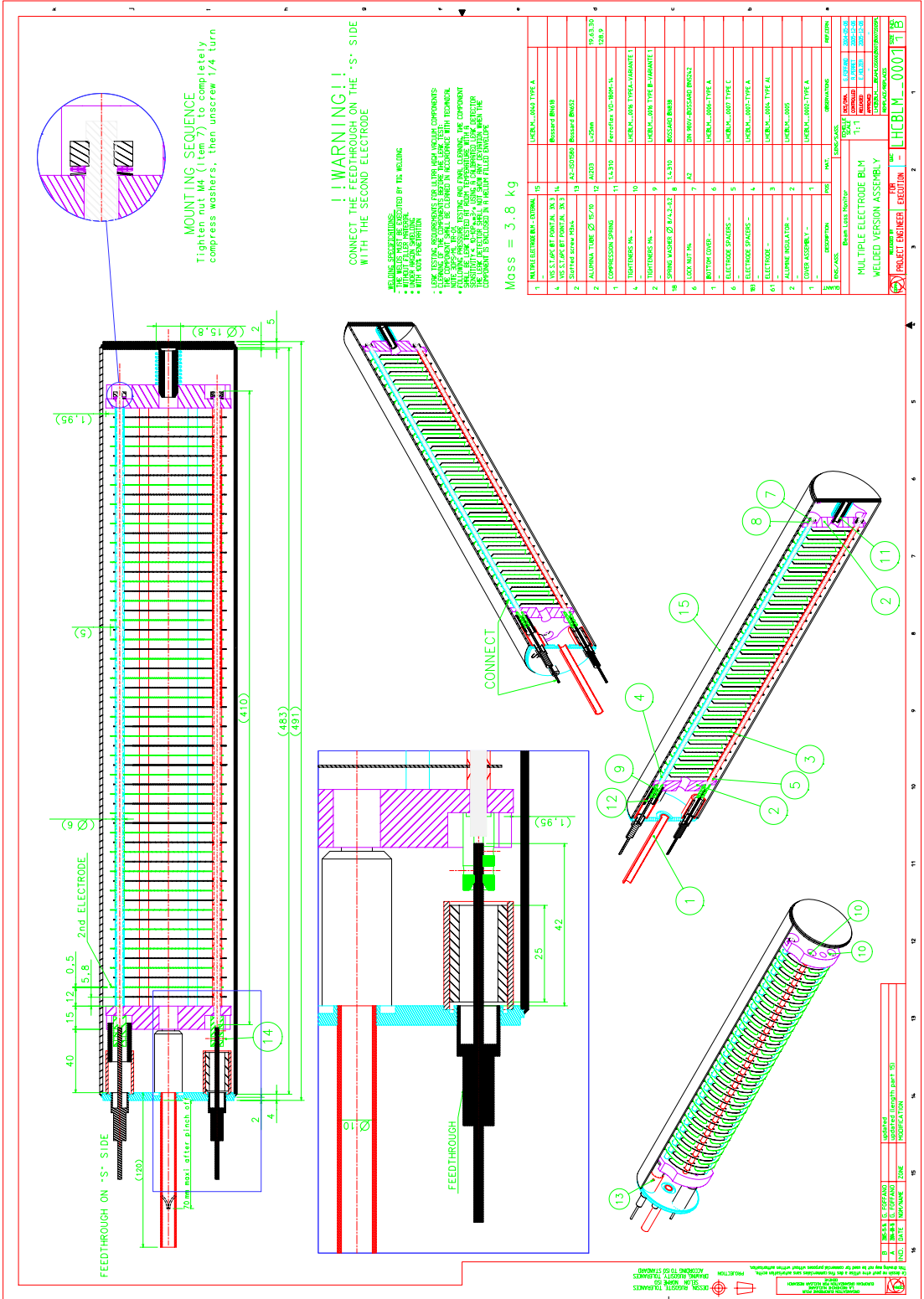
- [58] Outgassing in thin wall stainless steel cells, *J. Vac. Sci. Technol. A*, Volume 17, Issue 3, pp. 1040-1046, 1999.
- [59] K. Jousten, CAS - CERN Accelerator School : Vacuum Technology, OPEN-2000-274, CERN 1999.
- [60] M. Taborelli, private communications.
- [61] I. Wevers, private communications, unpublished results.
- [62] P. Chiggiato et al., Surface cleaning efficiency measurements for UHV applications, *Vacuum*, Volume 53, Issues 1-2, 1999.
- [63] P. Chiggiato, Vacuum Calculation of the TBID (Target Beam Instrumentation Downstream) for CNGS, CERN-TS-Note-2006-002.
- [64] J. Gómez-Goñi and A. G. Mathewson, Temperature dependence of the electron induced gas desorption yields on stainless steel, copper, and aluminum, *J. Vac. Sci. Technol. A* 15.6., 1997.
- [65] N. Yoshimura, A differential pressure-rise method for measuring the net outgassing rates of a solid material and for estimating its characteristic values as a gas source, *J. Vac. Sci. Technol. A*, Volume 3, Issue 6, pp. 2177-2183, 1985.
- [66] J. Apostolakis, G. Folger, V. Grichine, A. Howard, V. Ivanchenko, M. Kossov, and A. Ribon, Hadronic shower shape studies in Geant4, Technical Report CERN-LCGAPP-2007-02, CERN, March 2007. version 1.1.
- [67] D.H. Wright et al., Recent Developments And Validations in Geant4 Hadronic Physics, SLAC-PUB-12348, 2007.
- [68] H.W. Bertini and P. Guthrie, *Nucl. Phys.* A169 (1971).
- [69] GEANT4 lectures, [http://www.ge.infn.it/geant4/training/siena\\_oct2006/geant4lectures.html](http://www.ge.infn.it/geant4/training/siena_oct2006/geant4lectures.html)
- [70] H. Burhardt, V. M. Grichine, and V. N. Ivanchenko et al., Geant4 Standard Electromagnetic Package for HEP applications, Nuclear Science Symposium Conference Record, pp.1907-10, 2004 IEEE.
- [71] J.E. Borovsky, D.J. McComas and B.L. Barraclough, *Nucl. Instr. and Meth.* B30, 191-195, 1988.
- [72] D.M. Suszcynsky and J.E. Borovsky, Modified Sternglass theory for the emission of secondary electrons by fast-electron impact, *Physical Review A*, Vol. 45, Num. 9, 1992.

- [73] W.R. Leo. *Techniques for Nuclear and Particle Physics Experiments: A how to approach*, Springer Berlin, 1987.
- [74] H. Kagan, S. Roe, P. Weilhammer et al., *RD42 Status Report: Development of Diamond Tracking Detectors for High Luminosity Experiments at the LHC*, CERN Report CERN-LHCC-2008-005, 2008.
- [75] R.E. Kirby and F.K. King, *Secondary Electron Emission Yields From PEP-II Accelerator Materials*, SLAC-PUB-8212, 2000.
- [76] H. Rothard, *Secondary-electron yields from thin foils: A possible probe for the electronic stopping power of heavy ions*, *Phys. Rev. A* 41, 2521 - 2535 (1990).
- [77] N. Hilleret et al., *Secondary electron emission data for the simulation of electron cloud*, Workshop proceedings, CERN, 15 - 18 Apr 2002, pp.75-78
- [78] International Commission on Radiation Units and Measurements. *Average energy required to produce an ion pair*. Technical report, ICRU Report 31, Washington D.C., 1979.
- [79] National Institute of Standards and Technology, <http://www.nist.gov>
- [80] T. Böhlen, *Beam Loss Patterns at the LHC Collimators Measurements & Simulations*, CERN Master Thesis, submitted in September 2008.
- [81] R.M. Zwaska, *Accelerator Systems and Instrumentation for the NuMI Neutrino Beam*, PhD thesis, University of Texas at Austin, December 2005.
- [82] L.A. Viehland and E.A. Mason, *Transport properties of gaseous ions over a wide energy range*, IV, *Atomic data and nuclear tables* 60, 37-95 , 1995.

Appendix A

Drawings







## Appendix B

# Signal paths for the LHC BLM detectors

The analogue part of the LHC BLM system's measurement chain is presented on the Fig. B.1 and B.2. The HV capacitor was removed from the electronic boxes of the detectors in the high radiation areas in order to avoid negative output currents during large dose rate periods.

The current to frequency converter (CFC) front end electronics card

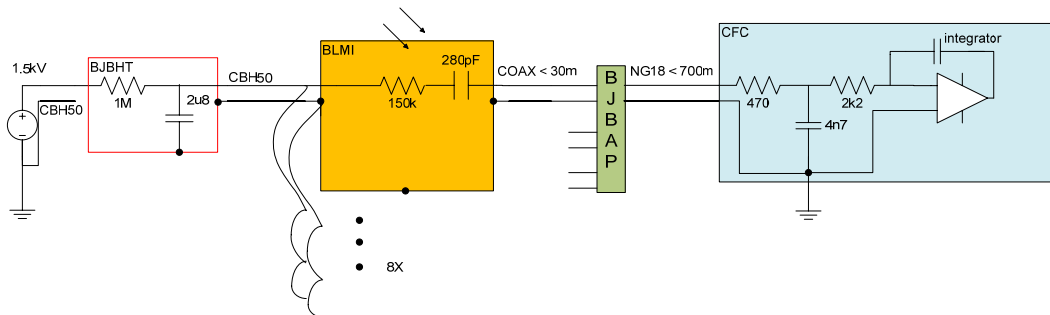


Figure B.1: Schematic of the signal paths for the BLM system's ionisation chambers in the areas, where large annual dose levels are expected.

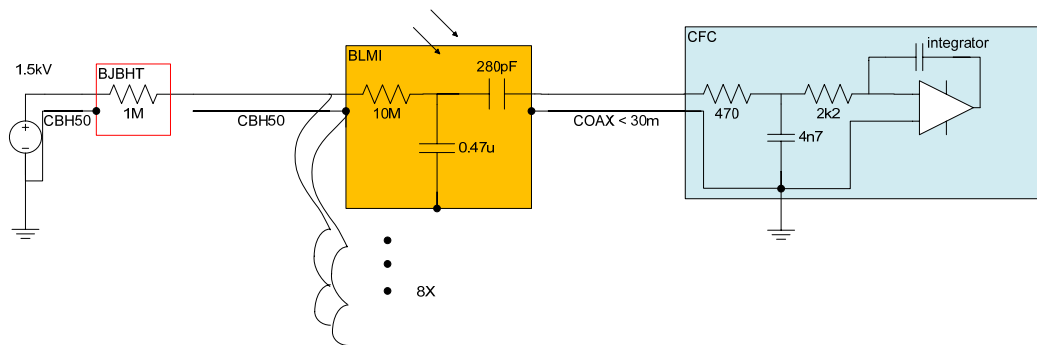


Figure B.2: Schematic of the signal paths for the BLM system's ionisation chambers in the LHC ARCs.

## Appendix C

# Space Charge Effect Correction

The maximum charge integrated from the current of the ionisation chamber (IC) under the SPS TIDV beam dump during a beam abort is about  $45 \mu\text{C}$ . This correspond to a dose of about 0.8 Gy, but the SEM, which does not suffer from any saturation effects measures at the same location up to 6 Gy. The IC should therefore produce about seven times more signal if it was working in a linear way.

In a sensitive detector volume of  $1500 \text{ cm}^3$  and with an irradiation time of  $t_c = 7.8 \mu\text{s}$  this corresponds to an ionisation rate of  $1.7 \cdot 10^{11} \text{ ions}/(\text{cm}^3 \mu\text{s})$ . The space charge saturation effects start to be important for the utilized LHC BLM ionisation chamber configuration at an ionisation rate of about [26]

$$\phi_{crit} = \mu \frac{\epsilon_0}{q} \cdot \frac{4U^2}{d^4} = 1.1 \cdot 10^8 \left[ \frac{\text{ions}}{\text{cm}^3 \mu\text{s}} \right] \quad (\text{C.1})$$

which corresponds to a charge of  $0.21 \mu\text{C}$  deposited in  $7.8 \mu\text{s}$  inside the detector and is about 1500 times lower compared to the maximum measured ionisation rate. The nitrogen ion mobility of  $\mu = 2.43 \cdot 10^{-6} \text{ cm}^2/\text{V} \mu\text{s}$  was taken from [82].

In [81] and [26], the space charge calculations are treated as follows.

Space charge refers to slow moving ions that deform the applied electric field. At the critical ionisation rate, a dead zone starts to form. The electric field is completely shielded by the ions (nearly field free zone). As long as the irradiation continues the charge density in the dead zone increases approximately linear in time. If the ionisation rate is higher than the critical one, the dead zone expands. If one assumes all charges generated in the dead zone to be lost due to recombination, the effective length of the ionisation chamber is reduced by the width of the dead zone. A formula to calculate the effective length  $x_0$  of the ionisation chamber is derived in [81]

$$x_0 = \left[ \frac{\epsilon_0}{q} \frac{4\mu U^2}{\phi} \right]^{1/4} \quad (\text{C.2})$$

where  $\phi$  is the ionisation rate. The space charge collection efficiency coefficient  $\varepsilon_{sc}$  can be expressed as

$$\varepsilon_{sc} = x_0/d \qquad Q_m = \varepsilon_{sc} \cdot Q \qquad (C.3)$$

One can derive from the equation above the analytical correlation between measured and deposited charge

$$Q = \left( \frac{Q_m}{K_2} \right)^{\frac{4}{3}} \qquad K_2 = \frac{1}{d} [4 \cdot \epsilon_0 \cdot V_{IC} \cdot t_c \cdot \mu \cdot U^2]^{\frac{1}{4}} \qquad (C.4)$$

The correction to the measured charge was applied for the data presented on the Fig. 6.23 and converted to the deposited dose. It should be noted that the ionisation chambers in the LHC BLM system will not have signal filters, so the input of the electronics will be saturated before the space charge effects could occur.

## Appendix D

### List of publications

- Simulations and Measurements of Secondary Electron Emission Beam Loss Monitor for LHC/ Kramer, Daniel et al., Nucl. Phys. B, Proc. Suppl. 172 (2007) 246-249
- Very High Radiation Detector for the LHC BLM System Based on Secondary Electron Emission / Kramer, Daniel et al., 2007 IEEE Nuclear Science Symposium Conference Record
- Secondary Electron Emission Beam Loss Monitor for LHC / Kramer, Daniel et al., CERN-AB-2007-027
- Beam Loss Monitoring System for the LHC / Holzer, E B et al., CERN-AB-2006-009
- LHC Beam Loss Detector Design: Simulation and Measurements / Kramer, Daniel, Stockner, M et al., CERN-LHC-PROJECT-Report-1026
- The LHC Beam Loss Measurement System / Kramer, Daniel, Dehning, B et al., CERN-LHC-PROJECT-Report-1025
- Generation of 1.5 Million Beam Loss Threshold Values / Holzer E B et al., CERN-LHC-PROJECT-Report-1158
- Development, Production and Testing of 4500 Beam Loss Monitors / Holzer E B et al., CERN-AB-2008-054
- FLUKA Monte Carlo simulations and benchmark measurements for the LHC beam loss monitors / Sarchiapone, L et al., Nucl. Instrum. Methods Phys. Res., A 581 (2007) 511-516
- Beam Scraping to detect and remove Halo in LHC Injection / Letnes, P A et al., CERN-LHC-PROJECT-Report-1096

- Abort Gap Cleaning Using the Transverse Feedback System: Simulation and Measurements in the SPS for the LHC Beam Dump System / Koschik, A et al., LHC-PROJECT-Report-1160
- Classification of the LHC BLM Ionization Chamber / Stockner, M et al., CERN-AB-2007-029
- Optical telescopes for COMPASS RICH-1 up-grade / P. Abbon et al., Czech.J.Phys.56, F315-F322 (2006)
- Optical design for BIPM imaging system / Kramer, Daniel et al., CERN-AB-2005-072
- Fast photon detection for COMPASS RICH-1 / Abbon, P et al., Nucl. Instrum. Methods Phys. Res., A 572 (2007) 419-421
- Design and status of COMPASS FAST-RICH / Abbon, P et al., Nucl. Instrum. Methods Phys. Res., A 567 (2006) 114-117
- Fast photon detection for the COMPASS RICH detector / Schill, C et al., Nucl. Phys. B, Proc. Suppl. 172 (2007) 75-78
- Fast Photon Detection for Particle Identification with COMPASS RICH-1 / Abbon, P et al., Nucl. Instrum. Methods Phys. Res., A 580 (2007) 906-909
- A new measurement of the Collins and Sivers asymmetries on a transversely polarised deuteron target / Ageev, E S et al., Nucl. Phys. B 765 (2007) 31-70
- Accuracy of Profile Monitors and LHC Emittance Measurements / Arduini, Gianluigi et al., LHC-Project-Report-782
- Design and Tests of a New Rest Gas Ionisation Profile Monitor Installed in the SPS as a Prototype for the LHC / Fischer, C et al., CERN-AB-2004-031-BDI
- Comparative Transverse Distribution Measurements between the New SPS Rest Gas Ionisation Monitor and the Wire Scanner Monitors / Roncarolo, F et al., CERN-AB-2004-088